Versatile Association Behavior in Mixtures of Oppositely Charged Amphiphiles

From DNA-Like Assembly of Supramolecular Helices to Coacervation in Chiral Surfactant Systems

Du, Guanqun

2022

Document Version:
Publisher's PDF, also known as Version of record

Versatile Association Behavior in Mixtures of Oppositely Charged Amphiphiles:

From DNA-Like Assembly of Supramolecular Helices to Coacervation in Chiral Surfactant Systems

GUANQUN DU
PHYSICAL CHEMISTRY | DEPARTMENT OF CHEMISTRY | LUND UNIVERSITY

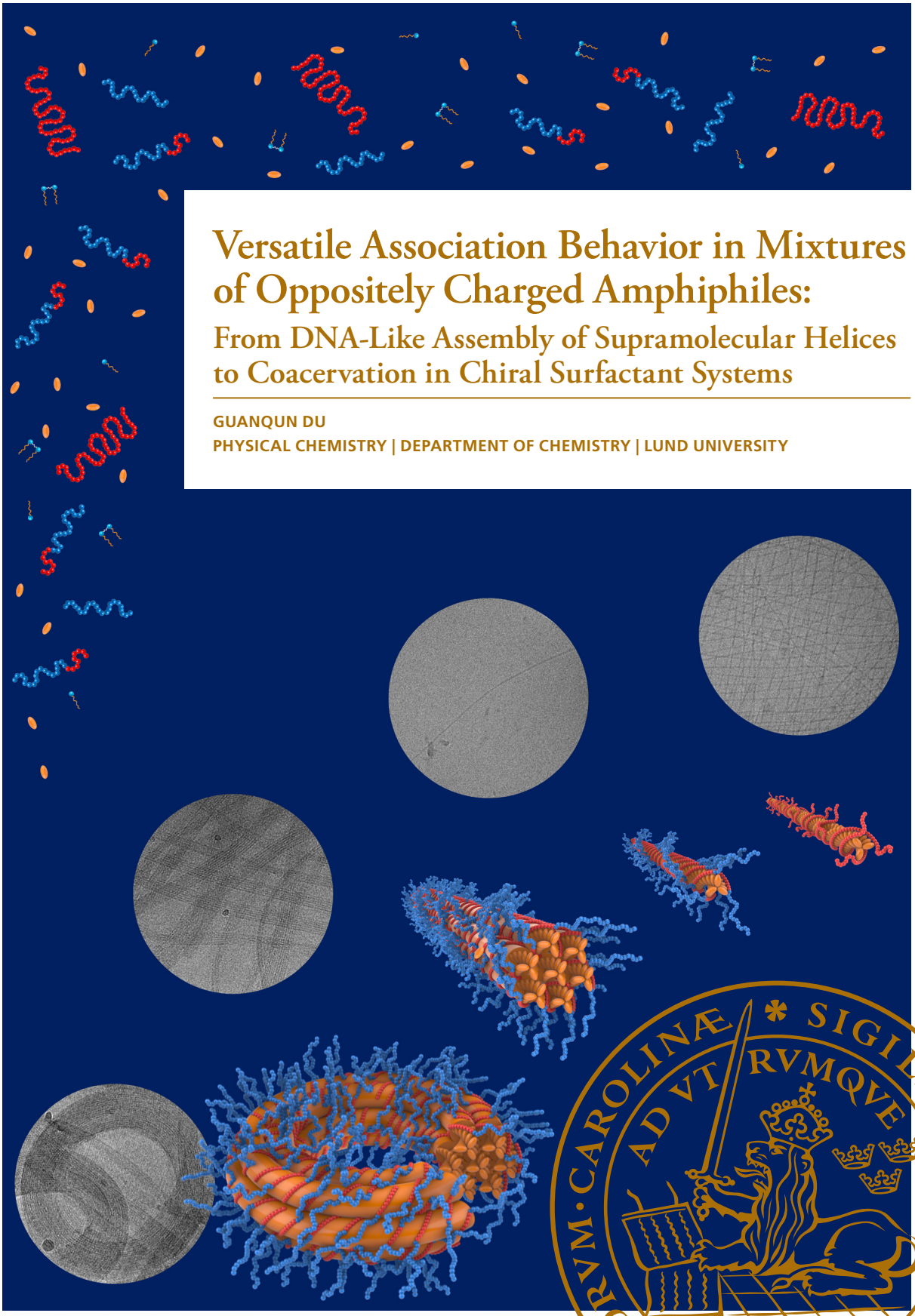

Printed by Media-Tryck, Lund 2022 NORDIC SWAN ECOLABEL 3041 0903

LUND UNIVERSITY

ISBN: 978-91-7422-852-6

Physical Chemistry
Faculty of Science
Lund University

9 789174 228526

Versatile Association Behavior in Mixtures of Oppositely Charged Amphiphiles:

From DNA-Like Assembly of Supramolecular Helices to Coacervation in Chiral Surfactant Systems

Versatile Association Behavior in Mixtures of Oppositely Charged Amphiphiles:

From DNA-Like Assembly of Supramolecular Helices to Coacervation in Chiral Surfactant Systems

by Guanqun Du

LUND
UNIVERSITY

DOCTORAL DISSERTATION

by due permission of the Faculty of Science, Lund University, Sweden.
To be defended on January 14, 2022 at 09.15 AM in Lecture hall A at the Department of Chemistry, Lund University.

Faculty opponent
Prof. Dr. Michael Gradzielski, Institut für Chemie,
Technische Universität Berlin, Berlin, Germany

Organization
LUND UNIVERSITY
Department of Chemistry
Box 124
SE-221 00 LUND
Sweden

Document name
DOCTORAL DISSERTATION

Date of issue
2022-01-14

Author(s)
Guanqun Du

Sponsoring organization
China Scholarship Council (CSC scholarship, No. 201706870015)

Title and subtitle

Versatile Association Behavior in Mixtures of Oppositely Charged Amphiphiles: From DNA-Like Assembly of Supramolecular Helices to Coacervation in Chiral Surfactant Systems

Abstract

As biological surfactants, bile salts (BSs), play important roles in biological processes, i.e., food digestion, but also in BS-related diseases, as well as in applications. In this thesis, the main focus was to gain a fundamental understanding of the intermolecular interactions between BSs and cationic block copolymers with the purpose of developing new BS sequestrants that are used in the treatment of BS-related diseases. In addition, the studies also aimed to explore the unique co-assembled structures formed in mixtures of BS and either block copolymers or chiral gemini surfactants of opposite charge, which can be used for biomedical applications. The versatile association behavior, thermodynamic interactions, different morphologies and supramolecular structures of the complexes formed in these oppositely charged amphiphile systems were investigated by dynamic and static light scattering, isothermal titration calorimetry, high-sensitive differential scanning calorimetry, small angle X-ray scattering, cryogenic (cryo-) transmission electron microscopy and cryo-electron tomography, turbidimetric titration, and electrophoretic mobility measurements. Based on these studies, this thesis is divided into three parts.

The studies on the oppositely charged block copolymer-BS systems are summarized first. Two cationic diblock copolymers with the same charged block of poly((3-acrylamidopropyl)trimethylammonium chloride) (PAMPTMA(+)) but with different nonionic blocks, either the thermoresponsive poly(*N*-isopropylacrylamide) (PNIPAM) or methoxy poly(ethylene glycol) (MPEG), and two homopolymers (PAMPTMA(+)$_{130}$ and PNIPAM$_m$) were explored in terms of their interactions with the bile salt sodium deoxycholate (NaDC) in water at 25 °C. The experimental studies showed that single supramolecular helices were formed in the PAMPTMA(+)$_{130}$-NaDC system, while they condensed into different hierarchical arrangements, i.e., orderly parallel structures and DNA-like hexagonally packed bundles or toroids when using the diblock copolymers. The chirality of BS molecules and the supramolecular chirality of the helices obtained in different polymer-NaDC systems enabled the mixed co-assemblies the ability to load drugs, highlighting their potential use in drug encapsulation and delivery. Moreover, the observed heat-induced phase transition in the PNIPAM$_{120}$-*b*-PAMPTMA(+)$_{30}$-NaDC system demonstrated the formation of composition-controlled thermoresponsive mixed aggregates, which are appealing in stimulating responsive-related applications.

The co-assembly in PNIPAM$_{65}$-*b*-PAMPTMA(+)$_{20}$ block copolymer-sodium dodecyl sulfate (SDS) system was studied in the second part of the thesis. It was found that SDS interacts with both blocks of the copolymer and associates in a step-wise process involving both electrostatic and hydrophobic interactions, which stands in contrast to the copolymer-NaDC system where the NaDC preferentially interacts with PAMPTMA(+) blocks. This is reflected in both a different mixed complex structure and a divergent thermoresponsive behavior compared to the PNIPAM$_{120}$-*b*-PAMPTMA(+)$_{30}$-NaDC system.

Lastly, the study on the mixtures of NaDC and three gemini surfactants 1,4-bis(dodecyl-*N*,*N*-dimethylammonium bromide)-2,3-butanediol (12-4(OH)$_2$-12), including two chiral ones ((2*S*,3*S*)-12-4(OH)$_2$-12 and (2*R*,3*R*)-12-4(OH)$_2$-12) and the racemate ((±)-12-4(OH)$_2$-12), revealed different aqueous phase behaviors including coacervation. It was found that the BS can recognize the gemini surfactants by showing either an enhanced, switched, or induced chirality in (2*S*,3*S*)-12-4(OH)$_2$-12-NaDC, (2*R*,3*R*)-12-4(OH)$_2$-12-NaDC, and (±)-12-4(OH)$_2$-12-NaDC mixtures, respectively.

Key words

Bile salts, Block copolymers, Oppositely charged polymer-surfactant systems, Co-assembly, BS sequestrants, Gemini surfactants, Supramolecular helices, Hexagonal packing, Chirality, Thermoresponsive behavior, Scattering, Tomography, Calorimetry

Classification system and/or index terms (if any)

Supplementary bibliographical information

Language
English

ISSN and key title

ISBN
978-91-7422-852-6 (print)
978-91-7422-853-3 (pdf)

Recipient's notes

Number of pages
266

Price

Security classification

Signature Guanqun Du 杜冠群 Date 2021-12-03

Versatile Association Behavior in Mixtures of Oppositely Charged Amphiphiles:

From DNA-Like Assembly of Supramolecular Helices to Coacervation in Chiral Surfactant Systems

by Guanqun Du

LUND
UNIVERSITY

This doctoral thesis is constructed as a summary of research papers and consists of two parts. An introductory text puts the research work into context and summarizes the main conclusions of the papers. Then, the research publications themselves are reproduced. The research papers may either be previously published or manuscripts at various stages.

Cover Front: by Guanqun Du. Illustration of bile salts, head-tail surfactants, gemini surfactants, polymers, supramolecular helices, bundle and toroid of the helices. Cryo-TEM images of the supramolecular helices, bundles and toroids of the helices.

Cover Back: by Guanqun Du. Cryo-TEM image showing unexpected ice contamination (no sample was found ☹). However, the beauty of the large ice crystal made the experiments not so upsetting. ☺

Division of Physical Chemistry
Department of Chemistry
Faculty of Science
Lund University

ISBN 978-91-7422-852-6 (print)
ISBN 978-91-7422-853-3 (pdf)

Printed in Sweden by Media-Tryck, Lund University, Lund 2022

To my family

Contents

Acknowledgments

Time is flying. It is unbelievable that I have spent four years in Lund, Sweden, for one of my life projects, getting a PhD. It is still like an unimaginable dream for someone who comes from a little village, who never thought they would have a chance to study abroad, but in the end has experienced a beautiful and colorful PhD journey here. This time has been full of fun, happiness, courage, challenges, and also (painful and happy) tears. But the most important component is the lovely people who I have been lucky enough to meet and who have helped me make this dissertation possible. At this moment, I would like to take this great opportunity to give my sincere gratitude to all of you.

First and foremost, I would like to give my sincerest thanks to my dear "supermother" (supervisor mother), **Karin Schillén**, I believe it is fate that guided me to come to Lund to do my PhD with you; the night we met in Lund's city center is still as fresh as if it were yesterday. It turns out that doing my PhD under your supervision at Lund University is one of the most wonderful and unique experiences in my life. Thank you, **Karin**, for taking such good care of me, both with regard to my scientific work and in my daily life these past years: you are always so patient and have kindly helped me with numerous questions and problems. You always support my various ideas both within and without the scientific scope, and I am grateful for your endless encouragement for anything I want to do. We have had countless fun and moving moments when spending time together and I have enjoyed all these moments so much! It is such a great pleasure to have been accompanied by you all these years. Thank you also for offering great opportunities for me to visit many other places outside Lund, which has largely enriched my PhD life. **Karin**, your positive attitude, patience, kindness and young-heart attitude have inspired me a lot. In my heart, you are not only my scientific supervisor but also my close friend, English tutor, mentor and so much more. Words are powerless to express my gratitude to you, everything you have contributed to during this journey is deeply rooted in my heart and I will cherish it for the rest of my life.

Viveka Alfredsson, my co-supervisor, I am grateful for your help and support when I needed it, and I immensely enjoyed our fruitful discussions and collaborations.

Luciano Galantini, my dear "superfather", who in my heart is also my supervisor and friend, and not only a collaborator. Thank you for all your help, support and encouragement during my PhD studies. Without you and your humor, the tough parts of my PhD project would not be easily overcome–you always have such inspired ideas and thoughts to improve the projects. Thank you very much for taking good care of me when I was in Rome; it was such a pleasant time with all the ice cream, pizza, pasta, and of course, the fruitful scientific works.

Yilin Wang, **Yaxun Fan**, thank you for taking good care of me and for good collaborations in Beijing. **Yilin**, thank you for offering me the great opportunity to work in your group for two months. Thank you two for all the nice discussions, meals and group activities. It was a really nice and unique experience for someone who studies abroad and still has the chance to experience part of the PhD life in her mother country: this made my PhD journey even more colorful and cherished. **Yuchun Han**, thank you also for taking care of me when I was in Beijing the second time.

Bo Nyström, thank you for hosting me in Olso. I am so grateful for all the nice discussions and your contributions to my PhD studies.

Björn Lindman, it is actually you who gave me such a life-changing opportunity permitting me to experience this incredible and unforgettable journey in Lund. I would not be a lucky member of the big Physical Chemistry family if you hadn't opened a stranger's email from another part of the planet and recommended me to Karin. I am extremely grateful for your recommendation, help and encouragement.

Alessandra Del Giudice, my great collaborator, you have contributed a lot to my studies, and I feel so lucky to have a collaborator like you with enormous knowledge in the scattering field. I could not have finished my PhD studies without your invaluable help and contributions–thank you for your support. **Suelen Gauna Trindade**, my scientific sister, I must say we have overcome many challenges together during 2020. It was so joyful to do experiments, chat, laugh, and share funny things with you when you were in Lund, and the experience became even more cherished during this tough period. Thank you for all your help, company and collaboration.

Domagoj Belić, **Anna M. Carnerup**, **Crispin Hetherington**, you are my indispensable cryo-TEM supporters. **Dom**, I am very impressed by your microscopy expertise and I enjoyed all the discussions, thank you for all your help and contribution to my PhD project. **Anna**, I really appreciate that you were willing to teach me how to prepare and measure my challenging samples; it was such a pleasant time working with you. **Crispin**, I really appreciate your effort in getting good images of my samples during the tough Covid-19 period.

I would like also to thank my other collaborators who have contributed to this project in different aspects. **Watson Loh**, **Nicolae V. Pavel**, **Giancarlo Masci**, **Kaizheng Zhu**, **Lili Zhou**, **Martin Malmsten**, **Elisa Maria Parra Ortiz**, **Lennart Piculell**, **Tommy Nylander**, and **Reidar Lund**, thank you all for your contributions and nice discussions during this project.

Johan Larsson, **Karolina Mothander**, my officemates, thank you for your company these years. **Mohammad Arif Kamal**, **Antara Pal**, thank you two for always being available to talk about plants and flowers; it was so joyful to discuss how to make our plants survive and be happy. **Simon Fridolf**, I was lucky to start my PhD project together with you when you were doing your project work: thanks for your work and your help with the NMR measurements. **Ben Humphreys**, thank you for the AFM measurements. **Jennifer Gilbert**, thank you for squeezing my sample in your MAX IV beam time. **Marco Fornasier**, thank you for the nice Italian pasta and all the good times.

Maria Lövgren, **Maria Södergren**, **Helena Persson**, **Christopher Ward**, and **Peter Holmqvist**, thank you all for your help, support and patience when addressing my various practical and technical problems.

Thanks to all the previous and current colleagues at **Physical Chemistry** for making such an incredible international working environment. I really enjoyed working in such a big family. I will miss the "Fika", fruits, Friday cakes, and all the nice times in the division very much.

I also have many Chinese friends who made me feel at home in Lund and that I would like to thank. **Meiting Wang**, my dear Ting, I really miss all the good times we spent together here: thank you for always taking good care of me. **Xiaoyan Liu**, a great sister in many aspects, you always have such inspired thoughts and positive attitudes. It was always so joyful to chat, hang out and hike with you. **Hong Jiang**, we always cheered each other up when we met difficulties during our PhD studies; thank you for being so supportive. Many thanks to **Na Hu**, **Weijing Qi**, **Xugang Dang**, **Qian Wang**, **Suxun Pan**, **Junhao Dong**, **Kena Li**, **Yutang Li**, **Hongduo Lu**, **Feifei Peng**, **Qi Shi**, and **Haiyue Gong**, for all the good times in Lund.

Fengdan Song, my dear close friend, you deserve several lines although you did not directly accompany me on this journey. I would like to thank you for all the weekly chats by video and the cherished time we spent together in Beijing. You are such a dear friend with whom I have freely shared anything from laughs to tears during this almost decade-long friendship. **Jieli Lyu**, **Jiayun Fan**, my scientific sisters and friends, thank you for your encouragement and for always being available to share the highs and the lows of our PhD studies.

I would like also to acknowledge the financial support from **China Scholarship Council** (**CSC**) for supporting me to do my PhD at Lund University. Many thanks to my Master thesis supervisor **Junxia Peng** at Shaanxi Normal University for providing the high-level scientific platform, for your help during my CSC scholarship application, and for your encouragement that pushed me forward on this scientific journey. I would also like to thank my Bachelor thesis supervisor **Rong Yang** at Xi'an University of Technology for taking me into the world of research.

Last but not least, I would like to give my tremendous and loving gratitude to my **parents** and **brother** for their unconditional love and endless care. Thank you for always believing in me, supporting any choice and decision I have made, and encouraging me to keep working on what I want to do and who I want to be. I love you forever! ☺

最后也是最重要的，感谢我的父母和弟弟给予我无条件的爱和无尽的关心。感谢你们一直相信我，支持我的任何选择和决定，并一直鼓励我做我想做的事和成为我想成为的人。永远爱你们！☺

Guanqun Du

November 2021 in Lund, Sweden

杜冠群

2021 年 11 月于瑞典隆德

Popular science summary

Surfactants, named from surface active agents, are amphiphilic molecules, which generally contain a hydrophilic head (that likes water) and a hydrophobic tail (that dislikes water but likes oil) (Figure 1a). This means surfactants like both water and oil, and such a unique property enables them to be extensively used in household detergents and cosmetics. In these applications, surfactants work as bridges catching both water-soluble and water-insoluble (oily) substances, and thereby easily removing the water-insoluble dirt by rinsing. Due to their dual personality of loving both water and oil, when the surfactant concentration reaches a critical point, called the critical micelle concentration, they gather together to form micellar aggregates. In these aggregates, their hydrophobic tails stay inside to avoid contact with water, while their hydrophilic heads prefer to interact with the water molecules (Figure 1). There are massive different kinds of surfactants, some of which have two hydrophilic heads and two hydrophobic tails, named gemini surfactants (Figure 1b). Some of these surfactants play critical roles in our body in numerous biological processes and applications, and are called biological surfactants. The one that strikes our interest the most is bile salts (BSs). BS differs from head-tail surfactants as they have a rigid hydrophobic region and a hydrophilic region (Figure 1c).

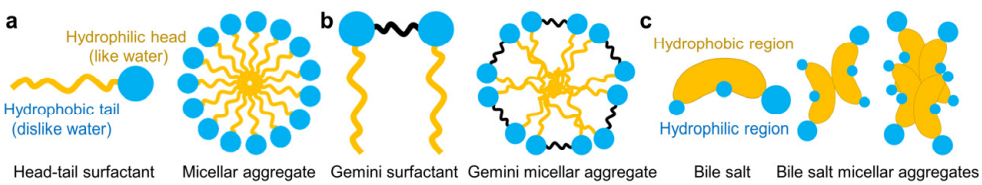

Figure 1 (a) Head-tail, (b) gemini, and (c) bile salt surfactants and their micellar aggregates.

Through enterohepatic circulation, BSs help with food digestion and adsorption in the intestines (Figure 2). They are synthesized from cholesterol and stored in the gallbladder. When digesting and absorbing fat (food), they will go through the small intestine and then the large intestine. Finally, 5% BSs will be lost and 95% will be reabsorbed back to continue their mission in the enterohepatic circulation. However, problems could occur during this reabsorption process, which would result in BS malabsorption, and further cause BS-related diseases such as chronic diarrhea, gallstones, and liver disease.

Commercial drugs with polymeric sequestrants are usually used to treat chronic diarrhea by binding with excess BS, forming complexes and thereby decreasing the BS level in the intestines. However, there are still side effects for patients, for example, severe constipation caused by the water-insoluble complexes formed between excess BS and polymeric sequestrants. Therefore, considering the weakness of the present polymeric sequestrants and in the search for new sequestrants, amphiphilic block copolymers could be a potential candidate. In addition, decreasing BS level through binding with sequestrants can also stimulate the transformation of cholesterol to BS, thereby lowering the level of cholesterol in the body. Therefore, BS sequestrants can also be used to treat hypercholesterolemia.

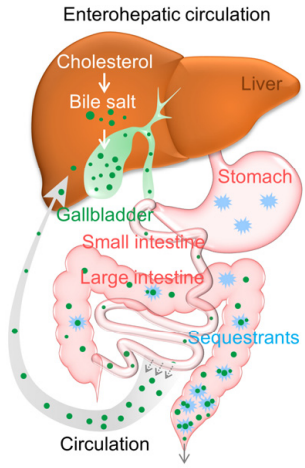

Figure 2 Enterohepatic circulation.

Polymers, composed of a large number of repeating units (monomers) that are linked together by chemical bonds, are larger molecules or macromolecules with a high molecular weight. Polymers are used everywhere in our daily life, e.g., plastic water bottles, food bags, wall paints, glasses, and so on. Amphiphilic diblock copolymers comprise two blocks linked by chemical bonds. Similar to low molecular weight surfactants, amphiphilic block copolymers also love both water and oil because they have both hydrophobic and hydrophilic blocks (see Figure 3). Therefore, they can also self-associate to form micellar aggregates in aqueous solutions as a result of this block incompatibility.

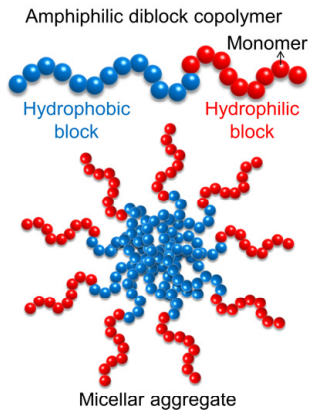

Figure 3 Amphiphilic diblock copolymer and its micellar aggregate.

Mixing amphiphilic block copolymers and surfactants in aqueous solutions will enrich the aggregation behaviors of the individual components especially when involving the oppositely charged components. The idea of using oppositely charged block copolymers as new BS sequestrants is therefore based on the physico-chemical fundamentals of mixed solutions of amphiphilic block copolymers and biosurfactants, i.e., BSs.

All in all, based on the background of the search for new BS sequestrants, this thesis has investigated the amphiphilic block copolymer-BS aqueous systems systematically from a physico-chemical perspective. For the sake of comparison, a system containing

the same copolymer and a conventional head-tail surfactant was also studied. In addition, as biosurfactants, many reported studies on BSs have been aimed at applying BS-related studies to biomedical applications. Thus, to further understand the BS aqueous solution properties and explore their biological nature, i.e., their chirality, chiral gemini surfactant-BS systems were also investigated in this thesis.

中文科普简介

表面活性剂是一种两亲分子，其通常含有亲水基团（头部）和疏水基团（尾部）。因此，它们同时喜欢水和有机溶剂，即它们在水和有机溶剂中均可溶（图 1a）。这种亲水亲油的独特性质使得它们被广泛地应用在家用洗涤剂和化妆品配方中。以洗衣服为例，当我们使用洗衣液时，其中的表面活性剂分子可以作为“桥梁”同时将水溶性和水不溶性（油渍）污垢抓住，从而通过冲洗轻松地去除衣服上的污垢。由于这种亲水亲油的独特性质，当表面活性剂分子的浓度在水溶液中达到一定临界值时，即临界胶束浓度，它们就会聚集在一起形成一种胶束状聚集体（图 1）。在这种结构中，它们的疏水尾部会倾向于呆在胶束内部以避免与水接触，因为疏水尾部不喜欢水，而它们的亲水头部则非常乐意地呆在胶束的外层以便与水相互作用。表面活性剂的种类非常多，除了上述的单头单尾的链状结构外，还有两个亲水头部两个亲水尾部的结构，称为双子（gemini）表面活性剂（图 1b）。还有一类表面活性剂在人体生物过程及维持我们身体健康中扮演着重要的角色，它们被称为生物表面活性剂，例如胆汁盐（bile salt）。不同于头-尾链状表面活性剂，胆汁盐具有亲水区域和刚性的疏水区域（图 1c），这也就为其赋予了特殊的表面活性及自组装能力。

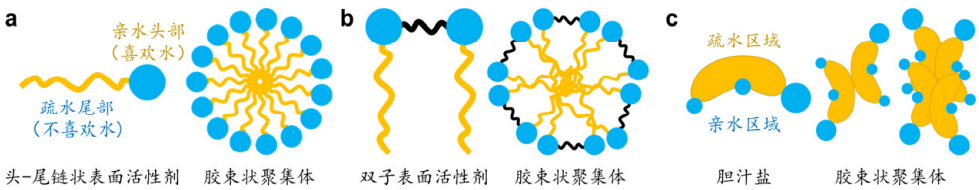

图1 (a) 头-尾，(b) 双子和 (c) 胆汁盐表面活性剂以及它们的胶束状聚集体。

胆汁盐在人体的肝肠循环中起着关键的作用，它们通过促进食物在肠道内的消化吸收来维持我们正常的身体机能（图 2）。胆汁盐通过胆固醇合成于肝脏并储存在胆囊中，他们经过小肠和大肠对食物中的脂肪进行消化吸收。5%的胆汁盐会在这个过程中被排出体外而剩余 95%的胆汁盐在肠道中又重新被吸收返回肝脏进行新一轮的肝肠循环。然而，在这个过程中如果胆汁盐吸收不良，则可能会引起一些与胆汁盐相关的疾病，例如慢性腹泻、胆结石和肝脏疾病等。

含有聚合物螯合剂的药物通常被用于治疗慢性腹泻病，通过其与过量的胆汁盐结合形成复合物排出体外从而降低肠道中胆汁盐的含量。然而这些螯合剂与胆汁盐形成的复合物通常都不溶于水，因此目前的药物会对病人产生严重便秘的副作用。所以，探索新型胆汁盐螯合剂对于治疗胆汁盐相关的疾病至关重要，而水溶性双亲嵌段聚合物被认为是一种很有潜力的候选者。

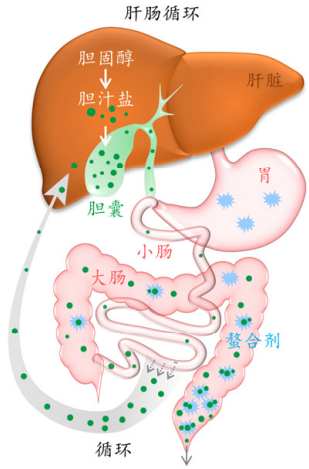

图2 肝肠循环过程。

聚合物（高分子化合物）是一种大分子并具有较高的分子量，由许多重复单元（单体）通过化学键连接在一起而组成。聚合物在我们日常生活中随处可见，例如，我们日常用的塑料水杯，食品袋，墙漆，保鲜膜等都含有高分子化合物。双亲二嵌段共聚物是众多聚合物中的一种，其包含两个由化学键连接的链段。与小分子表面活性剂相似，双亲嵌段共聚物也具有亲水亲油的特性，因为它们同时具有亲水和疏水的链段。因此，由于链段的不相容性，它们也可以在水溶液中自缔合形成胶束状聚集体（图 3）。

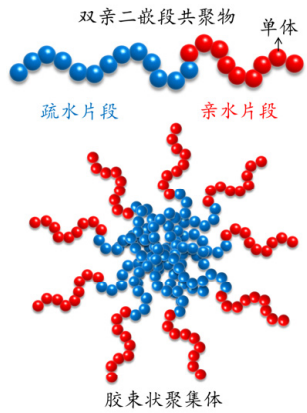

图3 双亲二嵌段共聚物及其胶束状聚集体。

将双亲嵌段共聚物和表面活性剂在水溶液中混合可以丰富其各自的聚集行为，尤其是当它们带有相反的电荷时，它们的聚集行为会更加引人注目。因此，从基础的物理化学角度去研究双亲聚合物和生物表面活性剂胆汁盐混合体系的相互作用和聚集行为可以为探索嵌段聚合物作为新型胆汁盐螯合剂的可能性奠定基础。

基于探索新型胆汁盐螯合剂的研究背景，本论文从物理化学角度对带相反电荷的嵌段聚合物-胆汁盐水体系进行了系统性研究。作为参考体系，本论文也涉及了嵌段聚合物和传统的头-尾链状表面活性剂水体系的研究。此外，作为生物表面活性剂，胆汁盐被应用于生物医药领域的研究也备受关注。因此，为了进一步理解胆汁盐的水溶液行为并探索其生物学本质，即手性，本论文还对手性双子表面活性剂和胆汁盐水体系进行了系统性研究。

List of publications

This thesis is based on the following publications, referred to in the text by their Roman numerals:

I. **Block copolymers as bile salt sequestrants: Intriguing structures formed in a mixture of an oppositely charged amphiphilic block copolymer and bile salt**

Karin Schillén,* Luciano Galantini,* **Guanqun Du**, Alessandra Del Giudice, Viveka Alfredsson, Anna M. Carnerup, Nicolae V. Pavel, Giancarlo Masci, Bo Nyström

Phys. Chem. Chem. Phys. **2019**, *21*, 12518–12529.

II. **Condensed supramolecular helices: The twisted sisters of DNA**

Guanqun Du, Domagoj Belić, Alessandra Del Giudice, Viveka Alfredsson, Anna M. Carnerup, Kaizheng Zhu, Bo Nyström, Yilin Wang, Luciano Galantini,* Karin Schillén*

Angew. Chem. Int. Ed. **2021**, *60*, XXX–XXX.

III. **Effect of temperature on the association behavior in aqueous mixtures of an oppositely charged amphiphilic block copolymer and bile salt**

Guanqun Du, Alessandra Del Giudice, Viveka Alfredsson, Anna M. Carnerup, Nicolae V. Pavel, Watson Loh, Giancarlo Masci, Bo Nyström, Luciano Galantini,* Karin Schillén*

Polymer **2020**, *206*, 122871.

IV. **Stepwise electrostatically and hydrophobically driven co-assembly in an amphiphilic block copolymer-surfactant system**

Guanqun Du, Alessandra Del Giudice, Bo Nyström, Yilin Wang, Luciano Galantini,* Karin Schillén*

Manuscript

V. Coacervation and chiral recognition in catanionic mixtures of chiral gemini surfactants and bile salt

Guanqun Du, Alessandra Del Giudice, Lili Zhou, Yaxun Fan, Luciano Galantini, Yilin Wang,* Karin Schillén*

Manuscript

Author contributions

I. **Block copolymers as bile salt sequestrants: Intriguing structures formed in a mixture of an oppositely charged amphiphilic block copolymer and bile salt**

GD performed the majority of the experimental work, analyzed the results except for the SAXS data and contributed to the writing of the paper.

II. **Condensed supramolecular helices: The twisted sisters of DNA**

GD performed all the experimental work except for the cryo-ET measurements and reconstruction. GD analyzed the results and wrote the manuscript with input from the co-authors.

III. **Effect of temperature on the association behavior in aqueous mixtures of an oppositely charged amphiphilic block copolymer and bile salt**

GD performed all the experimental work and analyzed the related results except for the SAXS measurements. GD wrote the manuscript with input from the co-authors.

IV. **Stepwise electrostatically and hydrophobically driven co-assembly in an amphiphilic block copolymer-surfactant system**

GD performed all the experimental work except for the SAXS measurements. GD analyzed the results and wrote the manuscript with input from the co-authors.

V. **Coacervation and chiral recognition in catanionic mixtures of chiral gemini surfactants and bile salt**

GD performed all the experimental work. GD analyzed the results and wrote the manuscript with input from the co-authors.

Papers not included in the thesis

I. **Harnessing student motivation to improve students' learning in higher education during the Covid-19 pandemic**

Ebba Ruhe,* Margaret Mcnamee, **Guanqun Du**, Jens Malmborg

Submitted to Högre utbildning

II. **Tools for improving student motivation used during online teaching in higher education due to Covid-19**

Ebba Ruhe, Margaret Mcnamee, **Guanqun Du**, Jens Malmborg

11:e Pedagogiska inspirationskonferen, 9 December, 2021, LTH, Lund University, Sweden.

Abbreviations

BR	Bilirubin IXα
CMC	Critical micelle concentration
CAC	Critical aggregation concentration
C_s	Saturation concentration
CR	Charge ratio
CD	Circular dichroism
Cryo-ET	Cryogenic electron tomography
Cryo-TEM	Cryogenic transmission electron microscopy
DLS	Dynamic light scattering
DSC	High-sensitivity differential scanning calorimetry
^{1}H NMR	Proton nuclear magnetic resonance spectroscopy
IFT	Inverse Fourier transformation
ITC	Isothermal titration calorimetry
LCST	Lower critical solution temperature
MPEG	Methoxy poly(ethylene glycol)
MR	Molar ratio
m or *n*	Polymerization degree
NaDC	Sodium deoxycholate
PAMPTMA(+)	Poly((3-acrylamidopropyl)trimethylammonium chloride)
PDDF, $p(r)$, $p_{cs}(r)$	Pair distance distribution function
PESC	Polyelectrolyte-surfactant complexes
PNIPAM	Poly(*N*-isopropylacrylamide)
SAXS	Small angle X-ray scattering
SDS	Sodium dodecyl sulfate
SI	Supporting information, Supplementary information
SLS	Static light scattering
TCF	Time correlation function
T_{cp}	Cloud point temperature
X	Charge fraction
12-4(OH)$_2$-12	1,4-bis(dodecyl-*N*,*N*-dimethylammonium bromide)-2,3-butanediol

1 Introduction

As biological surfactants, bile salts (BSs) play important roles in many biological processes and applications. They circulate in the body, a process called enterohepatic circulation, and serve as agents to help with fat digestion and fat-soluble vitamin adsorption in the small intestine. However, BS malabsorption can occur if there is a malfunction in this circulation, which will further cause BS-related diseases such as chronic diarrhea, liver disease, and gallstones. Therefore, studies on BS aqueous mixed solutions, especially those consisting of BSs and other amphiphiles, are crucial for our health and for solving BS-related problems. In addition to BS, the other amphiphilic molecules studied in this thesis were thermoresponsive cationic diblock copolymers, a head-tail conventional surfactant, and chiral gemini surfactants.

The purpose for studying interactions from a physico-chemical perspective between BS and oppositely charged polymers or gemini surfactants was to:

- Find potential block copolymers that could be employed as new BS sequestrants to treat BS-related diseases and hypercholesterolemia.
- Achieve supramolecular assemblies that can be used in biomedical applications such as drug loading and delivery, especially when these assemblies possess special properties like chirality and thermoresponsive property.
- Build supramolecular structures with hierarchical structural levels from the bottom up by non-covalent interactions of molecular building blocks.

This thesis starts with a general introduction in **Chapter 1** of BSs, thermoresponsive cationic block copolymers, gemini surfactants, and interactions of surfactants with oppositely charged copolymers or gemini surfactants and **Chapter 2** presents the experimental techniques utilized for the studies. Following these introductory chapters, all studies included in this thesis are summarized and divided into three chapters. The oppositely charged block copolymer-BS systems are summarized in **Chapter 3**. In comparison, **Chapter 4** discusses the interaction of the same block copolymer and a head-tail conventional surfactant. Lastly, **Chapter 5** summarizes the results of the

investigation on gemini surfactant-BS aqueous mixtures, and at the end of the thesis, highlights and conclusions are given as well as an outlook.

1.1 Bile salts

Bile salts are anionic biological surfactants (natural surfactants). As the end-product of the cholesterol metabolism in the liver, they present predominantly in the gallbladder of mammals.[1] BSs are widely involved in various biological processes and applications, but mainly help with fat digestion by acting as emulsifiers and absorption of fat-soluble vitamins in the intestines, thereby facilitating intestinal uptake.[2] Because of their steroidal backbone, BSs are significantly more rigid than conventional surfactants with a head-tail structure (Figure 1.1), where the head and tail represent the hydrophilic and hydrophobic moieties, respectively.[3] This rigidity together with a complex distribution of hydrophobic and hydrophilic regions in the BS molecule imparts specific self-assembly properties to them when in an aqueous solution.

It has been shown that BSs self-assemble into micelles through a stepwise micellization process: a primary step and a second step.[4–6] The pre-micelles are formed at the critical micelle concentration (CMC) in the primary step (CMC_{pre}) and this process can be attributed to the hydrophobic interaction between BS monomers. The secondary step is related to the formation of stable micelles at the CMC, which is ascribed to the combination of hydrophobic interaction and the hydrogen bond effect. Consequently, BSs do not have specific CMC values as classical ionic surfactants; instead their CMC values reported in the literature cover a quite wide range of concentrations.[7] Depending on the type of BSs, the concentration, the pH, and the ionic strength of the solution, BSs can form micelles or aggregates with specific structural arrangements, e.g., globular, rod-like, or tubular morphologies[4,8–10] as well as hexagonal liquid crystalline phase under certain conditions.[11] Due to their molecular architecture, BSs are also used as substrates for the synthesis of an expanded family of rigid amphiphiles with uncommon aggregation behaviors[3,12] and dispersing abilities.[13]

BSs can be classified into three groups according to their conjugation with amino acids and their degree of hydroxylation, namely dihydroxy conjugates (such as glycodeoxycholate and taurodeoxycholate), trihydroxy conjugates (such as glycocholate and taurocholate), and unconjugated forms (such as deoxycholate and cholate).[14] Approximately 60% of BSs in human bile are dihydroxy.[15] By properly choosing BSs from the above categories with regard to their hydrophobicity or hydrophilicity, it is possible to predict, design, tune, and achieve special aggregate structures with specific

properties and functionalities in a study system. Sodium deoxycholate (NaDC) was chosen in the studies (**Papers I–III** and **V**) presented in this thesis. As a comparison to these studies, the conventional head-tail surfactant sodium dodecyl sulfate (SDS) was selected as a model surfactant in **Paper IV**. The molecular structures of NaDC and SDS are shown in Figure 1.1.

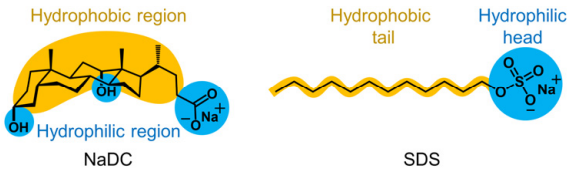

Figure 1.1 Molecular structures of sodium deoxycholate (NaDC) and sodium dodecyl sulfate (SDS). The rigid structure of the BS and the head-tail structure of SDS are exemplified.

As mentioned before, BSs play a key role in the food digestion-absorption process of the small intestine. They function through enterohepatic circulation via reabsorption of BSs (about 95% in a healthy adult) back to the liver. However, different pathologies are associated with disorders in the BS metabolism, such as chronic diarrhea, liver disease, and gallstones, which are caused by the malabsorption of BSs.[16] Diarrhea can be treated by using commercial drugs consisting of cationic polymers, so-called BS sequestrants, aimed at binding the excess BS and thereby decreasing its level in the intestine.[17] However, there are still problems with the current BS sequestrants, e.g., a rather low efficacy, poor compliance, and aggravation of severe constipation caused by the insoluble complexes formed between the sequestrants and BSs. Conversely, stimulating the transformation of the cholesterol to BSs through the binding of excess BSs is favorable in the treatment of hypercholesterolemia disease. Consequently, **Papers I–III** presents the study of the interactions, supramolecular structures, and thermoresponsive properties of oppositely charged block copolymer-BS mixtures to determine whether it would be possible to use cationic amphiphilic block copolymers as new BS sequestrants in the treatment of BS-related diseases. In addition, the mixed complexes formed in these mixtures could be applied in biomedical applications as nanocarriers.

1.2 Thermoresponsive cationic block copolymers

Block copolymers comprise two or more blocks of different polymerized monomers linked by covalent bonds.[18] They have many different architectures including linear, branched (graft and star), and cyclic molecular architectures,[19] among which, diblock

copolymers comprising two distinct blocks have been vastly studied.[20] Due to the diversity of the molecular architectures and availability of monomers, the solution behavior of block copolymers can be tuned based on different blocks and the quality of solvents, giving them unique self-assembly properties. When there exists a difference in the hydrophobicity level of the blocks, the block copolymers will be able to self-associate to form micellar aggregates in aqueous solutions as a result of their amphiphilicity. This is similar to the self-assembly behavior of classical low molecular weight surfactants. Diverse morphologies have been obtained from the self-assembly of amphiphilic block copolymers in solution, for example, spherical micelles, rods, bicontinuous structures, lamellae, vesicles, tubules, "onions", and so on.[21] These aggregates can be widely used in a variety of applications, for instance, in nanotechnology,[22] as nanocarriers, bioactive agents or nanoreactors in drug delivery and gene therapy, etc.[23–25]

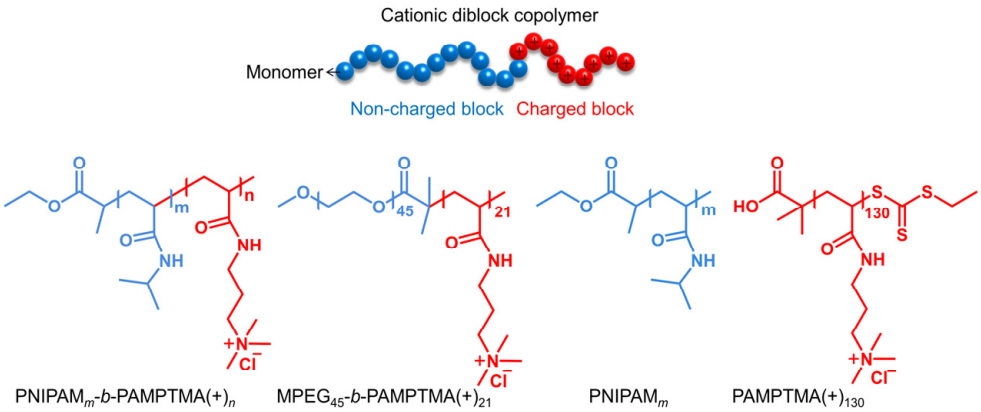

Figure 1.2 Schematic illustration of the cationic diblock copolymer (top). Chemical structures (bottom) of cationic diblock copolymers PNIPAM$_m$-*b*-PAMPTMA(+)$_n$ (m = 120, n = 30; m = 48 or 65, n = 20) and MPEG$_{45}$-*b*-PAMPTMA(+)$_{21}$, nonionic hompolymer PNIPAM$_m$ (m = 97 or 71), and cationic homopolymer PAMPTMA(+)$_{130}$.

The family of block copolymers also includes charged copolymers that have a nonionic (either hydrophilic, hydrophobic, or amphiphilic) and an ionic block. Introduction of a charged block enables the block copolymer to interact electrostatically as polyions (Figure 1.2). Therefore, their self-assembly can be tuned or induced through electrostatic interaction, especially when they are involved in mixtures with oppositely charged species, such as other polymers, surfactants, proteins or nanoparticles.[26–28]

The block copolymers involved in this thesis were poly((3-acrylamidopropyl)trimethyl-ammonium chloride) PAMPTMA(+)-based diblock copolymers, where the nonionic block was composed of either the amphiphilic poly(*N*-isopropylacrylamide) (PNIPAM) or the hydrophilic methoxy poly(ethylene glycol) (MPEG) polymer. These

copolymers are denoted PNIPAM$_m$-*b*-PAMPTMA(+)$_n$ (m = 120, n = 30; m = 48 or 65, n = 20) and MPEG$_{45}$-*b*-PAMPTMA(+)$_{21}$. As a reference, the homopolymer PAMPTMA(+)$_{130}$ and PNIPAM$_m$ (m = 97 or 71) were also studied. The chemical structures of these polymers are shown in Figure 1.2.

The presence of PNIPAM in the block copolymers imparts thermoresponsive properties to the studied systems, which is very attractive especially in drug delivery applications.[29] PNIPAM is known as a thermoresponsive amphiphilic polymer, and the thermoresponsive behavior and aggregation are directly related to its aqueous solubility which depends on the lower critical solution temperature (LCST). The LCST for the PNIPAM polymer is usually stated to be ~ 32 °C.[30–33] Below the LCST, the PNIPAM is soluble in water because of a favorable hydrogen bond interaction between its amide groups and water molecules. However, upon heating, the fraction of the hydrogen-bonded water molecules covering the polymer chain[34] decreases and the intramolecular amide-amide hydrogen bonds formed within the polymer chain, i.e., dehydration of the polymer chain in dilute solution occurs. Consequently, water becomes a poor solvent for PNIPAM, causing the coil-to-globule transition of the PNIPAM polymer.[35] This temperature-induced transition is associated with phase separation or a demixing phenomenon, i.e., the dilute solution becomes turbid at temperatures above its cloud point temperature (T_{cp}).[33]

The phase transition temperature is related to the molecular weight, polydispersity and concentration[36] of the PNIPAM polymers, the copolymerization of PNIPAM with other polymers, and the choice of functional monomers in the copolymerization. Attaching a block (e.g., charged) to the PNIPAM polymer is an effective way to tune the transition temperature as well as the novel characteristics, thereby enabling the PNIPAM-based copolymers to be optimal for the desired applications. For example, biomedical applications like drug delivery[37] can benefit from the fact that the transition temperatures of the PNIPAM-based block copolymers can be modulated to be close to body temperature.

In this thesis, the cationic PAMPTMA(+) block was introduced to the PNIPAM polymer. The formation of copolymer-BS mixed complexes with supramolecular structures and thermoresponsive properties could be promising for the aforementioned applications as BS sequestrants.

1.3 Gemini surfactants

Gemini surfactants generally contain two hydrophilic heads, two hydrophobic tails and a spacer that binds the two head groups together by covalent bonds (Figure 1.3). The head groups can be positively and/or negatively charged or nonionic. The spacers can be of different nature, e.g., flexible chains of methylene groups, rigid, polar, and nonpolar groups.[38] This kind of surfactant was firstly reported by Bunton et al.,[39] but was later named "Gemini" by Menger and Littau in 1991.[40] It has been reported that these surfactants could be several orders of magnitude more surface-active than the corresponding counterpart single-chain surfactants.[41] Thereby, gemini surfactants possess a higher surface activity, lower CMC values, lower Kraff points, a stronger interaction with oppositely charged surfactants, diverse aggregation behaviors and unique rheological properties.[40,42] In addition, their interfacial activity and molecular aggregation property can be finely tuned by adjusting the three structural elements: i.e., two hydrophilic head groups, two hydrophobic chains, and one spacer,[43,44] to obtain desired physico-chemical properties for specific applications. Based on these superior performances, gemini surfactants can be applied in gene transfection,[45] oil recovery,[46] drug delivery,[47] antimicrobial materials,[48] and so on.[38]

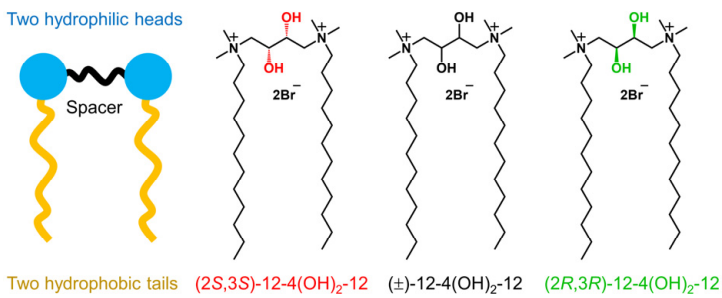

Figure 1.3 Schematic illustration of the gemini surfactant and chemical structures of three gemini surfactants: (2*S*,3*S*)-12-4(OH)$_2$-12, (±)-12-4(OH)$_2$-12, and (2*R*,3*R*)-12-4(OH)$_2$-12.

Chirality is one of the most fascinating phenomena found in nature, and most life processes are directly governed by chiral interactions between biomolecules.[49] Therefore, introducing a chiral center to gemini surfactants enable them to be more appealing in biomedical applications. This can be attributed to the fact that chiral gemini surfactants possess superior properties from both conventional gemini surfactants and chiral molecules. Chiral gemini surfactants can self-assemble into a rich variety of assemblies, e.g., micelles,[50,51] bilayers,[52] vesicles,[53] LB films,[54] tubules,[55] and so on. Since chirality has a structure-directing power to promote the self-assembly of

monomers into aggregates, the stability and growth of aggregates formed by chiral gemini surfactants can then be intimately associated with their chirality.[56]

The chiral gemini surfactants studied in this thesis were 1,4-bis(dodecyl-*N*,*N*-dimethylammonium bromide)-2,3-butanediol (12-4(OH)$_2$-12) including two enantiomers denoted (2*R*,3*R*)-12-4(OH)$_2$-12 and (2*S*,3*S*)-12-4(OH)$_2$-12, and the racemate denoted (±)-12-4(OH)$_2$-12. The racemate was a mixture of two enantiomers with a 1:1 mixing ratio (Figure 1.3). These gemini surfactants have two positive charges on their head groups, allowing them to interact with oppositely charged biosurfactants, here BS, through electrostatic interactions. In addition, as BSs are also chiral molecules, chiral effects are therefore expected to appear in the gemini surfactant-BS system. The mixed aggregates of the gemini surfactant-BS systems exhibiting chiral properties can hopefully be applied in chiral recognition, drug delivery, and other applications.

1.4 Polymer-surfactant interactions

Due to the richness in structural features of both surfactants and charged polymers (polyelectrolytes), it is evident that their mixtures will result in a variety of structurally different co-assemblies.[26] The polyelectrolyte and surfactant complexes (PESCs) formed in these mixtures have been applied in numerous industrial areas such as pharmaceutical formulations, home and personal care, detergents, paints, food products, and other industrial areas.[57]

The interaction of polyelectrolytes with oppositely charged surfactants in aqueous solutions and the formation of PESCs have been a topic in colloid research for more than 40 years.[58,59] The topic has mainly focused on binding mechanisms, assembled structures of the PESCs, phase behaviors, rheology properties, and applications.[27] All these aspects are intimately related to the intermolecular interaction between the oppositely charged components in aqueous solutions, which is based on electrostatic and hydrophobic interactions, and mainly driven by the entropic gain due to the release of small counterions and water molecules.[57,60–62] However, other interactions such as hydrogen bonding and van der Waals forces can also have an impact on the interaction processes.[57]

As mentioned before, the association behavior and co-assembly in oppositely charged polymer-surfactant systems provide a versatile platform for the formation of a variety of colloidal aggregates soluble in water with unique structures, functionality and biocompatibility. Soluble mixed complexes, sometimes with highly ordered internal structures,[57,63] e.g., cubic,[64] hexagonal,[65,66] can be obtained by tuning the intermolecular

interactions.[27] This can be achieved by varying the molecular weight, charge density and functional groups of the polyelectrolytes,[67] the architecture of the surfactant (head-tail or steroidal) and mixture composition,[68] or via the addition of non-ionic surfactants.[64,69] The internal ordered structures can provide a large surface area, which enables the particles to solubilize high concentrations of hydrophobic molecules, proteins, drugs, or peptides, thereby making them useful in a wide range of medical applications, such as drug loading, delivery and release, gene therapy, and so on.

In order to employ polyelectrolyte-surfactant colloidal complexes for these medical applications, it is important that the oppositely charged species are biocompatible and a controllable self-assembly in dilute aqueous conditions is also particularly desirable.[70] Therefore, the water-soluble charged block copolymer-BS mixed complexes obtained in this thesis, with highly ordered internal structures are expected to be used in biomedical related applications as biocompatible nanocarriers.

1.5 Surfactant-surfactant interactions

As mentioned in **Chapter 1.1**, BSs are important biosurfactants possessing superior aggregation behaviors in aqueous solutions under certain conditions due to their special steroidal molecular structures. However, they form small micelles in dilute solutions in the CMC of 5–20 mM with a relatively small aggregation number of 2–12, resulting in small hydrophobic domains.[3] This limits the usage of BSs in drug delivery when considering the loading ability.[71,72] Nevertheless, mixing BSs with oppositely charged surfactants can be one effective way to improve their performances in biomedical applications.

With many appealing properties, the cationic gemini surfactants (**Chapter 1.3**) are good candidates to help BSs improve their performances in dilute aqueous solutions. There are several studies on gemini surfactant-BS systems reported in the literature.[71,73–77] The combination of BSs and gemini surfactants provides a useful model to explore the relationship between the aggregate morphology and the component structure, as both BS and gemini surfactant are unconventional surfactants rich in structural options through synthesis or post-modification.[75]

In general, mixed surfactants with oppositely charged species, often called catanionic surfactant mixtures, have been extensively studied due to their diverse phase behaviors, interesting assemblies, and synergistic physico-chemical properties. This brings about their widespread technological and biomedical applications.[78–80] Strong synergistic effects observed for their bulk and surface properties originate mainly from strong

electrostatic attractions between oppositely charged head groups of surfactant molecules, while other factors such as the molecular packing geometry, hydrophobic interaction, and hydrogen bonding can also have an impact.

A large number of aggregate structures such as rod-like micelles, vesicles, lamellar phases, and nanodiscs can be prepared by controlling these interactions between oppositely charged surfactants. However, phase separation is often observed in these mixtures over certain concentration ranges or molar charge ratios. Particularly, precipitation (liquid-solid associative phase separation) usually occurs when opposite charges reach the equimolar point, which sometimes limits the use of the systems in practical applications.[81] Conversely, the coacervation, i.e., liquid-liquid associative phase separation, in catanionic mixtures, can be appreciated due to its widespread applications in water treatment,[82] cosmetic and food formulation,[83] protein purification,[84] and pharmaceutical microencapsulation.[85,86]

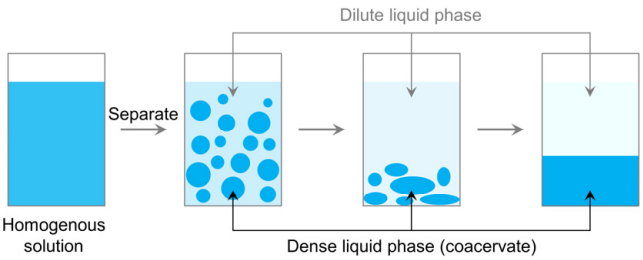

Figure 1.4 Schematic illustration of coacervation or liquid-liquid associative phase separation.

Coacervation is defined as a process during which a homogenous colloidal solution separates into two immiscible liquid phases (Figure 1.4), i.e., a liquid-liquid phase separation, giving rise to a dense phase, which is relatively concentrated in colloidal components, called the coacervate, in equilibrium with a dilute liquid phase containing less colloidal components.[87,88] The coacervate phase can be present as spherical or amorphous droplets in a turbid solution,[89] or they can coalesce and finally separate macroscopically into a top or bottom liquid phase depending on its density[90] (see Figure 1.4).

Coacervation is usually divided into simple coacervation and complex coacervation. Simple coacervation involves a system of one kind of macromolecule or surfactant that undergoes phase separation. Complex coacervation, on the other hand, consists of at least two oppositely charged colloidal species and is primarily driven by electrostatic attraction. Particularly, it takes place close to the charge neutralization. Coacervation is a subtle balance among electrostatic attractions, hydrophobic interactions, hydrogen bonds, van der Waals forces, and other weak interactions. It can be suppressed when

these interactions are reduced, however, precipitation often happens when these interactions are enhanced.[90] It is therefore critical to study the fundamental interaction, aggregate structure, and phase behavior in catanionic surfactant mixtures, especially when these mixtures involve biocompatible species because of their potential in biomedical applications, to gain a deep understanding of the coacervation mechanism.

Studies on gemini surfactant-BS catanionic mixtures involving interactions, mixed aggregate formation, phase transition have been reported in previous studies,[71,73–77,91] however, a few coacervation phenomena were observed in these studies.[73,91] Studies on biosurfactant-based coacervation and the coacervates with chiral properties formed in mixtures of BSs and chiral gemini surfactants have so far not been reported in the literature, which motivated the investigation described in **Paper V**. In this study, the interactions, diverse phase behaviors including coacervation, co-assembled structures, and chiral performances were explored in mixtures of NaDC and three oppositely charged gemini surfactants with different chirality. This study was also a fundament on exploring more potential applications of gemini surfactant-BS systems.

2 Experimental methods

This chapter presents the main techniques used in this thesis as a general overview. The significance of these different techniques and their important features are explained and emphasized in varying depths. Static and dynamic light scattering (SLS/DLS), and turbidimetric titration were used to investigate the aqueous phase behaviors of the studied systems. Cryogenic transmission electron microscopy (cryo-TEM), cryogenic electron tomography (cryo-ET), and small angle X-ray scattering (SAXS) were utilized to explore the morphology and structure of the aggregates. It should be emphasized that by means of the cryo-ET technique, aggregate structures can be imaged from three dimensions (3D), and the 3D morphology can be reconstructed later.

Two calorimetric techniques were employed to study the systems from a thermodynamic point of view. One was high-sensitivity differential scanning calorimetry (DSC), which was used to determine the phase transition temperature and the enthalpy changes during the transition process. The other was isotherm titration calorimetry (ITC), from which the thermodynamic interaction information was acquired and which is a helpful technique for understanding the mixed complex formation in polymer-surfactant or gemini surfactant-BS systems. To obtain information on the chirality and to confirm the chiral properties of the studied systems, circular dichroism (CD) was employed. As a complementary method, electrophoretic mobility measurements were carried out to gain information on the chemical compositions of the mixed aggregates. In addition, optical microscopy (OM) was a useful method to confirm the formation of coacervate droplets in the gemini surfactant-BS system.

2.1 Scattering techniques

Scattering techniques such as light and X-ray scattering, have become leading techniques for the characterization of structures, interactions, and dynamics in soft matter systems containing colloids, polymers, surfactants, and biological macromolecules. Due to several advantages, e.g., a relatively strong signal and rapid acquisition of statistically relevant data, the experiments give a representative overview

of the existing structure, and so on.[92] As a result of the interaction between the electromagnetic radiation and the matter, the scattering methods can be divided into different categories depending on the radiation sources. The radiation can be visible light obtained from lasers giving plane-polarized light in the wavelength (λ) range of 250–700 nm, X-rays with λ around 0.05 to 1 nm, or neutrons with λ range from 0.1 to 1 nm.[93] Each source interacts with different parts of the atom, light and X-rays interact with the electrons through the difference in polarizability or electron density, respectively, between object and solvent, which gives rise to contrast in each case. Neutrons, on the other hand, interact with the nuclei of atoms and they are therefore sensitive to different isotopes.[92] Based on the length scale of the colloidal particle (ranging from nanometers up to several micrometers), scattering techniques with suitable radiation sources can be chosen to obtain information about the particles such as the size, morphology, structure, and interaction.

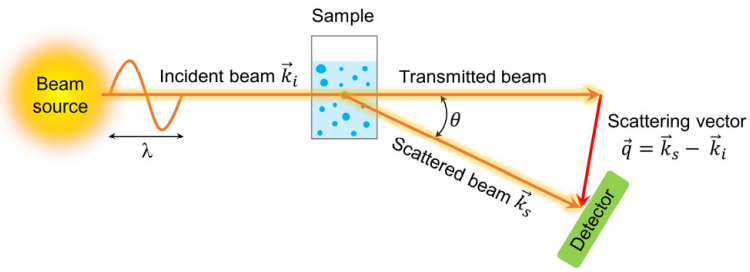

Figure 2.1 Schematic illustration of a scattering experiment and definition of the scattering vector $\vec{q}$. θ is the scattering angle.

When a beam of an incident electromagnetic radiation impinges a solution of colloidal particles, part of it can interact with the particles in two ways, and the remainder of the radiation will pass through the solution without interacting with the particles (transmitted beam),[94] as depicted in Figure 2.1. The incident radiation can either be absorbed as a result of the excitation of the atoms in the particles, which is the basis of spectroscopic techniques, or be scattered by the particles through interaction with them either elastically or inelastically. Elastic scattering means that there is no energy loss during the scattering process and the scattered radiation thus has the same wavelength as the incident one. This is valid for the light scattering methods (DLS and SLS) as well as SAXS used in this thesis.

In a typical scattering process, the electric field of the incident radiation, which is a plane wave at position $\vec{r}$ and time t can be expressed as:[94]

$$\vec{E}_i(\vec{r}, t) = E_0 exp\left[i(\vec{k}_i \cdot \vec{r} - \omega t\right] \quad (2.1)$$

where E_0 is the electric vector, $\vec{k}_i$ is the propagation vector of the incident light and ω is the angular frequency.

It will be scattered by the point scatterer which results in a spherical scattered wave with a wave vector of $\vec{k}_s$.

The scattered radiation is collected by a detector at a specific scattering angle θ, the relative position of which can be experimentally varied as depicted in Figure 2.1.

The difference between $\vec{k}_i$ and $\vec{k}_s$ defines the scattering vector $\vec{q} = \vec{k}_s - \vec{k}_i$. Since $|\vec{k}_i| = |\vec{k}_s| = k = 2\pi/\lambda$, for an elastic scattering process, the magnitude of $\vec{q}$ can be derived from the scattering geometry (Figure 2.1):

$$|\vec{q}| = q = \frac{4\pi}{\lambda}\sin\left(\frac{\theta}{2}\right) \tag{2.2}$$

In a real scattering experiment, the incident radiation is scattered by numerous particles. The radiation scattered from single point scatterers with varying spatial positions in the sample or from diverse scattering centers within larger particles will have a different distance to travel to the detector, thereby resulting in a constructive or destructive interference between the scattered waves. The extent of the interference is reflected by the fact that the amplitude of the electric field of the scattered radiation $E_s(\vec{R}, t)$ will depend on the scattering angle θ, i.e., the scattering vector $\vec{q}$. $E_s(\vec{R}, t)$ from N particles in the scattering volume V with the centers of mass at time t, to a point detector at position $\vec{R}$ in the far field is given by:[94]

$$E_s(\vec{R}, t) = -E_0 \frac{exp[i(kR - \omega t)]}{R} \sum_{j=1}^{N} b_j(\vec{q}, t)\, exp\left[-i\vec{q} \cdot \vec{R}_j(t)\right] \tag{2.3}$$

where $\vec{R}_j(t)$ is the position vector of the particle j at time t and $b_j(\vec{q}, t)$ is the scattering length of particle j defined as:[94]

$$b_j(\vec{q}, t) = \int_{V_j} \Delta\rho(\vec{r}_j, t)\, exp(-i\vec{q} \cdot \vec{r}_j) d^3 r_j \tag{2.4}$$

where $\Delta\rho(\vec{r}_j, t)$ can be regarded as a measure of the local density of scattering material, which is the contrast term in each of the different scattering methods mentioned before.

Unfortunately, the amplitude of the scattered electric field is not an accessible parameter in real experiments. Instead, the scattering intensity is measured directly by

the scattering instruments. The relationship between scattering intensity and the electric field is given by:[94]

$$I_s(\vec{q},t) = |E_s(\vec{q},t)|^2 \tag{2.5}$$

Combining Equations (2.3) and (2.5), the scattering intensity can be expressed as:[94]

$$I_s(\vec{q},t) = \left(\frac{E_0}{R}\right)^2 \sum_{j=1}^{N}\sum_{k=1}^{N} b_j(\vec{q},t)b_k(\vec{q},t)\, exp\{-i\vec{q}\cdot[\vec{R}_j(t) - \vec{R}_k(t)]\} \tag{2.6}$$

This is the instantaneous scattering intensity, for size and structural information of colloidal particles in a solution. The time-averaged scattering intensity $\langle I_s(\vec{q})\rangle$ (here also denoted $I_s(q)$) is required when assuming the colloid particles to be spatially isotropic on average, and is written:[94]

$$\langle I_s(\vec{q})\rangle = \left(\frac{E_0}{R}\right)^2 \langle \sum_{j=1}^{N}\sum_{k=1}^{N} b_j(\vec{q})b_k(\vec{q})\, exp[-i\vec{q}\cdot(\vec{R}_j - \vec{R}_k)]\rangle \tag{2.7}$$

In the following subchapters, the approximation, data analysis, and settings for each scattering technique used in this thesis is explained in detail.

2.1.1 Static light scattering

In static light scattering, the radiation source is a laser beam of monochromatic plane-polarized light with a wavelength in the visible light range; in this thesis, the wavelength of the laser beam was 632.8 nm. By measuring the angular dependence of the scattering intensity as a spatial and time average, we can determine the molar mass M, radius of gyration R_g of the objects under investigation and their mutual interaction (in terms of the second virial coefficient A_2). Theoretical limitations of the scattering angle are $0° < \theta < 180°$, intensity from θ = 0° corresponds to the unscattered (transmitted) light, while from θ = 180° the light is scattered directly back into the laser. However, in practice, it is almost impossible to reach the angles closest to 0° or 180°, the measurements are thus usually carried out at $15° < \theta < 145°$, depending on the geometry of each specific instrument.

In SLS experiments, the measured scattering intensity can be normalized against a reference (usually toluene) and expressed as the excess Rayleigh ratio ΔR_θ:[92]

$$\Delta R_\theta = \frac{I_s(q) - I_0(q)}{I_{tol}(q)} R_{tol} \left(\frac{n}{n_{tol}}\right)^2 \tag{2.8}$$

where $I_s(q)$, $I_0(q)$, and $I_{tol}(q)$ are the time-averaged scattering intensities of the solution, the solvent, and toluene at a specific q, respectively. R_{tol} is the Rayleigh ratio of toluene, n and n_{tol} are the refractive indices of the solution and solvent, respectively, and are here used to correct the difference in scattering volume between the solution and the reference.

The size, molecular weight, and interaction of the particles are all associated with the excess Rayleigh ratio, which can thus also be expressed as:[94,95]

$$\Delta R_\theta = KMCP(q)S(q) \tag{2.9}$$

where K is the optical constant that is related to the instrumental setup and the sample (it contains the contrast factor $\frac{dn}{dc}$ mentioned earlier), C is the solute mass concentration, $P(q)$ $(= 1 - \frac{(qR_g)^2}{3} + \cdots)$[96] is the form factor, which expresses the intraparticle interference effects, and is related to the size and shape of the particles, $S(q)$ is the structure factor representing the contribution of the interparticle interference to the scattering intensity: $S(q) = 1/(1 + 2A_2MC + \cdots)$,[97] where A_2 is the second virial coefficient. The value of A_2 is a measure of the nonideality of the solution or of the interaction forces between particles in a solution. When A_2 is positive the solute-solvent interactions are more favorable than the solute-solute interactions and the interparticle interaction is repulsive, otherwise, when negative, the reverse is true and the interparticle interaction is attractive.

For very dilute solutions (no interparticle interaction, i.e., $S(q) = 1$) of small particles (size smaller than $\lambda/20$), the scattered intensity is independent of the scattering angle and depends only on M of the particle. Moreover, it is proportional to the total number of scattering particles. The molar mass can be determined at $\theta = 0°$, and $C = 0$. This can be achieved by measuring the scattering intensity at different angles, extrapolating to zero scattering angle for each sample and thereafter performing an extrapolation to infinite dilution. In this case, the scattering is said to be isotropic and the particles that scatter the light are termed isotropic scatterers.

However, for dilute solutions of non-interacting large particles, the scattered intensity is no longer independent of the scattering angle due to intraparticle interference ($P(q) \neq 1$ but still $S(q) = 1$). The angular dependence increases with increasing particle size, and in this case, the size and shape of the particles are reflected in the form factor $P(q)$ from which information on the radius of gyration of the particle can be obtained (see Equation (2.9)).

For both cases cited above, interparticle interference effects cannot be ignored at finite particle concentrations (i.e., $S(q) \neq 1$) and therefore, information of the type of interparticle interaction can be acquired from determining A_2 as mentioned in Equation (2.9).

Due to the complexity in size, shape and internal structure of the different aggregates studied in this thesis, the aforementioned standard theoretical approaches to the analysis of SLS data cannot be easily applied. Hence, the total scattering intensity (without subtracting the solvent scattering) was used to follow the overall phase behaviors, e.g., the phase transition upon increasing temperature, relative changes in aggregate size at different compositions, and so on.

2.1.2 Turbidimetric titration

Turbidity is the cloudiness of a particle solution, determined by the amount of light that passes through the solution and caused by the light scattering from the suspended non-absorbing particles, which therefore gives the solution a cloudy appearance. Turbidity assessments are based on the measurements of the transmittance (T), which is defined as the ratio of transmitted light intensity (I_t) to incident light intensity (I_0):[98]

$$T = \frac{I_t}{I_0} = \frac{I_0 - I_s}{I_0} \tag{2.10}$$

where I_s is the intensity of scattered light (see Equation 2.6). The turbidity values are usually expressed as $(1 - T) \times 100\%$ or $100 - \%T$.

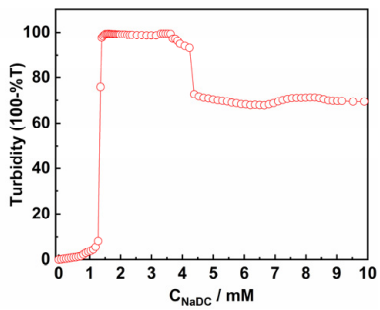

Figure 2.2 Turbidity ($100 - \%T$) as a function of NaDC concentration (C_{NaDC}) of the gemini surfactant-BS solution when titrating a concentrated NaDC solution into a gemini surfactant solution.

Studying solution behavior by turbidimetric titration is a very useful and convenient way to monitor a phase transition process, such as the occurrence of coacervation (liquid-liquid phase separation) or precipitation (liquid-solid phase separation), in a

colloidal mixed solution. In **Paper V**, the turbidity was measured by turbidimetric titration to study the phase transition and coacervation in gemini surfactant-BS mixtures (see Figure 2.2).

2.1.3 Small angle X-ray scattering

The small angle X-ray scattering technique can generally access the structural information of the particles in smaller length scales compared to static light scattering. This is because X-ray sources having much smaller wavelengths (typically 0.1–0.2 nm) than light sources, which results in larger q ranges, and since q has dimensions of the inverse of length, q^{-1} can be interpreted as a rough measure of the probed length scales. In SAXS experiments, the obtained result is the scattering intensity as a function of q as described in Equation (2.11):

$$I(q) = N_p {V_p}^2 \Delta\rho^2 P(q) S(q) \tag{2.11}$$

where N_p is the number of particles per volume, V_p is the volume of a particle, $\Delta\rho$ is the difference in scattering length density (SLD) between the particle and the solvent, and $P(q)$ and $S(q)$ are the form factor and structure factor as described before.

Dissimilar to the contrast used in SLS experiments, where differences in refractive indices are employed, SLD is utilized as the contrast in SAXS experiments and expressed as $\Delta\rho$ in Equation (2.11) according to:[94]

$$\Delta\rho(\vec{r}_j, t) = \frac{r_e}{V_p}\left(\sum_j Z_j - \sum_k Z_{k,L}\right) \tag{2.12}$$

where $r_e = 2.81794 \times 10^{-5}$ Å is the electron radius, and Z_j and $Z_{k,L}$ are the numbers of electrons in the atoms of the particle and the solvent, respectively.

The analysis of SAXS data can be done in numerous ways, and different methods give various levels of detail, but it also requires many levels of prior knowledge. As mentioned before, q^{-1} can give the length scale information of a measurement, and the dimension of the scattering particles can be estimated from $2\pi/q$. This indicates that larger structural information of the scattering particles can be obtained at low q values, while information about internal or small structures can be acquired at higher q values.

At low enough q values so that $qR_g < 1$, the Guinier approximation[99] is valid and can be used to estimate the R_g of the particles. For non-interacting particles ($S(q) = 1$),

the scattering intensity $I(q)$ depends only on the zero angle scattering intensity $I(0)$ and the R_g, which is given by:[92]

$$I(q) = I(0)e^{\frac{-q^2R_g^2}{3}} \tag{2.13}$$

By using the Guinier plot, i.e., plotting $\ln[I(q)]$ as a function of q^2, the R_g can be obtained in a linear function where the slope of this function is proportional to R_g^2.

In the intermediate q regions, where the Guinier regions may not be seen due to the larger size of the particles. This means that the overall size of the particles cannot be determined. Nevertheless, the q dependence of the scattering curve in this region can give information about the shape of the particles. For example, a slope of q^{-1} corresponds to a cylindrical shape of the particle, while a slope of q^{-2} reveals the lamellar structure of the particles.

At the higher q regions, the scattering intensity is related to the surface scattering and a slope of q^{-4} can be seen for smooth interfaces. This is known as the Porod region described in the Porod law.[100]

The above-mentioned information of the scattering particles can be directly revealed from the characteristics of the scattering curves. In order to gain more information about the particles, a model-free or model-dependent analysis is generally required. In the model-free analysis, no prior information is needed to fit the data. This type of data analysis is based on the inverse Fourier transformation (IFT) of the scattering intensity, which results in the pair distance distribution function (PDDF) or $p(r)$ describing the geometry of the scattering particles in the real space.[101] For a locally cylindrical particle, the IFT yields the cross-section pair distance distribution function $p_{cs}(r)$, which provides important information on the cross-section structure of the aggregates such as the maximum dimension. This kind of information was obtained in **Papers I–IV** (under the assumption that the structure factor $S(q)$ was 1).

For the model-dependent analysis, there are numerous form factor models available in many software such as SasView[102] and SASfit.[103] Through fitting of the experimental data to a selected model, e.g., a sphere, cylinder or disc, information of the size and shape of the particles can be obtained. However, prior knowledge about the studied systems is sometimes needed in order to find the best $P(q)$ model to use. This can be achieved by combining SAXS with other techniques that can give an indication of the morphological information about the particles, for example, cryo-TEM. In the studied systems, all the above-mentioned data analysis methods were employed at different levels or to various extents.

Bragg diffraction

Colloidal particles with a highly ordered arrangement or internal structure such as the lamellar, cubic or hexagonal phases are often called dispersed liquid crystalline phases. The X-ray scattering intensity from such ordered structures will result in a diffraction pattern with well-defined peaks due to the constructive interference (Figure 2.3); these peaks are known as Bragg peaks and this type of scattering obeys Bragg's law:[104]

$$n\lambda = 2d\sin\left(\frac{\theta}{2}\right) \tag{2.14}$$

Here, n is an integer (diffraction order), d is the distance between the lattice planes and θ is the scattering angle.

A crystal can be described by its unit cell, the smallest repeating unit in the crystal, and the miller indices (h, k, l) denoting how many lattice planes that intersect each unit axis of the cell. For a given structure, e.g., 2D-hexagonal, the distance (d_{hk}, l = 0) between the lattice planes can be related to the miller indices. The relation is given by:[105]

$$d_{hk} = \frac{\sqrt{3}a}{2\sqrt{(h^2 + k^2 + hk)}} \tag{2.15}$$

By combining Equations (2.2) and (2.14), the characteristic distance of the inter-plane can be calculated through $d = 2\pi/q_1$, and the size of the unit cell a, for a 2D-hexagonal phase, can be calculated according to:

$$a = \frac{4\pi}{\sqrt{3}q_1} \tag{2.16}$$

where q_1 is the q value of the first Bragg peak in the X-ray scattering curve.

In practice, the liquid crystalline structures can be determined by the ratios between different Bragg peaks of the particles. For example, in the case of the hexagonal phase, the Bragg peaks in the X-ray scattering curve show the position order of $\sqrt{1}, \sqrt{3}, \sqrt{4}, \sqrt{7}, \ldots$ which is relative to the position of the first Bragg peak at q_1.[92] Studies on the ordered structures showing Bragg diffraction peaks of the investigated systems can be found in **Papers II**, **IV** and **V**.

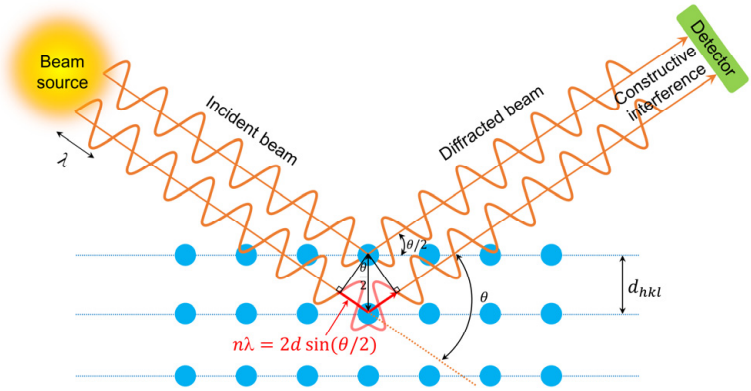

Figure 2.3 Schematic illustration of Bragg diffraction. Two incident beams with identical wavelength and phase reach the crystalline or liquid crystalline phase and are scattered from the lattice planes. The lower beam traverses an extra length of $2d\sin\left(\frac{\theta}{2}\right)$ (marked with red). Constructive interference occurs when this length is equal to an integer multiple of the wavelength of the radiation, i.e., $n\lambda = 2d\sin\left(\frac{\theta}{2}\right)$.

2.1.4 Dynamic light scattering

In dynamic light scattering experiments, the time-dependence of the scattered intensity is measured at different scattering angles. DLS is known as quasi-elastic light scattering but it is still based on an elastic scattering process as in SLS and SAXS, i.e., the wavelength of the scattered light is the same as the incident light. In a DLS experiment, the scattered intensity from a solution of particles shows a time-dependent fluctuation due to the Brownian motion of particles causing concentration fluctuations. Therefore, by studying these intensity fluctuations (Figure 2.4), information on the collective diffusion and hydrodynamic size of the particles can be obtained.

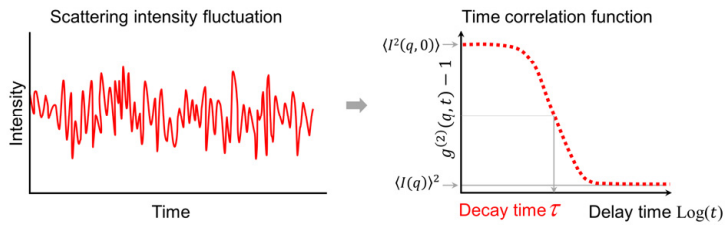

Figure 2.4 Schematic illustration of the scattering intensity fluctuation and a time correlation function of the scattering intensity.

The scattered intensity is collected by using a detector (photomultiplier or avalanche photodiode) and a time correlation function (TCF) is constructed by a digital correlator (Figure 2.4). The normalized TCF of the scattering intensity $g^{(2)}(q,t)$ is defined as:[94]

$$g^{(2)}(q,t) = \frac{\langle I(q,0)I(q,t)\rangle}{\langle I(q)\rangle^2} \tag{2.17}$$

where $I(q,0)$ and $I(q,t)$ are the scattering intensity at time 0 and a delay time t, respectively, while $\langle I(q)\rangle$ is the time-averaged scattering intensity.

The TCF has a characteristic decay time called the relaxation time τ, which describes the mobility feature of the particles (Figure 2.4). Longer τ indicates a slower fluctuation in scattering intensity, thus suggesting a slower motion from larger particles in solution according to Brownian motion theory. Conversely, a shorter τ indicates a faster diffusion of the smaller particles. From this, we can correlate the particle size with the scattering intensity fluctuation.

$g^{(2)}(q,t)$ is related to the normalized electric field autocorrelation function $g^{(1)}(q,t)$ through the Siegert relation:[106]

$$g^{(2)}(q,t) = 1 + \beta[g^{(1)}(q,t)]^2 \tag{2.18}$$

where β (≤ 1) is an instrumental parameter that takes into account the deviation from ideal correlation and the experimental geometry.

For monodispersed spherical particles, $g^{(1)}(q,t)$ can be fitted to a single exponential function as:

$$g^{(1)}(q,t) = e^{-q^2Dt} = e^{-\Gamma t} = e^{-\frac{1}{\tau}t} \tag{2.19}$$

where D is the collective diffusion coefficient of particles, which involves particle interactions at finite solute concentrations and Γ is the decay rate which is the reciprocal of the decay time τ.

The self-diffusion coefficient D_0, sometimes called the "free particle" diffusion constant, can be obtained by extrapolating the D measured at different solute concentrations to zero using its concentration dependence: $D = D_0(1 + k_D C + \cdots)$,[107] where C and k_D are the concentration and concentration coefficient, respectively.

The hydrodynamic radius R_H of a particle can be obtained from D_0 by using the Stock-Einstein equation:

$$R_H = \frac{k_B T}{6\pi\eta D_0} \tag{2.20}$$

where k_B is the Boltzmann constant, η is the viscosity of the solvent and T is the absolute temperature.

An apparent hydrodynamic radius $R_{H,app}$ is obtained if the value of D is used in Equation (2.20) instead of D_0. $R_{H,app}$ is thus affected by both hydrodynamic and thermodynamic interactions.

In a solution that contains polydispersed particles, $g^{(1)}(q,t)$ is a multiexponential function and can be expressed as a continuous distribution of relaxation times in a Laplace transform:

$$g^{(1)}(q,t) = \int_0^\infty A(\tau)\mathrm{e}^{-\frac{t}{\tau}}d\tau = \int_{-\infty}^\infty \tau A(\tau)\mathrm{e}^{-\frac{t}{\tau}}d\ln\tau \qquad (2.21)$$

where $A(\tau)$ is the relaxation time distribution, which can be extracted by an inverse Laplace transformation (ILT).

There are two general types of DLS data analysis: mean size analysis and size distribution analysis. The mean size of the particles can be obtained by the Cumulants method[108] which gives a z-average particle size and also an estimation of the width of the distribution (polydispersity index, PDI). The Cumulants method is suitable for systems where the size polydispersity of the particles is small. The size distribution analysis is usually employed for polydisperse systems and there are various analysis methods based on the inverse Laplace transformation of either the electric field or the intensity correlation function.[109] The best-known packages are CONTIN, a type of Tikhonov regularization originally encoded in FORTRAN by Provencher,[110] NNLS (non-negative least squares, General purpose in Malvern instrument), and REPES[111] (Regularized Positive Exponential Sum), a constrained nonlinear regularization algorithm.

For the purpose of this thesis, the Cumulants method, NNLS, and CONTIN were used to analyze the DLS data in different studies, and which method was chosen was based on the specific feature of each system. Details about the DLS data analysis can be found in the corresponding papers.

2.2 Microscopy techniques

2.2.1 Cryogenic transmission electron microscopy

Cryo-TEM has attracted much attention in recent years and has been widely used for studying the self-assembly behavior of amphiphilic molecules in solution due to its impressive development.[112,113] In 2017, Jacques Dubochet, Joachim Frank and Richard Henderson were awarded the Nobel Prize in Chemistry for their work in developing the cryo-electron microscopy technique that helps researchers image biomolecules.[114] Transmission electron microscopy is most frequently used for the evaluation of the ultrastructure in colloidal and material science.[115] However, in most of the colloidal systems, self-assembled structures of amphiphiles, such as surfactants and amphiphilic block copolymers, are only stable in their native solution state under certain conditions such as concentration, temperature, and pH. Direct imaging of such liquid systems is not possible in a high-vacuum TEM chamber because of the vapor pressure of solvents and molecular diffusion. While it is possible to image samples by completely removing the solvent from the solution, this often results in the deformation or destruction of the assembled structure.[112] Nevertheless, thanks to the successful development of the cryogenic freeze technique in the electron microscopy field, cryo-TEM extends the capabilities of TEM by allowing for *in-situ* imaging of the delicate self-assembled structures of soft matter in liquid systems, providing unique information that cannot be accessed by other techniques. Cryo-TEM measurements can directly provide structural and morphological information of samples in a wide range of length scales, ranging from a few nanometers to several micrometers.

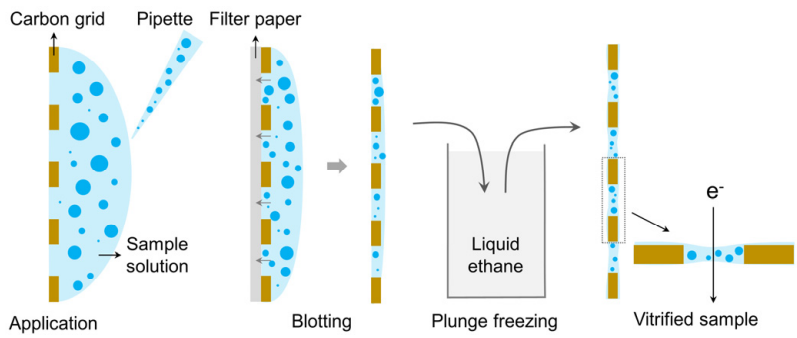

Figure 2.5 Schematic illustration of the cryo-TEM sample preparation process including application, blotting, and plunge freezing to obtain the vitrified sample.

Sample preparation for cryo-TEM is critical for acquiring high-quality images and is a rather sensitive process requiring strict control of the sample environment over the

whole time of preparation, transfer, and electron microscopic investigation. Automatic vitrification systems with controlled humidity and temperature are often required to ensure a reproducible sample preparation procedure.

In the papers of this thesis, the specimens were prepared using an automatic plunge freezer system (Leica Em GP) with the environmental chamber operated at room temperature and 90% relative humidity. As shown in Figure 2.5, during the plunge-freezing process, a droplet of sample solution (approximately 2–5 μL, here 4 μL) was deposited on the carbon-coated grid with a pipette. The excess solution was removed by quick blotting with a filter paper, leaving a thin spanned film in the holes of the grid. The grid was then immediately plunged into liquid ethane (around -183 °C) to ensure rapid vitrification of the sample (i.e., transform it into a glassy state) in its native state and to avoid the formation of crystalline ice.[116] Thereafter, the specimens were transferred intermediately into liquid nitrogen (around -196 °C) and placed in the cold cryo-holder using pre-cooled tools. Subsequently, the cooled holder was quickly inserted into the electron microscope for the image acquisition process. To ensure electron transparency, the vitrified films were usually prepared with typical thicknesses in the order of 100 nm.[117]

In a habitual TEM measurement, the sample is illuminated by an electron beam created from the electronic gun in the microscope column. When the electron beam is focused on the sample by a system of electromagnetic lenses, the interaction occurs between the electrons and atoms of the sample through the scattering of the electrons in three dimensions by the various atoms of the sample. The scattering angles are related to the density and thickness of the sample, which further results in the formation of the image with different brightness and darkness, thereby presenting the structural information of the samples.[118] The transmitted electrons are then projected onto an image recording system/detector and the images of the sample can be captured by a camera system (in this thesis, a bottom-mounted TemCam-F416 camera (TVIPS) using SerialEM).

The contrast of a cryo-TEM image can be attributed to both mass-thickness contrast and phase-contrast mechanisms.[112] The mass-thickness contrast is related to the different abilities of the atoms to scatter electrons in a sample. For amphiphilic colloidal systems, however, it is more difficult to obtain images with high resolutions since both the self-assembled objects and solvents in solutions are mainly comprised of low-atomic-number elements such as carbon, hydrogen, oxygen, and nitrogen. Nevertheless, the dense packing of hydrophobic moieties and the presence of any heavier atoms definitely contribute to the mass-thickness contrast. Phase contrast, on the other hand, can be enhanced by under-focusing the objective lens, which induces a phase shift of the scattered electrons, whereby the self-assembled objects with inner

electron potentials different from the vitreous solvent become visible. Nevertheless, the underfocus may cause optical artifacts and loss of spatial resolution during the imaging process. The resolution of a cryo-TEM image depends on both sample contrast and the electron dose used for capturing images. A slightly higher electron dose can give rise to images with higher resolutions, however, it is important to be aware of the visible electron beam damage in the vitrified films.[117,119]

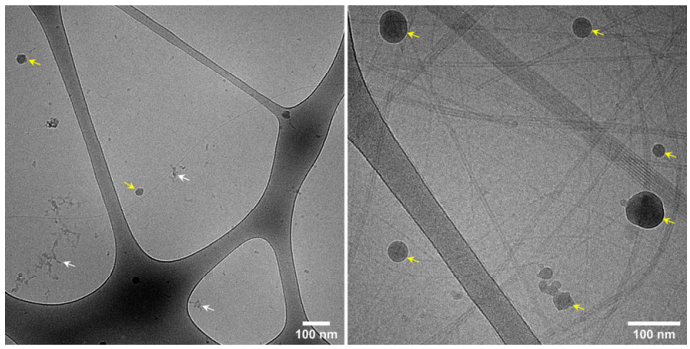

Figure 2.6 Examples of cryo-TEM images with artifacts like cryogen residues (marked with white arrows) and ice contaminations (marked with yellow arrows).

Due to the complicated experimental process of cryo-TEM, which involves sample vitrification, insertion of the sample into the holder, transfer of the holder into the microscope, and image acquisition, various artifacts may occur in the cryo-TEM images. These include cryogen residues (Figure 2.6), which can remain from the plunge freezing process, and ice contaminations (Figure 2.6) from either the freezing process, the phase transition of the vitrified ice into cubic or hexagonal ice, or evaporated water in the column of the TEM.[115] In addition, cryo-TEM images only visualize a small area of a whole sample grid, wherefore a single image should not be overestimated and a series of images that can be representative for the whole sample should be considered for a thorough analysis of the sample.

Moreover, because of the small volume in the hole of the thinner sample film, larger anisometric objects especially with elongated structures may immerse parts of their structure inside the film and/or protrude other parts of their structure outside the film. This would lead to the loss of overview information of the objects, e.g., their size, shape, and internal structure. Hence, it is necessary to perform a series of images and the obtention of structural information from three dimensions of such samples is advised to gain a deep understanding. This could be achieved with the help of different angular views by tilting the sample specimen several times, i.e., performing a tomography measurement.

2.2.2 Cryogenic electron tomography

As mentioned above, cryo-TEM is widely used to study the morphology and structure of objects in colloidal and material science. However, the images obtained in conventional cryo-TEM measurements are 2D projections of 3D objects, thus the true 3D structure of an object may be hidden in 2D images and the overlapped internal structures could make the analysis of complicated nanostructures even more difficult. Thankfully, the emergence of the powerful and versatile cryogenic electron tomography has rendered it possible to visualize the nanostructures in three dimensions and has opened a new window for the analysis of complicated nanostructures.

Generally, in a cryo-ET measurement, images of the object are acquired by tilting the same specimen at different angles and then performing a reconstruction into 3D objects (Figure 2.7), thereby revealing detailed information on the morphology, internal structure, and 3D organization of nanostructures. For this purpose, the images must be aligned with respect to a common origin and tilt axis to correct for relative shifts and rotations between images and to minimize reconstruction artifacts. This can be done with the help of the fiducial markers and usually 6–20 nm colloidal gold particles need to be added to the sample solution prior to vitrification. Once the images are properly aligned, numerical algorithms can be used for the 3D reconstructions.[120]

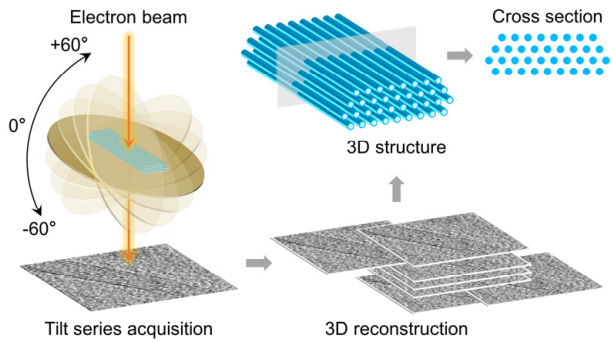

Figure 2.7 Schematic illustration of a typical cryo-ET experiment and image analysis process including the tilt series acquisition and the 3D reconstruction to obtain the 3D structure of the objects from which also the cross-section can be obtained.

In **Paper II**, a series of 2D cryo-TEM images of the same grid area were collected at tilt angles from -60° to +60° at a nominal defocus between -1.5 and -3 µm using the SerialEM software package, and a total of 61 images in 2° increments were recorded for the later 3D reconstructions. To prevent the area of interest from beam damage during total image acquisition, the electron dose per tilt image needed to be carefully evaluated.[121] The electron dose per tilt view was kept < 1.5 electrons/Å^2, i.e., the total

electron dose per imaged area was kept < 120 electrons/Å^2. After the alignment of all images with the aid of 10 or 20 nm Au particles as fiducial markers, the tilt series process and 3D reconstruction were then performed using the IMOD software package.[122] The tomographic reconstructions were carried out with a simultaneous iterative reconstruction technique (SIRT) algorithm after 15 iterations. Data visualization was performed using IMOD and UCSF Chimera.[123]

Due to the complicated arrangement of the supramolecular assemblies in the block copolymer-BS system studied in **Paper II**, it was very challenging to achieve a decent 3D structure of the object even though an isosurface 3D reconstruction was obtained (see Movie S3 in Supporting information (SI) of **Paper II**). Nevertheless, cross-sectional information was relatively easy to retrieve from the 3D reconstruction, and consequently with the combination of the top view and cross section of the images, it was possible to acquire the overall structural (including internal) and morphological information of the objects. Accordingly, the 3D structures could also be visualized by 3D models sketched by hand (Figure 2.7) in addition to the reconstructed 3D structures (Movies S1–S6 in SI of **Paper II**).

2.2.3 Optical microscopy

Both cryo-TEM and cryo-ET have a powerful and versatile ability to detect the morphological and structural information of the investigated objects at very high resolution with a small length scale (several nanometers). However, it is more difficult to observe the dynamics (motions) of the objects in the solution state with electron microscopy techniques. Optical microscopy is a more suitable and easily accessible technique for this kind of task. OM is also the oldest microscope design and the most traditional technique for observing small colloidal objects.

In the OM technique, visible light is used as the radiation source, generally, one or a series of lenses are employed to magnify the small objects. The lenses are placed between the sample and the viewer's eyes to magnify the image so that it can be examined in greater detail. With the help of charge-couple device (CCD) cameras, the magnified images can be projected onto a computer screen in real time, making it more convenient to observe the sample with the digital microscopes.[124]

As described in **Paper V**, OM was used to investigate the coacervation phenomenon in gemini surfactant-BS systems, i.e., small coacervate droplets with a size around 1 μm. In addition, from OM experiments, liquid-liquid phase separation or liquid-solid phase separation can be easily distinguished. OM was therefore a very suitable technique for the study presented in **Paper V**.

2.3 Calorimetry techniques

2.3.1 High-sensitivity differential scanning calorimetry

DSC is a very robust thermodynamic technique for investigating the phase and conformational transitions in polymer-surfactant systems. The thermal parameters such as the enthalpy (either exothermic or endothermic) and the temperature (onset or maximum) of a phase transition can be determined directly from the DSC measurements. These parameters are indispensable for studying the interaction and thermoresponsive behavior in polymer-surfactant systems, in our case, the thermoresponsive block copolymer-BS systems.

The calorimeter requires a high sensitivity in order to follow small energy changes associated with the thermally induced phase transitions at low solute solution concentrations. This high sensitivity is accomplished through the use of differential power compensation between a reference and a sample cell, and a carefully designed method to control temperature and scan rate during the thermal experiment.[125] In a DSC experiment (Figure 2.8a), a sample and a reference (the solvent, here water) with the same volume are filled into the sample and reference cells, respectively. When increasing or decreasing the temperature at a certain scan rate, the temperature sensor located between these two cells determines whether there is a temperature difference between the cells and if so, applies a compensating power through heaters to keep the cells at more or less the same temperature.

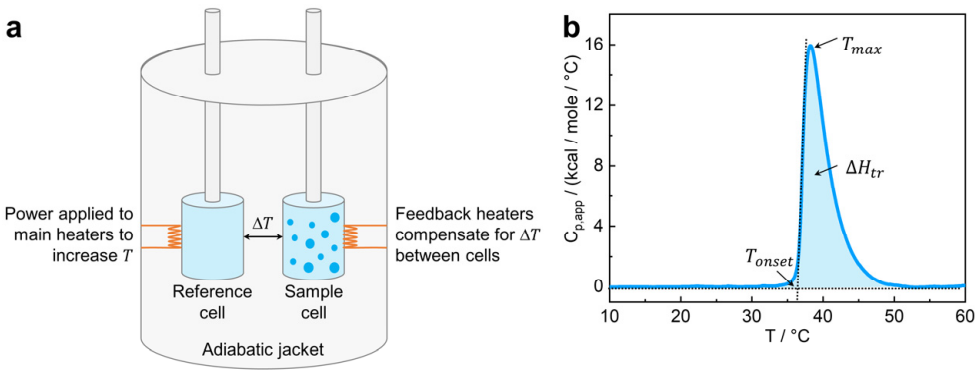

Figure 2.8 (a) Schematic representation of a typical DSC instrument. In scans where the temperature (T) is increased, power is applied to the main heaters, which causes the temperature of the cells to increase at a constant rate. The temperature difference (ΔT) between the sample and reference cells is measured by the instrument and compensated for by the feedback heaters. (b) Data output from a DSC measurement showing the normalized apparent molar heat capacity $C_{p,app}$ as a function of T. Here, T_{onset} and T_{max} are the transition temperatures as indicated and the transition enthalpy (ΔH_{tr}) is obtained from the area of the transition peak.

The power compensation signal is recorded as the output data and is reported as the heat capacity C_p against the temperature (T), generating thermal transition peaks in DSC curves. With concentration, cell volume, and scan rate, the C_p is normalized and expressed as the apparent molar heat capacity $C_{p,app}$ (kcal/mole/°C). The transition enthalpy ΔH_{tr} can be obtained by the integration of the peak area in the DSC curve (Figure 2.8b) as:[126]

$$\Delta H_{tr} = \int_{T_{onset}}^{T_{end}} C_{p,app}\, dT \tag{2.22}$$

where T_{onset} and T_{end} are the temperatures at which the transition (peaks) begins and ends, respectively. T_{onset} is defined as the intersection point of two lines as shown in Figure 2.8b. The temperature corresponding to the peak maximum is denoted T_{max}. In DSC curves, a sharper or narrower transition peak gives the signal of the higher cooperativity in the intermolecular interactions during the phase transition event.

With the thermal parameters, T_{onset} , T_{max} and ΔH_{tr} obtained from DSC measurements, the intermolecular interactions and the temperature-induced phase transitions in block copolymer-NaDC and block copolymer-SDS systems were studied at different temperatures up to 60 °C as described in **Papers III** and **IV**, respectively.

2.3.2 Isothermal titration calorimetry

As described above, the DSC technique detects the enthalpy change of the phase transition process induced by the temperature changes in thermoresponsive systems. Similar to the DSC technique, the ITC technique also detects the observed enthalpy changes but, in this case, induced by changes in concentration at constant temperatures. ITC is a powerful and widely used technique to study molecular interaction in self-assembly or association processes in colloidal mixtures. By simply measuring the heat absorbed (endothermic) or released (exothermic) during interactions in liquid solutions, the complete and accurate thermodynamic parameters can be directly determined, such as the observed enthalpy change ΔH_{obs}, the binding constant K_a, the reaction stoichiometry n, the free energy change ΔG, and the entropy change ΔS.[127]

A typically isothermal titration calorimeter (power compensation) is composed of two identical cells (reference and sample) which are located within an adiabatic jacket[128] (Figure 2.9a). The reference cell usually contains the solvent while the sample cell contains the solution which will be titrated by another solution. Constant power is applied to the reference cell to maintain a set temperature. Titration (injection) of a high concentration solution through a stirring syringe into the sample cell results in an

exothermic or endothermic interaction in the mixed solution in the sample cell, which causes a temperature difference (ΔT) between the two cells. The ΔT is measured by a circuit which then provides the feedback power to maintain the isothermal condition either by increasing or decreasing the sample cell temperature to reach that of the reference sample. The raw signal from ITC measurements is the power (P, μcal/s) (Figure 2.9b) and the power consumed at each injection is then integrated with time (t) to give ΔH_{obs} of the interaction process in the sample cell (Figure 2.9c) using Equation (2.23):[129]

$$\Delta H_{obs} = \int P\, dt \tag{2.23}$$

In colloidal systems like the polymer-surfactant and gemini surfactant-BS systems studied in **Papers II**, **IV** and **V**, the ITC method is used to determine the CMC, the critical aggregation concentration (CAC), the charged neutral concentration, and the saturation concentration (C_s). Through these parameters, the surfactant micellization, surfactant binding or association to polymer chains, thermodynamic interaction during mixed complex formation, and composition-controlled nanostructural changes of mixed complexes can be deeply understood, especially with the combination of other techniques such as cryo-TEM, DLS and SAXS.

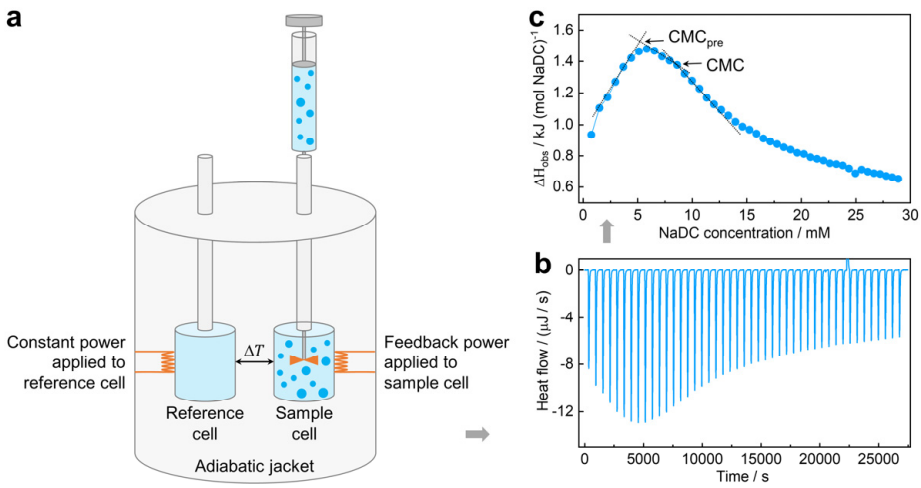

Figure 2.9 (a) Schematic representation of the power compensation in an ITC instrument. Constant power is applied to the reference cell, activating a feedback circuit, which applies a variable power to the sample cell. This maintains a very small and monitored temperature difference (ΔT) between the cells. The feedback power is the baseline in the ITC experiment. Exothermic reactions generate heat, thus triggering a decrease in the feedback power, whereas endothermic reactions increase the feedback power. (b) Raw heat flow as a function of time from an ITC experiment for titrating concentrated NaDC solution into water. (c) Observed enthalpy changes (ΔH_{obs}) as a function of NaDC concentration from the integration of the peaks in the heat flow curve (b), CMC and CMC_{pre} of NaDC are determined at the intersection points of the two lines.

2.4 Electrophoretic mobility

In aqueous mixtures of oppositely charged amphiphiles, most of the colloidal assemblies carry surface charges. Knowledge of the charge information is very helpful when further investigating the chemical composition, interaction, and aggregate structure of colloidal systems. It is therefore important to estimate the surface charges of colloidal particles, and for this electrophoretic mobility measurement is a widely used and powerful method.

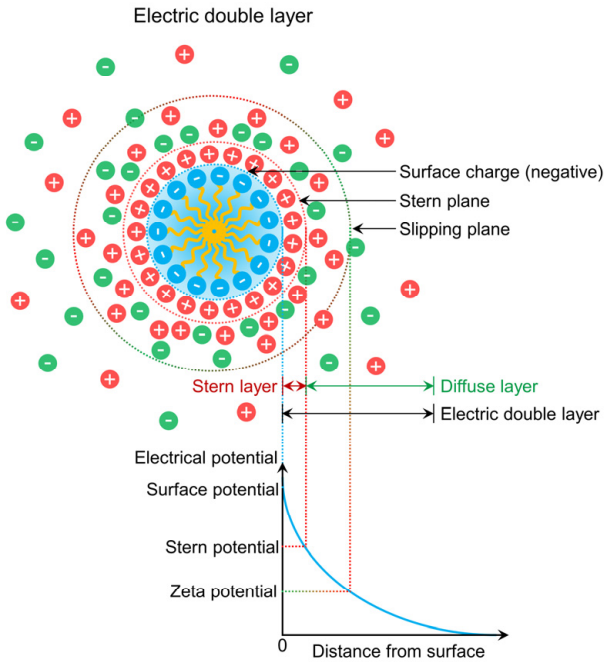

Figure 2.10 Schematic illustration of the distribution of counterions, which defines the electric double layer, around a negatively charged colloidal particle (here surfactant micelle) in an aqueous medium.

A colloidal particle with a net charge at its surface affects the distribution of counterions in its surrounding interfacial region, thereby resulting in an electric double layer (EDL) around each particle. The EDL consists of two layers (Figure 2.10), an inner one (Stern layer) where the counterions are strongly bound onto the particle surface, and an outer one (diffuse layer) where the ions are less firmly associated. Within the diffuse layer, there is a boundary called the slipping plane, inside of which, the particle and its counterions form a stable entity. When a particle moves due to gravity, thermal motion, or enteral forces (for example when an electrical field is applied), the ions within the slipping plane also move along with the particle, whereas those beyond the boundary

stay with the bulk dispersant. The potential at the slipping plane is known as the zeta potential ζ, and the magnitude of ζ gives an indication of the stability of a colloidal system. If a solution containing colloidal particles has a large negative or positive ζ value, the particles can be stabilized by the repulsive electrostatic force.

Usually, the surface charge property of the colloidal particles can be expressed as electrophoretic mobility (μ). The μ is the experimentally measured value from which the ζ can be estimated through the Henry equation:[130,131]

$$\mu = \frac{2\varepsilon_r \varepsilon_0 \zeta f(\kappa a)}{3\eta} \tag{2.24}$$

where ε_r is the dielectric constant of the medium, ε_0 is the permittivity of the vacuum, and η denotes the viscosity at the experimental temperature. Moreover, $f(\kappa a)$ is the Henry function, κ is the Debye length (κ^{-1} is often taken as a measure of the "thickness" of the EDL) and a is the radius of the particle.

For large spherical particles, i.e., when the radius of the particles is much larger than the Debye length ($\kappa a > 100$) and the diffuse layer, the value of $f(\kappa a)$ is taken as 1.5 in the Henry function. For small particles, on the other hand, the radius is much smaller than the thickness of EDL ($\kappa a \ll 1$), and the value of $f(\kappa a)$ is taken as 1 in Equation (2.24).[132]

The electrophoretic mobility can be measured by using the laser Doppler electrophoresis technique. In such an experiment, a laser light illuminates colloidal particles in solution with an applied electric field (E), the charged particles then move towards the oppositely charged electrode with a velocity (v), during which the Doppler frequency shift of scattered light caused by the moving particles is monitored and measured as the electrophoretic mobility. The μ ($m^2\ s^{-1}\ V^{-1}$) is defined as the velocity of the particle per unit applied electric field in the equation:

$$\mu = \frac{v}{E} \tag{2.25}$$

In this thesis, a Malvern Zetasizer Nano-ZS instrument equipped with a 632.8 nm 4 mW He-Ne laser was utilized to determine the electrophoretic mobility of the different self-assembled aggregates. Measurements were performed at a fixed scattering angle of 13° at certain temperatures by combining the laser Doppler electrophoresis technique and a phase analysis light scattering method.[132]

2.5 Circular dichroism

CD is an excellent method for studying chiral species in solution. It is widely used to determine the secondary structure of proteins and also to investigate chiral properties of self-assembled aggregates either from chiral molecules or in an asymmetric arrangement.

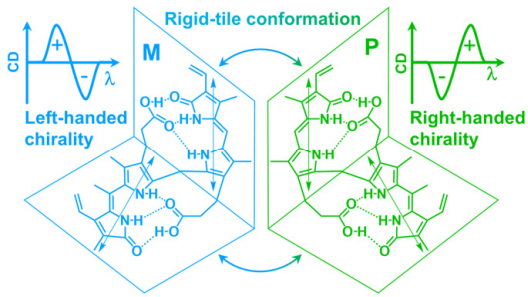

Figure 2.11 Schematic illustration of the interaction of chiral species with M- and P-forms of bilirubin-IXα, generating a left-handed and right-handed CD signal, respectively.

Plane polarized light consists of two circularly polarized components of equal magnitude: a left-handed (L) and a right-handed (R) component. CD refers to the sample's differential absorption of these two components.[133–135] If the sample only contains achiral species in solution, the L and R components will not be absorbed or will be absorbed to equal extents. The combination of the two components would then regenerate light polarized in the original plane, i.e., no CD signal will show up in the spectrum. However, for a sample that contains chiral species, the L and R components will be absorbed to different extents, and the resultant light will then be elliptically polarized, thereby generating the CD signal. The CD signal can be expressed as either the difference in absorbance (A) of the two components ($\Delta A = A_L - A_R$) or as the ellipticity in degrees as the function of the wavelength.[133]

In this thesis, the CD method was used to study the molecular and supramolecular chirality in polymer-BS systems in **Paper II** and the different chiral properties in gemini surfactant-BS systems in **Paper V**. To test the chiral selectivity of the mixed aggregates formed in these studied systems, bilirubin-IXα (BR) was used as a probe. In addition, the drug-loading ability of the mixed complexes was also assayed as BR can be used as a drug. BR has two interconverting enantiomeric "ridge tile" conformations (M- and P-forms) that are stabilized by six intramolecular hydrogen bonds (Figure 2.11). Chiral molecules (or their aggregates) can selectively interact with one of the conformations and by that determine an enantiomer in excess as revealed by a typical CD signal. When

chiral species interact with the M-form of BR, the CD spectrum will have a positive band at a shorter wavelength and a negative band at a longer wavelength, which corresponds to a left-handed CD signal (Figure 2.11). An inverted CD spectrum on the other hand can be observed when the P-form of BR is selected to interact with chiral species,[136–138] which then generates a right-handed chirality (Figure 2.11).

3 Oppositely charged block copolymer-bile salt mixtures

One motivation for studying the oppositely charged block copolymer-BS systems presented in this thesis was to explore cationic block copolymers as potential BS sequestrants which could be used in the treatment of BS-related diseases and hypercholesterolemia. For this purpose, fundamental investigations of the interaction between oppositely charged block copolymers and BS in dilute aqueous solution from a physico-chemical perspective can thus be the base for future medical applications.

Paper I describes an investigation of the phase behavior, mixed complex formation and supramolecular structures of the complexes in the mixtures of the cationic block copolymer PNIPAM$_{120}$-*b*-PAMPTMA(+)$_{30}$ and bile salt sodium deoxycholate (NaDC) at room temperature. Based on the results presented in **Paper I**, the thermoresponsive behavior of the same PNIPAM$_{120}$-*b*-PAMPTMA(+)$_{30}$-NaDC system was further researched in **Paper III**. The studies on the PNIPAM$_{120}$-*b*-PAMPTMA(+)$_{30}$-NaDC system were extended in **Paper II** by using similar block copolymers and the same BS (NaDC) to investigate the effects of copolymer block length on the supramolecular structure. The block copolymers used were PNIPAM$_m$-*b*-PAMPTMA(+)$_n$ where m = 48 or 65, n = 20. It is worth mentioning that the chirality of the mixed complexes in **Paper II** was also explored due to the chiral nature of BSs and also the supramolecular chirality of the assemblies. This kind of investigation is also an initial attempt towards applications of drug loading and drug delivery.

This chapter summarizes the results from the studies of the oppositely charged block copolymer-BS systems in **Papers I–III**. DLS, SLS and electrophoretic mobility were employed to follow the size changes and association behavior of different block copolymer-BS systems at varying compositions and temperatures. The structural and morphological information about the supramolecular assemblies was characterized by cryo-TEM, cryo-ET, and SAXS/WAXS techniques. The thermodynamic interaction during the co-assembly process was investigated by the ITC technique. The chiral properties and potential drug loading ability of the mixed complexes were explored by the CD method. In addition, the heat-induced phase transition and thermoresponsive

behavior in the PNIPAM$_{120}$-*b*-PAMPTMA(+)$_{30}$-NaDC system were also studied by the DSC technique. The additional methods used in the investigations are described in conjunction with the respective results in the papers.

3.1 Mixed complex formation

Paper I describes the investigation of dilute aqueous mixtures of the cationic diblock copolymer PNIPAM$_{120}$-*b*-PAMPTMA(+)$_{30}$ and NaDC in a wide range of charge compositions, expressed as either negative-to-positive molar charge fraction X = $n_-/(n_- + n_+)$ or negative-to-positive molar charge ratio CR = n_-/n_+. The chemical structures of NaDC and PNIPAM$_{120}$-*b*-PAMPTMA(+)$_{30}$ can be found in Figure 1.1 and Figure 1.2, respectively. The pure copolymer solution is denoted X = 0, and X = 0.5 corresponds to the theoretical charge-neutral composition (CR = 1). Thereby, the copolymer was in excess in the mixtures when X < 0.5 and conversely BS was in excess when X > 0.5. The investigation was conducted at ambient temperature, well below the phase transition of PNIPAM to study the formation of mixed complexes and the structures of the complexes, in order to avoid the heat-induced strong association effects of the PNIPAM block of the copolymer.

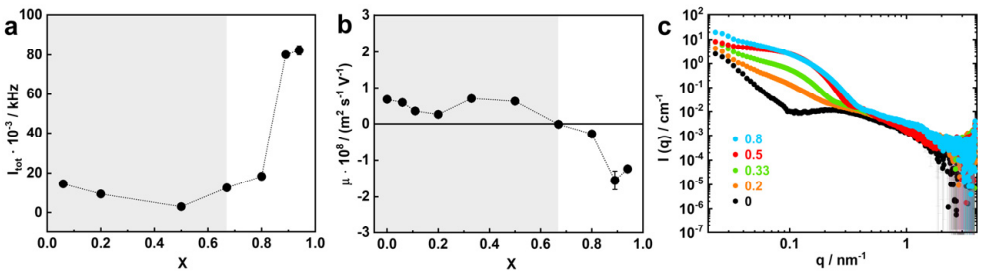

Figure 3.1 (a) Total SLS intensity (I_{tot}), (b) electrophoretic mobility (μ), and (c) SAXS curves ($I(q)$ vs. q) of PNIPAM$_{120}$-*b*-PAMPTMA(+)$_{30}$-NaDC mixtures at different negative charge fractions X: 0 ≤ X ≤ 0.94, where X = 0 denotes the pure copolymer solution. The color code in (c): X = 0 (black), X = 0.2 (orange), X = 0.33 (green), X = 0.5 (red) and X = 0.8 (blue). The temperature was 22 °C and the copolymer concentration was 0.13 wt% in (a) and (b), while 25 °C and 0.5 wt% copolymer concentration were used in (c).

Figure 3.1a, b presents the total scattering intensity (I_{tot}) and the electrophoretic mobility of the mixtures at different compositions (0 ≤ X ≤ 0.94). When X ≤ 0.67, the I_{tot} was almost constant, and the μ was close to zero and slightly positive, which suggests that the BS preferentially interacted electrostatically with the cationic PAMPTMA(+) blocks to form mixed complexes of neutral or slightly positive charges in the PNIPAM$_{120}$-*b*-PAMPTMA(+)$_{30}$-NaDC mixtures at relatively low X. However, the I_{tot} starts to increase sharply, accompanied by a decreasing μ to negative values,

when X is increased above 0.67, indicating that larger complexes of negative charge were formed at high X (X > 0.67). This could be attributed to the fact that the exceeding NaDC molecules could associate with the mixed complexes through hydrophobic interactions.

SAXS results shown in Figure 3.1c also indicate the formation and growth of the mixed complexes with increasing X. In a 0.5 wt% copolymer solution, the copolymer existed as free polymer chains and some large multichain clusters could contribute to the upturn scattering intensity at low q in the SAXS curve. Addition of BS to the copolymer solution changed the shape of the SAXS curves, especially in the low q range, suggesting an interaction beween the copolymer and BS molecules, and formation of mixed complexes. The SAXS curve demosntrates a typical Guinier behavior at low q when X reaches 0.5, which was expected for the globular-like structure of the mixed complexes. The structures of the mixed complexes in the copolymer-BS mixtures are discussed in detail in the following subchapter.

3.2 Co-assembled supramolecular structures

3.2.1 Intriguing supramolecular structures

To obtain the structural and morphological information about the mixed complexes formed in the PNIPAM$_{120}$-*b*-PAMPTMA(+)$_{30}$-NaDC system, cryo-TEM and SAXS experiments were conducted on the mixture at X = 0.5 and the results are summarized in Figure 3.2. Cryo-TEM images illustrate that two morphologically different mixed complexes are formed and coexist at ambient temperatures.

The first type of complex (see Figure 3.2b) has a globular morphology with a coacervate core (D_{core} = 21 ± 3 nm) of deoxycholate anions (DC^-) and PAMPTMA(+) blocks surrounded by a PNIPAM corona. Assuming no hydration of the core, the aggregation numbers of copolymers and DC^- molecules in this complex were estimated in a crude calculation to be about 174 and 5220, respectively. In addition, Figure 3.2c suggests that the globular complexes dominate the SAXS curve and by that possibly overshadow the contribution of the tape-like complexes. The curve is well-described by a form factor of a spherical particle with a graded out interface composed of the polymers in a Gaussian chain conformation. A good fit was achieved for particles with a core diameter of about 18 nm, which was in good agreement with the size inferred from cryo-TEM (Figure 3.2b).

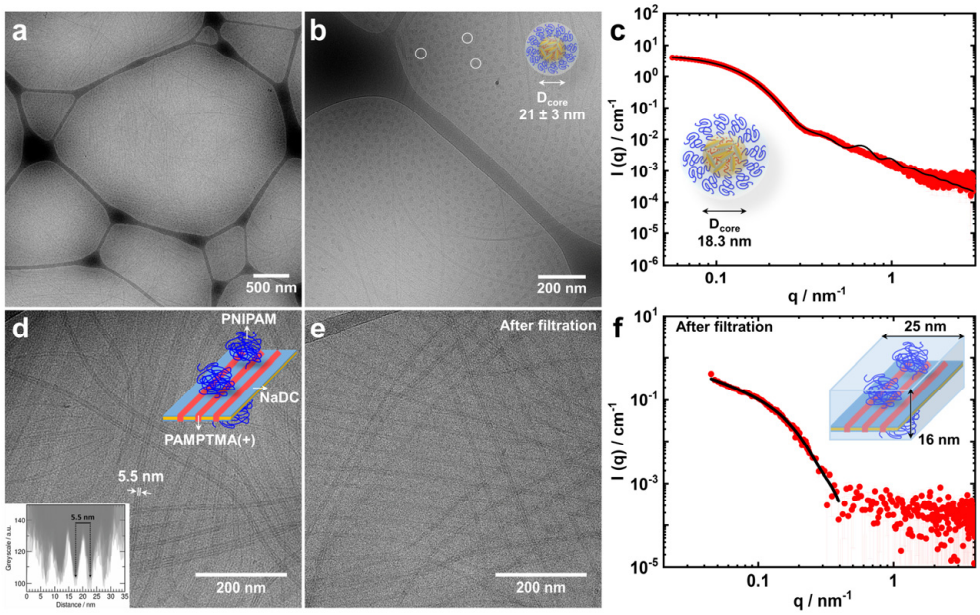

Figure 3.2 (a, b, d, e) Cryo-TEM images and (c, f) SAXS curves of the $PNIPAM_{120}$-*b*-$PAMPTMA(+)_{30}$-NaDC mixtures at X = 0.5. (a) Overview image showing the coexistence of globular structures and striped tape-like structures. (b) Cryo-TEM image focusing on the globular structures with an estimated core diameter (D_{core}) of 21 ± 3 nm. (c) Experimental SAXS curve (red symbols) and best-fitting curve (black line) for particles with a spherical core (D_{core} = 18.3 nm) and a graded interface of Gaussian chains. (d, e) Cryo-TEM images show the striped tape-like structures with an inter-stripe distance estimated to be 5.5 nm by the gray scale analysis in the inset of (d). (f) Experimental SAXS curve of the same sample as in (e) (red symbols) and the fitting curve (black line) based on a form factor of an infinitely long parallelepiped with a rectangular cross section with a width of 25 nm and a height of 16 nm. The mixed solution for (e, f) was filtered through a syringe filter with pores of 0.45 μm. The color code for the models of globular structures (b, c) and striped tape-like structures (d, f): PAMPTMA (+) blocks (red), PNIPAM blocks (blue), and NaDC (light blue + orange). The copolymer concentrations were 0.25wt% in (a, b, d), 0.5wt% in (c), and 0.1wt% (e, f) and all measurements were done at 25 °C.

Figure 3.2d emphasizes the second type of complexes that are unusually ordered striped tape-like supramolecular structures with a length of several micrometers. The inter-stripe distance was estimated to be 5.5 nm by the gray scale analysis (see inset of Figure 3.2d). We proposed a model for such supermolecular structures (Figure 5 in **Paper I**) based on the fact that the stripes consisted of the self-assembled, oppositely oriented DC^- molecules that partly overlapped as a result of the hydrophobic interaction between them. This way, the BS molecules were associated and joined by the PAMPTMA(+) side chains of the copolymer blocks. The whole tape was built up by many block copolymers and was covered on both sides by the PNIPAM blocks, probably in a slightly coiled conformation, which can prevent the tapes from aggregating under ambient temperature conditions.

To separate these two coexisting complexes, filtration was performed. However, the cryo-TEM image in Figure 3.2e implies that the striped tape-like complexes were

reformed, meaning that a reorganization of the material in solution after filtration probably led to a more uniform solution. This result was also evidenced by the SAXS curve which was fitted to a form factor of an infinitely long parallelepiped with a rectangular cross section that is 25 nm wide and 16 nm high (Figure 3.2f and the inserted model). The fitting result was in accordance with the cryo-TEM result on the same sample (Figure 3.2e).

3.2.2 Truth behind the striped tape-like structure

The striped tape-like complexes found in the PNIPAM$_{120}$-*b*-PAMPTMA(+)$_{30}$-NaDC system were so fascinating that a subsequent study was performed to gain a deeper understanding of the truth behind this interesting co-assembly behavior. It was anticipated that the PAMPTMA(+) block of the copolymer played a critical role in the formation of the supramolecular structures. Therefore, the first system to be investigated was the mixtures of the cationic homopolymer PAMPTMA(+)$_{130}$ and NaDC in **Paper II**. Cryo-TEM performed on the PAMPMTA(+)$_{130}$-NaDC mixture at CR = 0.5 revealed single micrometer-long "nanowires" (Figure 3.3a), which confirmed the importance of the PAMPTMA(+) block in the formation of these supramolecular structures. This was also indirectly proved in the cryo-TEM images of the PNIPAM$_{71}$ homopolymer-NaDC mixture where no visible complexes were observed (Figure S22 in **Paper II**).

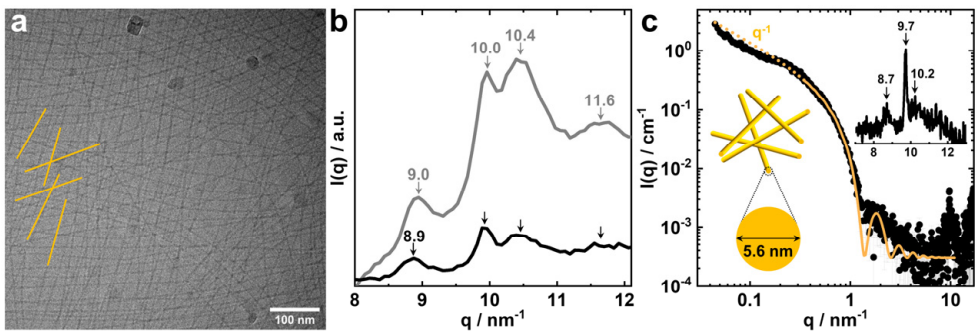

Figure 3.3 (a) Cryo-TEM image at CR = 0.5 and (b) WAXS curves of the concentrated phase at CR = 0.5 (black) and the precipitate at CR = 1 (gray) of PAMPTMA(+)$_{130}$-NaDC mixtures. The q values of the WAXS peaks are indicated in (b). (c) Experimental SAXS curve (black symbols) of the same sample as in (a) and the best-fitting curve (orange line) for a model of rod-like particles with a cross-sectional diameter of 5.6 nm (inset: WAXS region with the peaks indicated). The homopolymer concentration was 0.5 wt% and the temperature was 25 °C.

It is well established that NaDC forms gels at pH around 7, from which dry fibers can be drawn. It has been demonstrated that the dry fibers are composed of NaDC molecules in a helical arrangement as reflected in a very typical X-ray pattern.[139–141]

With this in mind, WAXS experiments were performed on the PAMPTMA(+)$_{130}$-NaDC mixture at CR = 0.5 (concentrated by centrifugation) and at CR = 1 (precipitate). The revealed peaks (Figure 3.3b, c (inset)) matched the layer lines of the X-ray pattern for the NaDC dry fiber ascribed to the typical supramolecular helical structure of NaDC.[140,141] More details can be found in **Paper II**. From this, it can be concluded that the PAMPTMA(+)$_{130}$-NaDC nanowires were composed of helices of DC^- with PAMPMTA(+)$_{130}$ polyions associated through electrostatic interactions. In addition, the PAMPTMA(+)$_{130}$-NaDC helices at CR = 0.5 could be fitted to rod-like particles with a cross-sectional diameter estimated to be 5.6 nm (Figure 3.3c).

Finally, it is clear that the dark stripes observed in the tape-like structure formed in PNIPAM$_{120}$-*b*-PAMPTMA(+)$_{30}$-NaDC system (described in **Paper I**) and the single nanowires formed in PAMPTMA(+)$_{130}$-NaDC system (described in **Paper II**) were in fact the self-assembled NaDC molecules in a helical arrangement, having formed with the help of either PNIPAM$_{120}$-*b*-PAMPTMA(+)$_{30}$ or PAMPTMA(+)$_{130}$. The words "stripes" and "nanowires" thus had an equivalent meaning and the word "helices" is therefore preferred and used from now on.

3.2.3 Assembly of supramolecular helices into bundles

To examine if the formation of the striped supramolecular co-assembled structures found in the PNIPAM$_{120}$-*b*-PAMPTMA(+)$_{30}$-NaDC system is a general phenomenon that also exists in similar copolymer-BS systems, two block copolymers with the same chemical composition but with different block lengths were introduced in the investigation reported in **Paper II**. They were denoted PNIPAM$_m$-*b*-PAMPTMA(+)$_{20}$ where m = 48 or 65. The objective was also to study the effect of block length on the co-assembly in the block copolymer-NaDC systems.

Figures 3.4a–c and S5 in **Paper II** reveal that helices packed orderly into bundles can also appear in the shorter copolymer-NaDC systems, thus demonstrating the above-mentioned common phenomenon and again showing the importance of the cationic block of the copolymers in the formation of these bundles. The bundles of helices packed with a regular spacing were present at all CRs (Figure 3.4a–c and S5 in **Paper II**), and they co-existed with single helices in PNIPAM$_{65\text{ or }48}$-*b*-PAMPTMA(+)$_{20}$-NaDC mixtures when CR ≤ 0.5 (Figures S5a and S9 in **Paper II**). Irrespectively of the PNIPAM block length of the investigated PNIPAM$_m$-*b*-PAMPTMA(+)$_{20}$ copolymers, the width of the bundles became wider with increasing CR, thus being tunable through optimization of the mixing ratio (Figures 3.4a–c, S5 and Table S1 in **Paper II**).

To further understand how the supramolecular helices pack in three dimensions, the cryo-ET technique was utilized. A Cryo-ET 3D reconstruction (Figure 3.4d) and analysis of the cross sections (Figure 3.4e, f) of the bundle formed in PNIPAM$_{65}$-*b*-PAMPTMA(+)$_{20}$-NaDC mixture at CR = 1 (Figure S13 in **Paper II**) revealed that the supramolecular helices were packed in a hexagonal lattice. An inter-helix distance of 5.5 nm and an inter-plane distance of 4.8 nm was estimated from the gray scale analysis (Figures 3.4f and S14c in **Paper II**). The distances were in good agreement with the periodic spacing in the bundles generally measured from the cryo-TEM 2D images (Figures S6–S8 and S10–S12 in **Paper II**) and also consistent with those of the hexagonal liquid crystalline phase at a high NaDC concentration.[142]

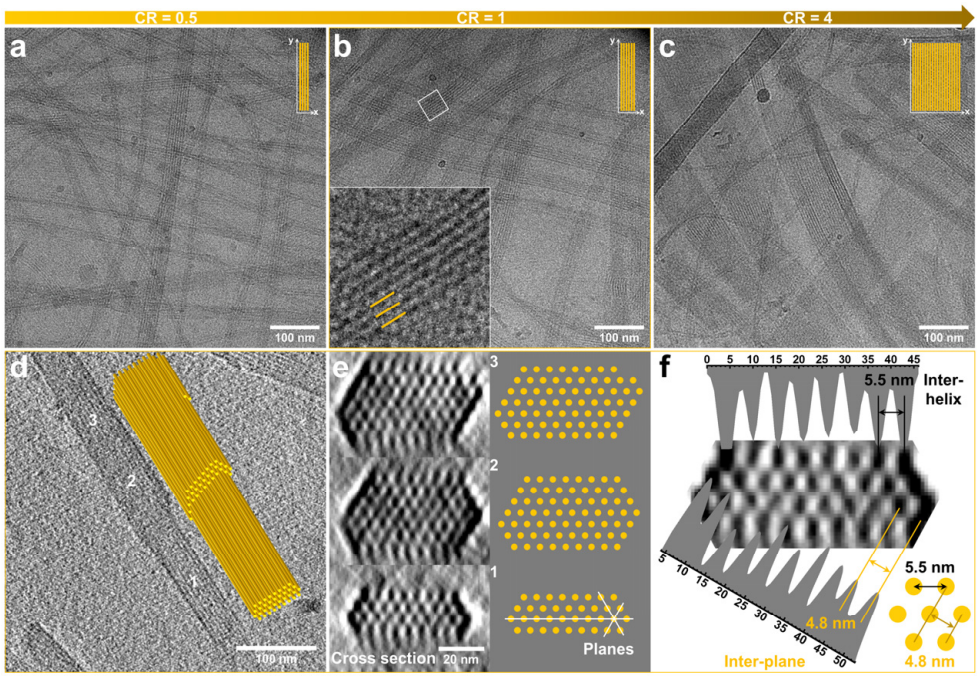

Figure 3.4 Cryo-TEM images of PNIPAM$_{65}$-*b*-PAMPTMA(+)$_{20}$-NaDC mixtures at CR of (a) 0.5, (b) 1 (inset: enlargement displaying the bundle interior in the marked region), and (c) 4. (d) Top view of cryo-ET reconstruction and corresponding 3D sketched model of the bundle in the PNIPAM$_{65}$-*b*-PAMPTMA(+)$_{20}$-NaDC mixed complexes at CR = 1. (e) Cross sections and corresponding sketches reconstructed in different positions of (d) marked with 1, 2, and 3. (f) Gray scale analysis of the cross section and sketch of the hexagonal lattice with inter-helix (5.5 nm) and inter-plane (4.8 nm) distances.

Moreover, the second type of cationic diblock copolymer and its interaction with NaDC was also investigated in **Paper II**. It has a hydrophilic non-ionic block of MPEG and the same cationic block PAMPTMA(+), denoted MPEG$_{45}$-*b*-PAMPTMA(+)$_{21}$ (see the chemical structure in Figure 1.2). Cryo-TEM experiments performed on MPEG$_{45}$-*b*-PAMPTMA(+)$_{21}$-NaDC mixtures at CR = 0.5 (Figure S15 in **Paper II**) and CR = 1

(Figure 3.5a, d) displayed the same type of bundles as observed for the PNIPAM$_m$-*b*-PAMPTMA(+)$_{20}$-NaDC systems. Single helices co-existed with such bundles at CR = 0.5 (Figure S15 in **Paper II**). The periodic distance measured in the bundles was similar to that obtained for the PNIPAM$_m$-*b*-PAMPTMA(+)$_{20}$-NaDC systems (Figure S16d, e in **Paper II**).

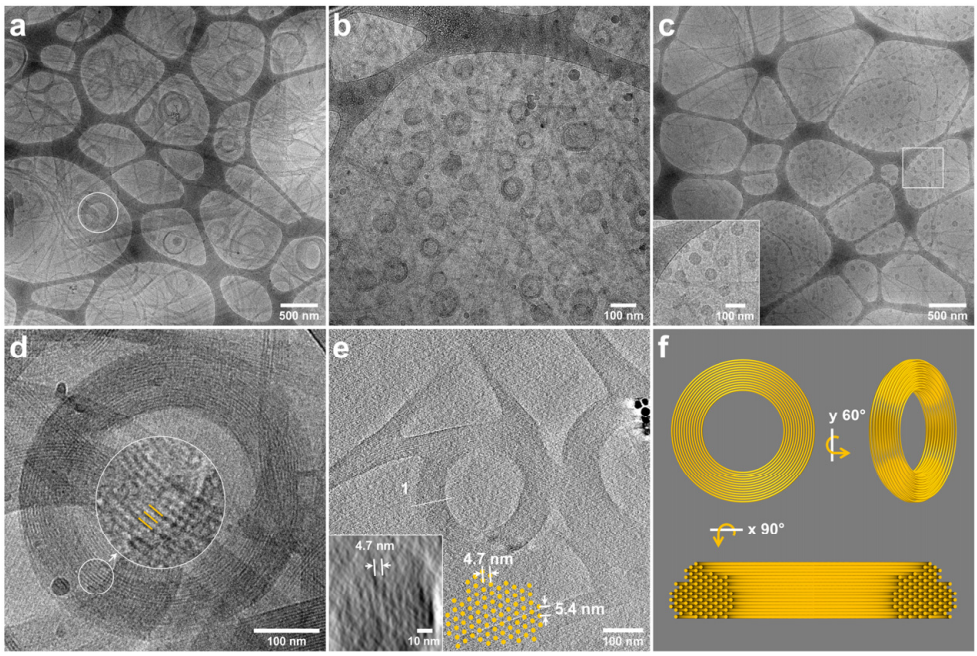

Figure 3.5 Cryo-TEM overview showing the toroidal structures of (a) MPEG$_{45}$-*b*-PAMPTMA(+)$_{21}$-NaDC mixture at CR = 1, (b) PNIPAM$_{65}$-*b*-PAMPTMA(+)$_{20}$-NaDC mixture at CR = 0.5, and (c) PNIPAM$_{48}$-*b*-PAMPTMA(+)$_{20}$-NaDC mixture at CR = 1, with a zoomed-in area of (c) in the inset. (d) Zoom of the toroid marked in (a) together with a further zoomed-in area highlighting the internal structure. (e) Cryo-ET reconstruction of a toroid of the MPEG$_{45}$-*b*-PAMPTMA(+)$_{21}$-NaDC mixture at CR = 1 with the reconstructed cross section and inter-plane distance reported in the inset and reproduced in the sketch. (f) 3D model sketches of the toroid in (e) displaying different orientations and a cross section with hexagonal lattice achieved by a 90° rotation of the model.

3.2.4 Toroids of supramolecular helices

Co-assembled toroidal structures were also found to co-exist with the bundles in all the investigated block copolymer-NaDC systems at certain compositions. The toroid sizes, in terms of average outer diameter D and thickness T of the toroidal wall, are summarized in Table S1 in **Paper II**. In the case of the PNIPAM$_m$-*b*-PAMPTMA(+)$_{20}$-NaDC systems, the toroids of the copolymer with the longer PNIPAM block (m = 65) had a slightly larger diameter (D = 81 ± 15 nm) than those composed of the copolymer with the shorter PNIPAM block (m = 48) (D = 55 ± 10 nm), while the thickness was roughly the same in both cases (15–17 nm). The toroids of the MPEG$_{45}$-*b*-

PAMPTMA(+)$_{21}$-NaDC system were in general much larger (D = 395 ± 81 nm and T = 75 ± 25 nm) than those of the PNIPAM$_m$-*b*-PAMPTMA(+)$_{20}$-NaDC systems, and displayed a better resolved internal structure (Figure 3.5d). It was demonstrated by cryo-ET that the toroids were built up by concentrically and hexagonally packed helices with an inter-plane distance of 4.7 nm and a calculated inter-helix distance of 5.4 nm (Figure 3.5e, inset). This was in good correlation with the distances obtained for the bundles of the same sample (Figure S17f in **Paper II**) and the results regarding the PNIPAM$_m$-*b*-PAMPTMA(+)$_{20}$-NaDC systems (Figure 3.4).

Strikingly, the bundles and toroids of the block copolymer-NaDC mixtures were structurally very similar to those formed by hexagonally close-packed DNA helices under specific conditions[143,144] (Figure 2g–i in **Paper II**). Condensation of DNA helices into hexagonally packed bundles and toroids represents an intriguing example of the functional organization of biological macromolecules at the nanoscale.[143–150] It occurs under many different conditions and is fundamental for the biological functions of DNA. Condensation models are based on the unique polyelectrolyte features of DNA.[149–153] However, the bundles and toroids of helices discussed in **Paper II** signify that it is possible to reproduce a DNA-like condensation with supramolecular helices of small chiral molecules.

3.2.5 Formation mechanism

Figure 3.6 shows the illustration of the formation of supramolecular helices and their association (condensation) into the hexagonal arrangement in the form of bundles and toroids. In the study presented in **Paper II**, the NaDC self-assembly was induced by intermolecular interaction with oppositely charged homopolymer or block copolymers. Single supramolecular helices were mainly formed at low negative charge fractions, and they were clearly isolated when the cationic homopolymer was used. With block copolymers, the condensation of the helices into bundles and toroids was induced by increasing the NaDC fraction in the mixture. The microscopy and X-ray techniques demonstrated that the hexagonal lattice of the helices was the same irrespective of the length and the chemical composition of the nonionic block of the copolymer (i.e., either PNIPAM or MPEG). This suggests that the core of the bundles and toroids mostly comprised helices of DC^- anions, while the charged blocks of the copolymers acted as large counterions at the surface and/or in a thin outermost shell of the core. The nonionic blocks protruded out from the core into the surrounding solution (Figure 3.6). This proposed model was verified by a liquid ^{1}H NMR measurement on the PNIPAM$_{48}$-*b*-PAMPTMA(+)$_{20}$-NaDC mixture at CR = 1 (Figure S20c in **Paper II**). The results showed that the proton signals connected to the PAMPTMA(+) block,

which was bound to the complex surface, were very broad and that the signals almost vanished for the NaDC molecules that were tightly packed into helices. Conversely, the data indicated that the PNIPAM block mainly moved freely.

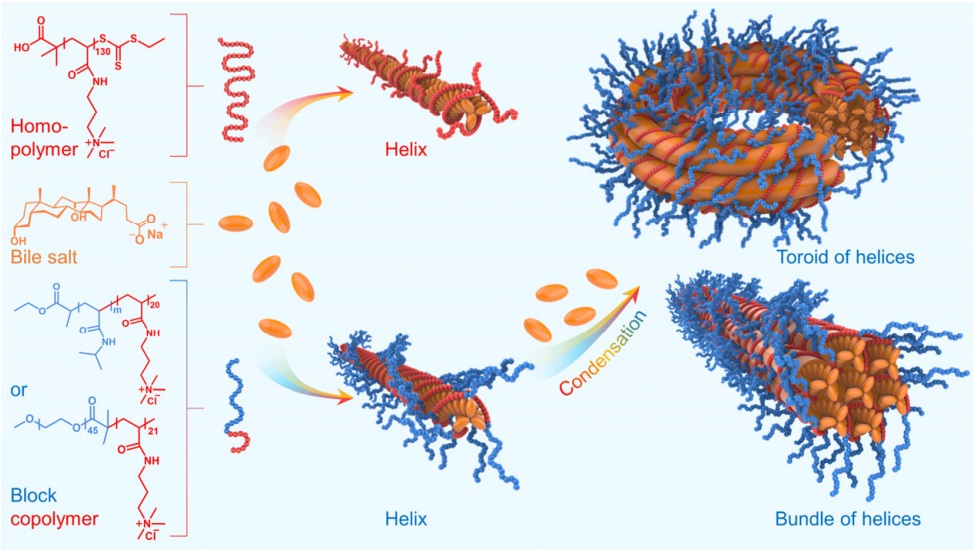

Figure 3.6 Illustration of supramolecular helix formation and condensation. Chemical structures of PAMPTMA(+)$_{130}$ homopolymer (left panel, top), bile salt NaDC (left panel, middle), and PNIPAM$_m$-*b*-PAMPTMA(+)$_{20}$ (m = 65 or 48) and MPEG$_{45}$-*b*-PAMPTMA(+)$_{21}$ block copolymers (left panel, bottom). NaDC helix formation induced by interaction with homopolymer (center panel, top) or block copolymers (center panel, bottom). Condensation of block copolymer-NaDC helices into toroid (right panel, top) and bundle (right panel, bottom). Color code: red (PAMPTMA(+)), blue (PNIPAM or MPEG), orange (NaDC).

3.3 Thermodynamic interactions

ITC experiments were carried out to gain relevant insights on the thermodynamic interaction behind the formation of copolymer-BS mixed complexes. Figure 3.7a shows the dilution curve of the NaDC micellar solution, from which two CMC values CMC$_{pre}$ (5.3 mM) and CMC (8.4 mM) were obtained (inset of Figure 3 in **Paper II**). They are related to the formation of pre-micelles and micelles of NaDC, respectively.[4–6,154,155]

The titration of NaDC solution into a solution of a homopolymer (PNIPAM$_{71}$) demonstrated that the interaction between PNIPAM and NaDC was very poor and did not impact the CMC values of NaDC. Instead, an effective CMC (CMC*) was found with the presence of PNIPAM$_{71}$ in the solution (Figure 3.7a). By contrast, the titration curve of NaDC into the PNIPAM$_{65}$-*b*-PAMPTMA(+)$_{20}$ solution presented three

endothermic transition peaks (regions), indicating that there existed some kind of interaction during the titration process (Figure 3.7a).

Region I, which is mainly defined by the peak at lower CR values (CR 0–0.4), is associated with the formation of single helices of DC^- anions driven by the interaction and rearrangement of NaDC micelles onto the PAMPTMA(+) blocks of the copolymer. The endothermic nature of the peak suggests that this process is entropy-driven due to the release of counterions and water molecules.[156]

Further addition of NaDC led to the formation of more helices in parallel with condensation into bundles and toroids. This condensation process dominated *Region II*, defined in the range CR 0.4–0.9, and generated the second endothermic peak in the ITC curve. At the end of this region, corresponding to C_s (= 7.9 mM), the copolymer was saturated by the NaDC molecules.

In *Region III* (CR ≥ 0.9), the addition of excess NaDC micelles could not bind to the saturated copolymer chains. Due to the poor interaction of NaDC with PNIPAM blocks, the curve therefore displayed the typical broad endothermic peak mainly related to the demicellization due to the low apparent NaDC concentration in the cell. At higher NaDC concentrations, the titrated NaDC micelles did not break up and the titration curve merged with the $PNIPAM_{71}$-NaDC titration curve, thus revealing the formation of NaDC free micelles. More detailed information on the ITC experiments and the interpretations can be found in **Paper II**.

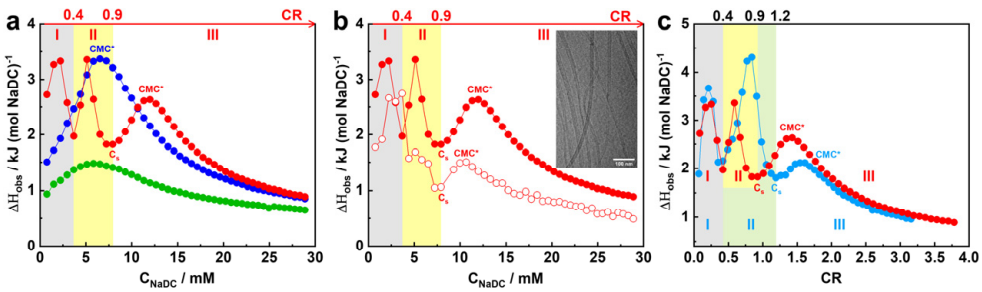

Figure 3.7 (a) ITC curves for the titration of an NaDC solution into water (green), $PNIPAM_{71}$ solution (blue) and $PNIPAM_{65}$-*b*-$PAMPTMA(+)_{20}$ solution (red). (b) ITC curves for the titration of an NaDC solution into $PNIPAM_{65}$-*b*-$PAMPTMA(+)_{20}$ solution with 50 mM NaCl (unfilled circles). The corresponding curve without salt (filled circles) from (a) is plotted for comparison. The inset shows a cryo-TEM image of $PNIPAM_{65}$-*b*-$PAMPTMA(+)_{20}$-NaDC mixure at CR = 1 with 50 mM NaCl. (c) ITC curves for the titration of an NaDC solution into solutions of shorter copolymer $PNIPAM_{48}$-*b*-$PAMPTMA(+)_{20}$ (light blue) and $PNIPAM_{65}$-*b*-$PAMPTMA(+)_{20}$ (red) plotted for comparison. The initial concentration of the NaDC solution was 200 mM, the polymer concentrations were 0.5 wt% for the ITC and 0.1 wt% for the cryo-TEM experiments.

Salt effect

The effect of salt (NaCl) on the complex formation during titration was also investigated and the outcome is presented in Figure 3.7b. As a result of the screened electrostatic interaction, the NaDC micellization occurred over a much narrower concentration range when 50 mM NaCl was present in the solution, and at the same time the two CMC values were lowered (see Figure S25 in **Paper II**).[6] By comparing the two ITC curves with or without 50 mM NaCl, it was concluded that the presence of salt caused a weakening of the co-assembly of the BS with the copolymer (i.e., the peak amplitude in *Region II* was mainly affected (Figure 3.7b). This is reflected by the thinner bundles formed in the copolymer-BS mixture at CR = 1 in the presence of 50 mM NaCl (inset of Figure 3.7b).

PNIPAM block length effect

In Figure 3.7c, it can be noticed that when comparing the NaDC titration into block copolymers with the same length of the PAMPMTA(+) block but different length of the PNIPAM block, the first endothermic peak (*Region I*), which is related to the formation of single helices, was not affected. On the other hand, the second endothermic peak in *Region II* was higher and shifted towards larger CRs for the shorter copolymer-BS system. This demonstrated that PNIPAM played a crucial role in stabilizing the bundles.

3.4 Chirality

The chiral nature of the polymer-NaDC mixed complexes and their drug loading ability were examined by using bilirubin-IXα as a probe with the help of the CD spectroscopy in **Paper II**. Details about the BR molecule can be found in **Chapter 2.5**. Chiral molecules and molecular aggregates can selectively interact with one of the BR conformations and by that determine which enantiomer is in excess as revealed by a typical CD signal (Figure 3.8a).

It can be observed in Figure 3.8b that a mixed solution of BR and NaDC at a concentration lower than the CMC (1 mM) provided a bisignate CD cotton effect, indicating a selective interaction of the NaDC monomer with the right-handed enantiomer (P-form) of BR[157] (Figure 3.8a). An inverted CD spectrum (left-handed spectrum) was observed for BR in the mixture of the $PNIPAM_{48}$-*b*-$PAMPTMA(+)_{20}$ copolymer and NaDC of the same low concentration (i.e., 1 mM) (Figure 3.8b). An equivalent selectivity was also observed for the interaction of BR with the

PAMPTMA(+)$_{130}$-NaDC single helices, with bundles and toroids of the other copolymer-NaDC systems, and in the micellar solution of NaDC at a much larger concentration than in the mixture (30 mM) (Figure 3.8b). The left-handed signal observed for block copolymer-NaDC and homopolymer-NaDC systems suggests an enantioselection of the M-form of BR by the supramolecular helices. Moreover, the CD results demonstrated a general ability of the polymer-NaDC complexes to load chiral molecules.

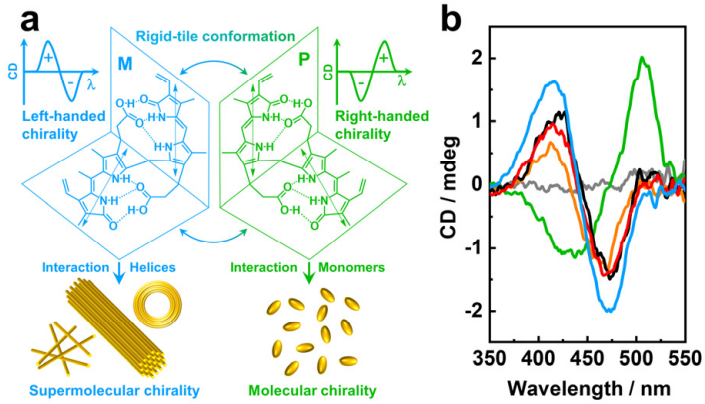

Figure 3.8 (a) Scheme showing the interaction of BR with the helices in polymer-BS mixed complexes and NaDC monomers, generating the opposite CD signal. (b) CD spectra of 1 mM (green) and 30 mM (orange) NaDC solutions, the PNIPAM$_m$-*b*-PAMPTMA(+)$_{20}$-NaDC mixtures at CR = 0.5 (m = 65, red, m = 48, light blue), the PAMPTMA(+)$_{130}$-NaDC mixture at CR = 0.5 (black), and BR in water (gray). The polymer concentration was 0.1 wt%. All solutions contained 100 μM BR.

3.5 Thermoresponsive behavior

As described in **Paper III**, the thermoresponsive solution behavior of the mixed complexes at different CRs upon heating was studied for the PNIPAM$_{120}$-*b*-PAMPTMA(+)$_{30}$-NaDC system by using SLS, DLS, DSC, SAXS, and electrophoretic mobility methods. The results of these measurements are summarized in the following text.

For a pure copolymer solution, at temperatures well below T_{cp}, the PNIPAM$_{120}$-*b*-PAMPTMA(+)$_{30}$ copolymer was present as single chains that coexisted with loose multichain clusters according to previous studies on similar copolymers.[158,159] Upon increasing the temperature, aggregation started in the solution as reflected by an increasing clouding at the T_{cp}, which originated from the decrease in water solubility (dehydration) of PNIPAM at LCST. However, the dehydration of PNIPAM blocks was only partly due to the presence of the charged block (Figure 3.9). This was reflected

in a lower transition enthalpy as compared to the PNIPAM homopolymer (Table 1 in **Paper III**). Indeed, at 60 °C, SAXS revealed that free copolymer chains and a small fraction of small micelles with a dehydrated PNIPAM core coexisted with the clusters (Figure 3.10).

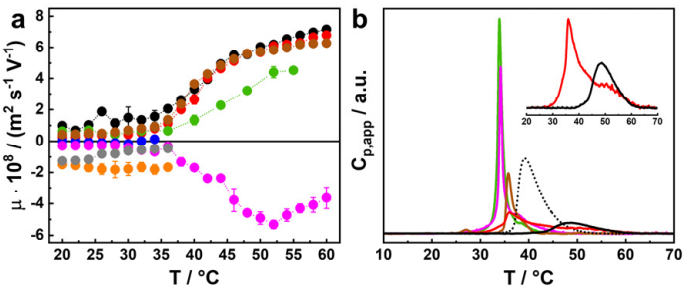

Figure 3.9 Temperature dependence of (a) the mean electrophoretic mobility (μ) and (b) DSC curves (inset: enlarged phase transition regime for X = 0 (black) and X = 0.2 (red)) for the PNIPAM$_{120}$-*b*-PAMPTMA(+)$_{30}$-NaDC aqueous mixtures at different negative charge fractions ($0 \leq X \leq 0.94$). Color code: X = 0 (black, pure copolymer solution), X = 0.2 (red), X = 0.33 (brown), X = 0.5 (green), X = 0.67 (blue), X = 0.8 (magenta), X = 0.89 (orange) and X = 0.94 (grey). The samples with X = 0.67, 0.89 and 0.94 were not investigated in the precipitation region that occurred at elevated temperatures. The copolymer concentrations were 0.13 wt% in (a), 0.5 wt% in (b) except for X = 0.33 and 0.5, where it was 0.25 wt%.

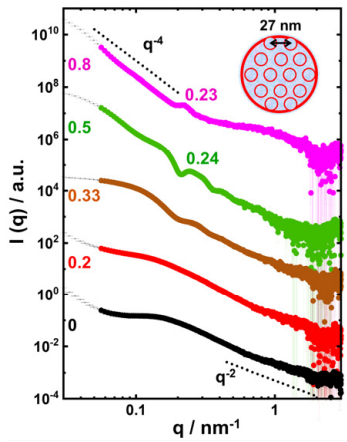

Figure 3.10 SAXS curves at 60 °C for the PNIPAM$_{120}$-*b*-PAMPTMA(+)$_{30}$-NaDC aqueous mixtures at different negative charge fractions ($0 \leq X \leq 8$). Color code: X = 0 (black, pure copolymer solution), X = 0.2 (red), X = 0.33 (brown), X = 0.5 (green), X = 0.67 (blue), X = 0.8 (magenta). The copolymer concentration was 0.5 wt%. The ordered nanoregions of the mixed aggregates at X = 0.8 were sketched to support the data interpretation.

With the addition of the NaDC to the copolymer, mixed complexes formed in the PNIPAM$_{120}$-*b*-PAMPTMA(+)$_{30}$-NaDC mixtures at room temperature through a preferential electrostatic interaction between the cationic PAMPTMA(+) blocks and the DC^- anions, as reported in **Paper I**. At low NaDC contents, X = 0.2 (corresponding to CR = 0.25) the neutralization (given by DC^-) triggered further dehydration of the

block copolymer at T_{cp} into denser aggregates with a positive μ (Figure 3.9a). The formation of the mixed complexes explains the increase in cooperativity of the transition in comparison to the pure copolymer as shown in the DSC curve (Figure 3.9b and Table 1 in **Paper III**). Above the transition temperature, at 60 °C, the SAXS results indicated that this mixture was an intermediate transition regime where the mixed aggregates formed with a core (radius of about 16 nm) of densely packed PNIPAM chains and a corona of PAMPTMA(+) blocks largely neutralized by DC^- (Figure 3.10). In addition, the clusters formed by partially DC^- anion-neutralized copolymer chains, small copolymer micelles, and free polymer chains were kept in the mixed solution.

As the NaDC content in the mixtures was increased to $0.33 \leq X \leq 0.5$ ($0.5 \leq CR \leq 1$), larger fractions of copolymers became engaged in the interaction with the BS molecules below T_{onset}. This gave rise to an increase in amplitude of the transition peaks in the corresponding DSC curves while T_{onset} decreased, approaching a value close to 32 °C (Figure 3.9b). The corresponding SAXS result at 60 °C suggested that further addition of BS led to the disappearance of the copolymer clusters and a slight growth of the copolymer-BS mixed aggregates, whose radii became about 20 nm at X = 0.33 and 0.5. At X = 0.5 (CR = 1), a further population of aggregates with a radius of approximately 40 nm was observed to contribute to the SAXS intensity, which was probably the prelude to the precipitation observed at higher X values.

With further increase in BS content to X = 0.8 (CR = 4), negatively charged mixed complexes existed in the mixed solution at 22 °C as indicated by the negative μ (Figures 3.1b and 3.9a). This sample expressed the highest cooperativity upon heating with a sharp DSC peak observed in Figure 3.9b. In addition, the SAXS curves revealed that a higher BS content at 60 °C promoted the formation of the copolymer-BS mixed aggregates with a microphase-separated interior consisting of nanoregions of dehydrated PNIPAM and PAMPTMA(+)/DC^-. The microphase-separated nanoregions had an inter-distance of about 27 nm according to the peak position (q = 0.23 nm^{-1}) in the SAXS profile (Figure 3.10). The mixed solutions at X = 0.67, 0.89 and 0.94 phase separated at higher temperatures and were therefore not further investigated.

4 Oppositely charged block copolymer-SDS mixtures

Due to the special rigid structures of BSs, the mixed complexes formed in different kinds of polymer-BS systems present fascinating supramolecular structures and thermoresponsive solution behaviors. As a comparative reference to the polymer-BS systems discussed in **Papers I–III**, mixtures of the same block copolymer (i.e., $PNIPAM_{65}$-*b*-$PAMPTMA(+)_{20}$) and a conventional head-tail surfactant (SDS) were investigated at varying compositions and temperatures by ITC, DSC, DLS, SAXS, and electrophoretic mobility methods. **Paper IV** describes this study and the results are summarized in the following subchapters.

4.1 Thermodynamic interactions

The thermodynamic interactions between $PNIPAM_{65}$-*b*-$PAMPTMA(+)_{20}$ and SDS were studied by the ITC method (Figure 4.1). The dilution of SDS micelles gave rise to endothermic enthalpy changes during titration, indicating that the demicellization of SDS was an entropy-driven process associated to the hydrophobic effect at 25 °C.[160–162] The CMC of SDS was estimated to be 8.6 mM at 25 °C (Figure S1 in **Paper IV**).

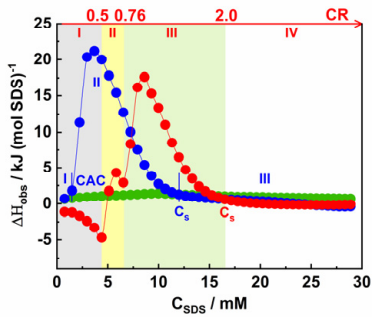

Figure 4.1 ITC curves of 200 mM SDS titrated into pure water (green), 0.5 wt% $PNIPAM_{71}$ (blue) and 0.5 wt% $PNIPAM_{65}$-*b*-$PAMPTMA(+)_{20}$ (red). The CAC, C_s, and different regions are marked with I, II, III, and IV. The temperature was 25.00 °C.

Interaction of SDS with homopolymer PNIPAM$_{71}$

In contrast to the PNIPAM$_{71}$-NaDC system described in **Paper II** where no obvious PNIPAM-NaDC interaction was detected, titration of SDS into the PNIPAM$_{71}$ homopolymer solution showed a clear CAC (= 1.5 mM) that was related to the cooperative micellization of PNIPAM$_{71}$ chain-bound SDS molecules. This demonstrated the hydrophobic interaction between PNIPAM$_{71}$ and SDS.[160,163–166] Three regions have been marked out in the ITC curve to easily follow the different steps of the binding process (Figure 4.1). *Region I* (0–1.5 mM) represents the demicellization of SDS micelles and the non-cooperative binding of SDS monomers to the polymer chains. *Region II* (1.5–12 mM) starts with a sharp increase at CAC at which SDS aggregates formed cooperatively at the polymer chains. The pronounced endothermic peak reflects the dehydration of polymer segments upon incorporation in the surfactant aggregates. Finally, the polymer chains became saturated at the end of this region (C_s = 12 mM).[163,167] In *Region III* (> 12 mM), free SDS micelles were eventually formed at higher SDS concentrations. The amount of polymer-bound SDS was estimated according to (C_s – CAC)/C(polymer)[167] to be about 17 SDS monomers per PNIPAM$_{71}$ chain, which suggests that one small SDS aggregate interacts with several PNIPAM$_{71}$ chains at this stage. This is a reasonable conclusion as SDS aggregates that bind to nonionic polymers are usually smaller than the corresponding free micelles.[168–171]

Interaction of SDS with PNIPAM$_{65}$-*b*-PAMPTMA(+)$_{20}$ copolymer

Titration of SDS into a PNIPAM$_{65}$-*b*-PAMPTMA(+)$_{20}$ block copolymer solution showed different trends from the PNIPAM$_{71}$-SDS system (Figure 4.1), implying that there were also other forms of interaction. Four titration regions were present in the PNIPAM$_{65}$-*b*-PAMPTMA(+)$_{20}$-SDS system.

Region I (0–4.4 mM, CR 0–0.5) represents the binding of one SDS micelle to several copolymer chains to form small PNIPAM$_{65}$-*b*-PAMPTMA(+)$_{20}$-SDS micellar aggregates, which was accompanied by an increase of the exothermic ΔH_{obs} values (Figure 4.1). The exothermic signal demonstrated that the interaction was primary of electrostatic origin thus leading to a preferential binding to the PAMPTMA(+) blocks in competition with the chloride counterions.[172] At 25 °C, DLS and electrophoretic mobility measurements on the pure copolymer solution revealed that the copolymer existed as clusters in addition to the single unimers. SDS may also associate to these clusters, thus inducing the formation of larger mixed aggregates (Figure 2 in **Paper IV**).

In *Region II* (4.4–6.5 mM, CR 0.5–0.76), the ΔH_{obs} increased from being exothermic to slightly endothermic, giving rise to a small peak in this region. Since the

PAMPTMA(+) blocks inside the copolymer-SDS mixed aggregates were neutralized at CR = 0.5, this region was therefore associated to the co-assembly process of $PNIPAM_{65}$-*b*-$PAMPTMA(+)_{20}$-SDS mixed aggregates into ordered mixed complexes where the rearrangement of the SDS micelles inside the complex took place. The endothermic signal revealed that the co-assembly mechanism had a relevant contribution of some entropy-driven processes probably related to this rearrangement, which could be accompanied with the release of counterions as discussed in ref.[173], leaving the PNIPAM blocks on the outside of the mixed complex.

In *Region III* (6.5–16.5 mM, CR 0.76–2.0), the large endothermic peak, which was similar to that in *Region II* of the $PNIPAM_{71}$-SDS ITC curve, implied a binding of SDS to the PNIPAM blocks through hydrophobic interactions. This binding process resulted in a dehydration of the PNIPAM blocks which continued until a saturation of the copolymers was reached at C_s. The amount of bound SDS to the $PNIPAM_{65}$ block was estimated to be 23 SDS monomers, which was in good agreement with the values obtained for the binding of SDS to $PNIPAM_{71}$. In this region, well-defined copolymer-SDS mixed complexes consisting of an ordered distribution of the SDS micelles were achieved at CR = 1 as indicated by SAXS (Figure 4.3).

In *Region IV* (16.5–28.9 mM, CR 2.0–3.8), the small nearly constant ΔH_{obs} values were related to the formation of free SDS micelles and the dilution of the micelles at higher concentrations.

4.2 Thermoresponsive behavior

In the absence of SDS, the pure block copolymer showed an aggregation behavior at an onset temperature of 36 °C (Figure 4.2a). A small addition of SDS did not have much influence on the aggregation temperature (36 °C), however, the size corresponding to the slow mode decreased compared to the copolymer clusters (CR = 0.25, Figure 4.2b), demonstrating the formation of copolymer-SDS mixed aggregates. With the addition of SDS up to CR = 0.5, large mixed aggregates were formed, with an electrophoretic mobility equal to zero (Figure 5 in **Paper IV**). However, the solution phase separated above 30 °C (Figure 4.2c). A small-amplitude DSC peak appeared at around 33 °C while the main peak remained at the same position as the pure copolymer although with a slightly higher ΔH_{tr} (Figure 7a and Table 1 in **Paper IV**). The μ value of zero measured at CR = 0.5 indicated that there remained free copolymer chains in the mixed solution that were not involved in the interaction with SDS below the phase transition. The main DSC peak was thus attributed to those non-interacting chains

while the small pre-peak was related to the phase separation, as detected in the DLS result (Figure 4.2c).

With continually increasing SDS concentrations at CR = 1 and 2, the mixtures did not phase separate at elevated temperatures and well-defined monomodal size distribution corresponding to the mixed complexes were found at all temperatures investigated (Figure 4.2d, e). The phase transition peak shifted to 48.6 °C in the case of CR = 1 and thereafter disappeared at CR = 2 (Figure 7a in **Paper IV**). The binding of SDS to the PNIPAM block shielded the polymer and thereby suppressed its dehydration upon raising the temperature, thus increasing the phase transition temperature of the mixture. This result was also verified in the $PNIPAM_{71}$-SDS mixtures where the transition peak shifted to higher temperature with a small addition of SDS and disappeared upon increasing the SDS content in the mixture (Figure 7b and Table 1 in **Paper IV**).

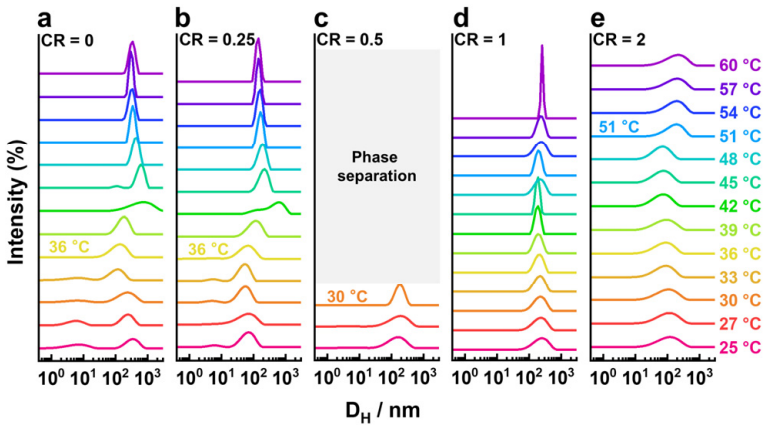

Figure 4.2 Intensity-weighted hydrodynamic diameter (D_H) distributions from CONTIN analysis of DLS data for $PNIPAM_{65}$-*b*-$PAMPTMA(+)_{20}$-SDS mixtures at different CRs and temperatures varying between 25 and 60 °C. (a) CR = 0, (b) CR = 0.25, (c) CR = 0.5, (d) CR = 1, and (e) CR = 2. The copolymer concentration was 0.1 wt%.

4.3 Ordered internal structure of mixed complexes

At 25 °C, the SAXS curve of the $PNIPAM_{65}$-*b*-$PAMPTMA(+)_{20}$-SDS mixture at CR = 1 showed a Bragg peak at relatively high q (= 1.55 nm^{-1}) (Figure 3 in **Paper IV**). A similar peak has been observed and interpreted in earlier studies,[174–176] and based on these interpretations, the structural peak was linked to an ordered distribution of SDS micelles in the interior of the mixed complex and corresponds to an inter-micellar distance of $d = 2\pi/q \approx 4.05$ nm.

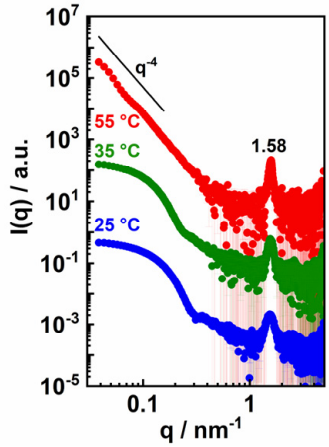

Figure 4.3 SAXS curves of PNIPAM$_{65}$-*b*-PAMPTMA(+)$_{20}$-SDS mixed solution at CR = 1 with elevated temperatures: 25 °C (blue), 35 °C (green), and 55 °C (red). The q value of the Bragg peak at 55 °C and the slope expected for q^{-4} Porod law decay are indicated. The curves have been shifted on the y-axis by a suitable factor to avoid data overlap. The copolymer concentration was 0.12 wt%.

When increasing temperatures to 35 and 55 °C, even though the mixed complexes grew, their internal structure did not change, as expressed by the constant peak position in the SAXS curves (Figure 4.3). However, the curves could not provide any information on the maximum particle size as the mixed complexes reached average dimensions well beyond the Guinier limit. It can be noticed that the curve at 55 °C changed to follow a Porod law of q^{-4} in the lower q range (Figure 4.3), corresponding to the tail of the scattering profile of these large structures, and which was predicted for particles with a sharp interface according to the Porod law.

5 Gemini surfactant-bile salt mixtures

The fascinating co-assembly and intriguing supramolecular structures found in oppositely charged polymer-BS systems discussed in **Chapter 3** were so inspiring that it was of interest to further explore the potential of BS co-assembly by studying their interaction with other amphiphiles. As introduced in **Chapter 1.3**, gemini surfactants are unconventional surfactants with interesting performances, just like BSs. Therefore, a system consisting of BS (NaDC) and cationic gemini surfactants including two chiral enantiomers ((2*S*,3*S*)-12-4(OH)$_2$-12 and (2*R*,3*R*)-12-4(OH)$_2$-12), and the racemate ((±)12-4(OH)$_2$-12) (see Figure 1.3) was studied and is described in **Paper V**. The results are summarized in the following subchapters.

5.1 Phase behavior and coacervation

The mixed solutions of a gemini surfactant and NaDC are expressed as a negative-to-positive molar charge ratio (CR = n_-/n_+), where n_- and n_+ are the number of moles of negative charge (= number of moles of NaDC) and the number of moles of positive charge (= 2 × number of moles of the gemini surfactants), respectively. Five phase transition regions were found when titrating NaDC into three gemini surfactants (Figure 5.1). The phase transition in each region could be summarized by taking the (2*S*,3*S*)-12-4(OH)$_2$-12-NaDC system as an example.

Region I (CR < 0.18): the very low turbidity (Figure 5.1a, b), the transparent appearance (Figure 5.1d) and the relatively large hydrodynamic diameters of 174 nm and 185 nm at CR = 0.1 and 0.2, respectively, (Figure 3 in **Paper V**) indicate the formation of gemini surfactant-rich mixed aggregates at low BS concentrations (≤ 0.72 mM).

Region II (0.18–0.32): the slightly increased turbidity of the mixtures (Figure 5.1b) and the fact that the mixed solution became slightly turbid at CR = 0.3 (Figure 5.1d) with a D_H = 209 nm (Figure 3 in **Paper V**) suggests a growth of the mixed aggregates, implying that they could be the precursors of the coacervate phase in the coacervation region.

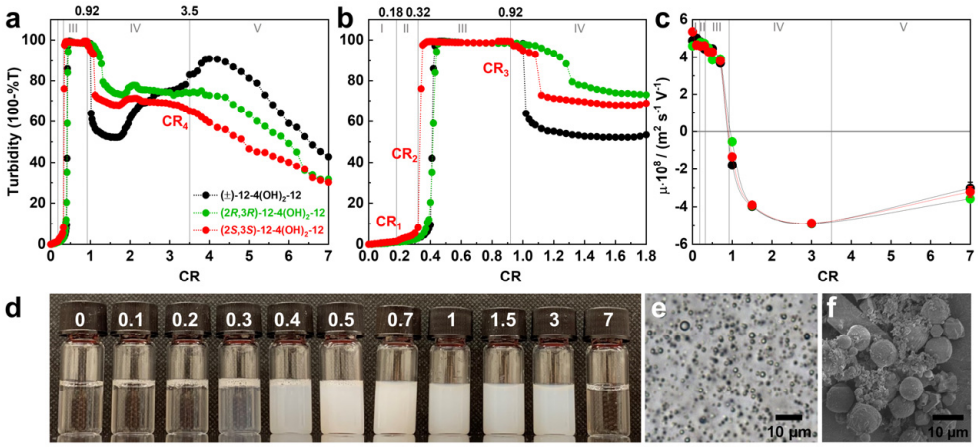

Figure 5.1 (a) Turbidity (100 – %T) curves obtained by titrating 40 mM BS into three gemini surfactants, (T denotes transmittance). (b) Enlarged turbidity curves at low values of NaDC concentration and CR. (c) Electrophoretic mobility (μ) of the gemini surfactant-NaDC mixed solutions at different CRs. Color code: (2*S*,3*S*)-12-4(OH)$_2$-12-NaDC mixtures (red), (±)-12-4(OH)$_2$-12-NaDC mixtures (black), and (2*R*,3*R*)-12-4(OH)$_2$-12-NaDC mixtures (green). Five transition regions were marked as I, II, III, IV, and V for the (2*S*,3*S*)-12-4(OH)$_2$-12-NaDC system as an example. (d) Visual inspection of the (2*S*,3*S*)-12-4(OH)$_2$-12-NaDC mixed solutions at different CRs (0–7), CR = 0 means the pure gemini surfactant solution. (e) Example of the optical microscopy image showing the coacervate droplets in (2*S*,3*S*)-12-4(OH)$_2$-12-NaDC mixture at CR = 0.7. (f) Cryo-SEM image of the (±)-12-4(OH)$_2$-12-NaDC mixtures at CR = 1.5. The concentration of gemini surfactants was kept at 2 mM for all the solutions.

Region III (0.32–0.92): the sharp increase in turbidity to its highest value after which it was maintained constant is the typical phenomenon of coacervation. This was also demonstrated by the very turbid visual appearances (Figure 5.1d) of the mixed solutions at CR = 0.5 and 0.7, originating from the coacervate droplets observed by optical microscopy (Figure 5.1e). The μ of the samples in this region was positive.

Region IV (0.92–3.5): the fact that the turbidity declined to another plateau but still presented relatively high values, accompanied by the still turbid appearance and the negative μ values of the mixed solutions at CR = 1, 1.5 and 3, led to the conclusion that this region corresponded to the charge-reversed coacervation regime as NaDC was in excess in these mixtures.

Region V (CR > 3.5): the gradual decrease in turbidity, and the fact that the mixed solutions became clear again at CR = 7 (Figure 5.1d) indicated the redissolution of the coacervate droplets. This finally led to the formation of BS-rich mixed micelles at higher BS concentrations.

The transition regions and critical concentrations or CRs for the three gemini surfactant-BS systems are summarized in Tables 1 and S1 in **Paper V**. From the comparison of the critical CRs and the differences between the turbidity curves at around CR = 0.4 (Figure 5.1b), it was obvious that the sharp increase in turbidity took

place early on during the titration of the NaDC solution into the (2*S*,3*S*)-12-4(OH)$_2$-12 gemini surfactant solution. This means that, given the same gemini surfactant concentration, the (2*S*,3*S*)-12-4(OH)$_2$-12 recognized and interacted with NaDC at a lower BS concentration than the other two gemini surfactants, thus having a higher receptivity to the BS molecules.

5.2 Thermodynamic interactions

Thermodynamic interactions in the three gemini surfactant-BS systems were investigated by ITC and the results are shown in Figure 5.2a. The differences between them are also observed by evident shifts in the ITC curves, which was consistent with the turbidity results (Figure 5.1a, b).

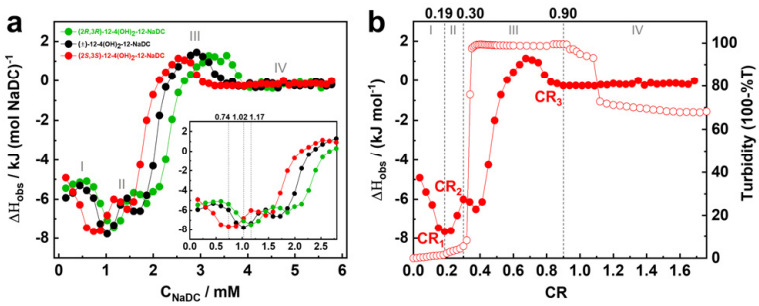

Figure 5.2 (a) ITC curves of 40 mM NaDC micellar solution titrated into (2*S*,3*S*)-12-4(OH)$_2$-12 (red), (±)-12-4(OH)$_2$-12 (black), and (2*R*,3*R*)-12-4(OH)$_2$-12 (green) solutions at 25.00 °C. The inset shows the ITC curves at low NaDC concentration and CR. (b) ITC (filled symbols) and turbidity (unfilled symbols) curves of titrating NaDC micellar solution into (2*S*,3*S*)-12-4(OH)$_2$-12. The gemini surfactant concentration was kept at 2 mM, while 40 mM and 200 mM NaDC were used for the ITC and turbidity experiments, respectively.

Except for the shifts in three ITC curves, these curves showed exactly the same trends. From these, four regions could be determined, which were in good agreement with the regions dividing the turbidity curves (Figure 5.1b). The thermodynamic event in each region was summarized for the (2*S*,3*S*)-12-4(OH)$_2$-12-NaDC system by combining the ITC results with the turbidity results (Figure 5.2b). In *Region I* (CR < 0.19), the increased exothermic ΔH_{obs} was related to the demicellization of NaDC micelles and the monomer binding with the gemini surfactant micelles to form gemini surfactant-rich mixed aggregates mainly through electrostatic attraction. In *Region II* (0.19–0.3), the less exothermic ΔH_{obs} indicates that besides the electrostatic attraction, other forms of interaction, such as hydrophobic interaction and hydrogen bonding, were involved during the growth of the mixed aggregates. With further titration of NaDC, the ΔH_{obs} increased steeply and went from exothermic ($\Delta H_{obs} < 0$) to endothermic ($\Delta H_{obs} > 0$),

which finally led to a second large transition peak in *Region III* (CR 0.3–0.9). This suggests that the electrostatic association between NaDC and the gemini surfactant gradually reached a saturation due to mixed aggregates becoming less and less charged upon further BS addition, while the hydrophobic interaction and hydrogen bonding became stronger and stronger, finally dominating the transition process towards coacervation. The formation of the coacervate droplets were driven by the entropy gain from the release of water and counterions during this association. Finally, all the charge sites in the oppositely charged surfactants were neutralized in *Region IV* (CR > 0.9), and zero ΔH_{obs} values were observed in this region.

5.3 Chirality

The chirality in the three gemini surfactant-NaDC mixtures was investigated by using the bilirubin-IXα as a probe to obtain CD signals. As mentioned before, the left-handed and right-handed signals are present in the CD spectra when M- and P-forms of BR are selected to interact with chiral species, respectively (Figure 2.11).[136–138,177] From now on, for an easier understanding of this system, the notation R-BR (i.e., BR with right-handed chirality) is used to represent the P-form of BR, and L-BR (i.e., BR with left-handed chirality) is utilized to represent the M-form of BR.

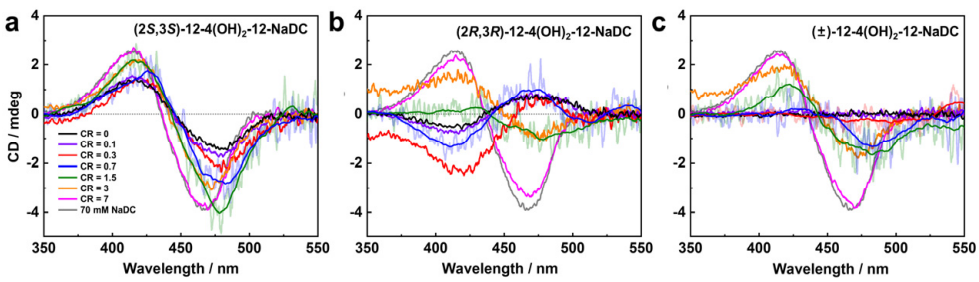

Figure 5.3 CD spectra of (a) (2*S*,3*S*)-12-4(OH)$_2$-12-NaDC, (b) (2*R*,3*R*)-12-4(OH)$_2$-12-NaDC, and (c) (±)-12-4(OH)$_2$-12-NaDC mixtures at CR = 0 (black), CR = 0.1 (purple), CR = 0.3 (red), CR = 0.7 (blue), CR = 1.5 (green), CR = 3 (orange), and CR = 7 (magenta). The trends of the noisy signal at CR = 0.7 and 1.5 (also CR = 0.3 in (c)) have been presented as smooth lines to facilitate the comparison. CD spectra of the 70 mM NaDC solution (gray) corresponding to the NaDC concentration in the mixture at CR = 7 is also presented. The gemini surfactant concentration was 5 mM. All solutions contained 100 μM BR.

It has been reported that NaDC micelles and monomers interact with L-BR and R-BR, showing a left-handed and a right-handed CD signal, respectively.[157,178] In our case, the left-handed chirality was detected when the L-BR interacted preferentially with the NaDC micelles at high concentrations (> 20 mM). At lower concentration, on the

other hand, the right-handed CD signal that was observed suggested an interaction between NaDC monomers and R-BR (Figure S11 in **Paper V**).

In the case of (2*S*,3*S*)-12-4(OH)$_2$-12-NaDC mixtures at different CRs, a left-handed CD signal was found (Figure 5.3a), implying that the L-BR can be selected by the (2*S*,3*S*)-12-4(OH)$_2$-12-NaDC mixed aggregates and coavervates. However, the recognition capabilities of the mixtures showed differences at different CRs. The mixed aggregates had similar recognition capabilities as the pure gemini surfactant micelles at low CRs (< 0.3), whereas the recognition capability was significantly enhanced by the (2*S*,3*S*)-12-4(OH)$_2$-12-NaDC coacervates in the coacervation region (CR 0.3–3.5). This enhancement reached the highest extent at CR = 1.5. It should be stressed that the NaDC concentration in the mixtures was ≤ 15 mM when CR ≤ 1.5, and the monomer CD signal of NaDC (right-handed) was observed for the pure BS solution when its concentration ≤ 20 mM (Figure S11 in **Paper V**). At high CRs in the redissolution region, the same recognition capability of the BS-rich mixed micelles at CR = 7 as for the pure BS micelles at a concentration identical to the one in the mixture (70 mM) is observed (Figure 5.3a).

In the (2*R*,3*R*)-12-4(OH)$_2$-12-NaDC mixtures (Figure 5.3b), the right-handed CD signals observed when CR < 1.5 suggested that R-BR was recognized by the (2*R*,3*R*)-12-4(OH)$_2$-12-NaDC mixed aggregates/coacervates. However, an inversion of the CD signal was observed when CR reached 1.5, indicating the selection of L-BR started instead. Therefore, the inversion of CD signals verified that a specific enantioselective capability of the (2*R*,3*R*)-12-4(OH)$_2$-12-NaDC mixed aggregates/coacervates to different forms of BR can be switched by the modulation of CRs.

The aqueous solution of the racemate (±)-12-4(OH)$_2$-12, i.e., the 1:1 mixture of the (2*S*,3*S*)-12-4(OH)$_2$-12 and (2*R*,3*R*)-12-4(OH)$_2$-12, did not present any CD signal (Figure 5.3c), reflecting that there was no recognition of any forms of the BR by the racemate micelles. It was therefore surprising to see a small indication of a left-handed CD signal at CR = 0.3 and this signal became more evident at CR ≥ 0.7, indicating that the capability to recognize L-BR was induced by mixing the achiral racemate with NaDC at CR ≥ 0.3. This finding also implies that the induced chirality in racemate-BS system was caused by the unequal interaction of the NaDC with two chiral gemini surfactants in the racemate, i.e., NaDC preferred to interact with (2*S*,3*S*)-12-4(OH)$_2$-12, thus resulting in the same left-handed CD signal as the one found for the (2*S*,3*S*)-12-4(OH)$_2$-12-NaDC system.

Conclusions and outlook

The papers included in this thesis have focused on the interaction of bile salt with oppositely charged amphiphiles such as diblock copolymers and chiral gemini surfactants. The reasons for gaining understanding of this interaction have varied. One objective was to search for suitable cationic block copolymers that show potential as new BS sequestrants in order to treat BS-related diseases and hypercholesterolemia. Another aim was to determine means to design supramolecular assemblies that can be used in biomedical applications such as drug loading and delivery, especially when these assemblies possess specific properties like chirality and thermoresponsive property. Moreover, building supramolecular structures on a hierarchical level from the bottom up by non-covalent interactions of molecular building blocks (like BSs and copolymers) has always been a fascination of modern science aimed at manufacturing reversible functional materials. Based on these motivations, the thesis has been divided into three parts. The following text gives a summary of the thesis as a whole, including conclusions and outlooks.

In the first part based on **Papers I–III**, oppositely charged block copolymer-BS systems were investigated. Two kinds of cationic block copolymers (PNIPAM$_m$-*b*-PAMPTMA(+)$_n$ and MPEG$_{45}$-*b*-PAMPTMA(+)$_{21}$), one cationic homopolymer (PAMPTMA(+)$_{130}$), and the nonionic homopolymer (PNIPAM$_m$) were selected in order to explore their interaction with the BS (NaDC). It was first demonstrated that single supramolecular helices of NaDC were formed in the PAMPTMA(+)$_{130}$-NaDC system. These helices could be condensed into different hierarchical arrangements such as orderly parallel structures and hexagonal packed bundles or toroids by using PNIPAM$_m$-*b*-PAMPTMA(+)$_n$ or MPEG$_{45}$-*b*-PAMPTMA(+)$_{21}$ block copolymers instead of the PAMPTMA(+)$_{130}$ homopolymer.

All in all, the different supramolecular assemblies formed in the polymer-BS systems suggest that the structures of the mixed complexes can be tuned by manipulating the charge composition of the mixtures and modifying the chemical composition of the polymers, to meet the requirement of desired applications. Moreover, the molecular chirality of the BS and the supramolecular chirality of the BS helices obtained in polymer-NaDC systems give the supramolecular mixed structures the ability to load

drugs, demonstrated with bilirubin-IXα, which highlights the potential application of these systems for drug encapsulation and delivery purposes.

The observed heat-induced phase transitions of the $PNIPAM_{120}$-*b*-$PAMPITA(+)_{30}$-NaDC system demonstrated the accomplishment of thermoresponsive mixed complexes. The addition of NaDC to the copolymer solution lowered the transition temperature and increased the cooperativity in different extents at different charge compositions. This suggests that the mixed aggregates had an appealing composition-controlled thermoresponsive behavior turning them into versatile nanomaterials that can be easily adapted to diverse applications. Moreover, the system phase-separated at body temperature at the highest NaDC fractions investigated, implying that it would be very promising for the oppositely charged block copolymer to act as a new BS sequestrant.

The intriguing supramolecular structures, chirality and thermoresponsive behavior found in the oppositely charged polymer-BS systems studied in this thesis led to a big effort when it comes to fundamental studies from a physico-chemical perspective. Although a preliminary exploration of a drug (bilirubin-IXα) loading application has been conducted and a good result obtained, there is still significant room for similar kinds of biomedical applications. Therefore, future studies on the drug loading and delivery performance of polymer-BS mixed complexes with special supramolecular structures would be appreciated.

It is also believed that this kind of application would benefit highly from the chiral and thermoresponsive properties of the mixed complexes. The formation of supramolecular mixed complexes in the copolymer-BS mixtures have also given promising indications for potential use of biocompatible cationic block copolymers in BS sequestration. However, the practical application has yet to be tested by relevant experiments. Thus, an investigation of the BS binding efficiency of the different block copolymers deserves more attention and effort in the future.

The second part of this thesis (**Paper II**) describes the investigation of the oppositely charged block copolymer-SDS system and compares it to its copolymer-BS counterpart. It was proved that the conventional head-tail surfactant SDS interacted with both the PNIPAM and PAMPTMA(+) blocks of the copolymer, conversely to the copolymer-NaDC systems where the NaDC molecules preferred to interact with the cationic blocks. The difference in the interaction behaviors of SDS compared with NaDC resulted in a specific thermoresponsive behavior of the copolymer-SDS mixed complexes upon heating: the phase separation induced by the PNIPAM dehydration occurred below the charge neutral composition while well-defined and stable aggregates

were formed above the charge-neutrality point due to overcharging. In addition, indications of an ordered internal structure in the copolymer-SDS mixed complexes were found at both ambient and elevated temperatures. However, the detailed morphology and structure of the mixed complexes in this system were not examined further at this stage, and should therefore be explored in coming studies.

The unique supramolecular assembly properties found in the copolymer-BS systems of this thesis originated from the chiral nature of the BS molecule. Therefore, the modulation of the chiral properties of another kind of unconventional surfactant, namely chiral gemini surfactants, through the interaction with BS was investigated in the last part of the thesis (**Paper V**). With the addition of NaDC, the phase behavior and the corresponding chirality of three gemini surfactants ((2*S*,3*S*)-12-4(OH)$_2$-12, (±)-12-4(OH)$_2$-12, and (2*R*,3*R*)-12-4(OH)$_2$-12) could be significantly changed.

Basically, five regions were observed in the phase behavior, corresponding to the formation of gemini surfactant-rich mixed aggregates, growth of the aggregates, coacervation, charge-reversed coacervation, and redissolution (BS-rich mixed aggregates/micelles). The coacervation occurred in the gemini surfactant-NaDC systems in a rather broad composition range. In addition, there were distinct differences in the interaction and phase behavior of these three gemini surfactant-BS systems, demonstrating that NaDC can recognize and interact with three gemini surfactants in different manners. Moreover, the chirality of the gemini surfactants (2*S*,3*S*)-12-4(OH)$_2$-12, (2*R*,3*R*)-12-4(OH)$_2$-12, and (±)-12-4(OH)$_2$-12 was enhanced, switched, and induced, respectively, by the addition of NaDC at specific compositions.

Coacervation has attracted great interest in applications such as wastewater treatment, pharmaceutical encapsulations, and mimicking protocells by using coacervate droplets as artificial cells. Therefore, the coacervation formed in the gemini surfactant-BS mixtures discussed in this thesis with tunable chiral properties in a wide range of compositions can be very competitive for potential use in these types of applications, which could thus be an interesting direction for future work in this area.

References

1 A. F. Hofmann and K. J. Mysels, Bile salts as biological surfactants, *Colloids and Surfaces*, 1987, **30**, 145–173.

2 N. A. Malik, Solubilization and interaction studies of bile salts with surfactants and drugs: A review, *Appl. Biochem. Biotechnol.*, 2016, **179**, 179–201.

3 M. C. di Gregorio, L. Travaglini, A. Del Giudice, J. Cautela, N. V. Pavel and L. Galantini, Bile Salts: Natural surfactants and precursors of a broad family of complex amphiphiles, *Langmuir*, 2019, **35**, 6803–6821.

4 D. Madenci and S. U. Egelhaaf, Self-assembly in aqueous bile salt solutions, *Curr. Opin. Colloid Interface Sci.*, 2010, **15**, 109–115.

5 K. Kano, S. Tatemoto and S. Hashimoto, Specific interactions between sodium deoxycholate and its water-insoluble analogues. Mechanisms for premicelle and micelle formation of sodium deoxycholate, *J. Phys. Chem.*, 1991, **95**, 966–970.

6 P. Garidel, A. Hildebrand, R. Neubert and A. Blume, Thermodynamic characterization of bile salt aggregation as a function of temperature and ionic strength using isothermal titration calorimetry, *Langmuir*, 2000, **16**, 5267–5275.

7 B. R. Simonović and M. Momirović, Determination of critical micelle concentration of bile acid salts by micro-calorimetric titration, *Mikrochim. Acta*, 1997, **127**, 101–104.

8 L. Galantini, M. C. di Gregorio, M. Gubitosi, L. Travaglini, J. V. Tato, A. Jover, F. Meijide, V. H. Soto Tellini and N. V. Pavel, Bile salts and derivatives: Rigid unconventional amphiphiles as dispersants, carriers and superstructure building blocks, *Curr. Opin. Colloid Interface Sci.*, 2015, **20**, 170–182.

9 L. Galantini, E. Giglio, A. Leonelli and N. V. Pavel, An integrated study of small-angle X-ray scattering and dynamic light scattering on cylindrical micelles of sodium glycodeoxycholate, *J. Phys. Chem. B*, 2004, **108**, 3078–3085.

10 F. Lopez, J. Samseth, K. Mortensen, E. Rosenqvist and J. Rouch, Micro- and macrostructural studies of sodium deoxycholate micellar complexes in aqueous solutions, *Langmuir*, 1996, **12**, 6188–6196.

11 E. F. Marques, H. Edlund, C. La Mesa and A. Khan, Liquid crystals and phase equilibria binary bile salt-water systems, *Langmuir*, 2000, **16**, 5178–5186.

12 T. M. Šarenac and M. Mikov, Bile acid synthesis: From nature to the chemical modification and synthesis and their applications as drugs and nutrients, *Front. Pharmacol.*, 2018, **9**, 1–22.

13 M. Gubitosi, J. V. Trillo, A. Alfaro Vargas, N. V. Pavel, D. Gazzoli, S. Sennato, A. Jover, F. Meijide and L. Galantini, Characterization of carbon nanotube dispersions in solutions of bile salts and derivatives containing aromatic substituents, *J. Phys. Chem. B*, 2014, **118**, 1012–1021.

14 H. Zughaid, B. Forbes, G. P. Martin and N. Patel, Bile salt composition is secondary to bile salt concentration in determining hydrocortisone and progesterone solubility in intestinal mimetic fluids, *Int. J. Pharm.*, 2012, **422**, 295–301.

15 T. S. Wiedmann and L. Kamel, Examination of the solubilization of drugs by bile salt micelles, *J. Pharm. Sci.*, 2002, **91**, 1743–1764.

16 J. R. F. Walters and S. S. Pattni, Managing bile acid diarrhoea, *Therap. Adv. Gastroenterol.*, 2010, **3**, 349–357.

17 E. Heřmánková, A. Žák, L. Poláková, R. Hobzová, R. Hromádka and J. Širc, Polymeric bile acid sequestrants: Review of design, in vitro binding activities, and hypocholesterolemic effects, *Eur. J. Med. Chem.*, 2018, **144**, 300–317.

18 I. W. Hamely, *The physics of block copolymers*, Oxford University Press, New York, 1998.

19 H. Feng, X. Lu, W. Wang, N. G. Kang and J. W. Mays, Block copolymers: Synthesis, self-assembly, and applications, *Polymers (Basel).*, 2017, **9**, 494.

20 G. Riess, Micellization of block copolymers, *Prog. Polym. Sci.*, 2003, **28**, 1107–1170.

21 L. Zhang and A. Eisenberg, Multiple morphologies and characteristics of 'crew-cut' micelle-like aggregates of polystyrene-b-poly(acrylic acid) diblock copolymers in aqueous solutions, *J. Am. Chem. Soc.*, 1996, **118**, 3168–3181.

22 I. W. Hamley, Nanostructure fabrication using block copolymers, *Nanotechnology*, 2003, **14**, R39.

23 Y. Mai and A. Eisenberg, Self-assembly of block copolymers, *Chem. Soc. Rev.*, 2012, **41**, 5969–5985.

24 K. Kataoka, A. Harada and Y. Nagasaki, Block copolymer micelles for drug delivery: Design, characterization and biological significance, *Adv. Drug Deliv. Rev.*, 2001, **47**, 113–131.

25 P. Alexandridis and B. Lindman, *Amphiphilic block copolymers: Self-assembly and applications*, Elsevier Science B.V., Amsterdam, 2000.

26 M. Gradzielski and I. Hoffmann, Polyelectrolyte-surfactant complexes (PESCs) composed of oppositely charged components, *Curr. Opin. Colloid Interface Sci.*, 2018, **35**, 124–141.

27 N. Khan and B. Brettmann, Intermolecular interactions in polyelectrolyte and surfactant complexes in solution, *Polymers (Basel).*, 2019, **11**, 51.

28 I. K. Voets, A. De Keizer and M. A. C. Stuart, Complex coacervate core micelles, *Adv. Colloid Interface Sci.*, 2009, **147**, 300–318.

29 A. B. Ebrahim Attia, Z. Y. Ong, J. L. Hedrick, P. P. Lee, P. L. R. Ee, P. T. Hammond and Y. Y. Yang, Mixed micelles self-assembled from block copolymers for drug delivery, *Curr. Opin. Colloid Interface Sci.*, 2011, **16**, 182–194.

30 H. G. Schild, Poly(N-isopropylacrylamide): Experiment, theory and application, *Prog. Polym. Sci.*, 1992, **17**, 163–249.

31 V. Aseyev, H. Tenhu and F. M. Winnik, Non-ionic thermoresponsive polymers in water, *Adv. Polym. Sci.*, 2011, **242**, 29–89.

32 J. E. Betancourt and J. M. Rivera, Nonpolymeric thermosensitive supramolecules, *J. Am. Chem. Soc.*, 2009, **131**, 16666–16668.

33 A. Halperin, M. Kröger and F. M. Winnik, Poly(N-isopropylacrylamide) phase diagrams: Fifty years of research, *Angew. Chem. Int. Ed.*, 2015, **54**, 15342–15367.

34 C. Scherzinger, A. Schwarz, A. Bardow, K. Leonhard and W. Richtering, Cononsolvency of poly-N-isopropyl acrylamide (PNIPAM): Microgels versus linear chains and macrogels, *Curr. Opin. Colloid Interface Sci.*, 2014, **19**, 84–94.

35 M. Alaghemandi and E. Spohr, Molecular dynamics investigation of the thermo-responsive polymer poly(N-isopropylacrylamide), *Macromol. Theory Simulations*, 2012, **21**, 106–112.

36 R. Pamies, K. Zhu, A. L. Kjøniksen and B. Nyström, Thermal response of low molecular weight poly-(N-isopropylacrylamide) polymers in aqueous solution, *Polym. Bull.*, 2009, **62**, 487–502.

37 H. Wei, S. X. Cheng, X. Z. Zhang and R. X. Zhuo, Thermo-sensitive polymeric micelles based on poly(N-isopropylacrylamide) as drug carriers, *Prog. Polym. Sci.*, 2009, **34**, 893–910.

38 R. Sharma, A. Kamal, M. Abdinejad, R. K. Mahajan and H. B. Kraatz, Advances in the synthesis, molecular architectures and potential applications of gemini surfactants, *Adv. Colloid Interface Sci.*, 2017, **248**, 35–68.

39 C. A. Bunton, L. Robinson, M. F. Stam and J. Schaak, Catalysis of nucleophilic substitutions by micelles of dicationic detergents, *J. Org. Chem.*, 1971, **36**, 2346–2350.

40 M. FM and L. CA., Gemini surfactants: Synthesis and propertie, *J Am Chem Soc*, 1991, 1451–1452.

41 M. J. AsRosen, Geminis: A new generation of surfactants, *Chemtech*, 1993, 30–33.

42 R. Zana, Dimeric and oligomeric surfactants. Behavior at interfaces and in aqueous solution: A review, *Adv. Colloid Interface Sci.*, 2002, **97**, 205–253.

43 Y. Han and Y. Wang, Aggregation behavior of gemini surfactants and their interaction with macromolecules in aqueous solution, *Phys. Chem. Chem. Phys.*, 2011, **13**, 1939–1956.

44 Y. Wang, Y. Han, X. Huang, M. Cao and Y. Wang, Aggregation behavior of a series of anionic sulfonate gemini surfactants and their corresponding monomeric surfactant, *J. Colloid Interface Sci.*, 2008, **319**, 534–541.

45 A. J. Kirby, P. Camilleri, J. B. F. N. Engberts, M. C. Feiters, R. J. M. Nolte, O. Söderman, M. Bergsma, P. C. Bell, M. L. Fielden, C. L. García Rodríguez, P. Guédat, A. Kremer, C. McGregor, C. Perrin, G. Ronsin and M. C. P. Van Eijk, Gemini surfactants: New synthetic vectors for gene transfection, *Angew. Chem. Int. Ed.*, 2003, **42**, 1448–1457.

46 M. S. Kamal, A Review of gemini surfactants: Potential application in enhanced oil recovery, *J. Surfactants Deterg.*, 2016, **19**, 223–236.

47 C. Bombelli, G. Caracciolo, P. Di Profio, M. Diociaiuti, P. Luciani, G. Mancini, C. Mazzuca, M. Marra, A. Molinari, D. Monti, L. Toccacieli and M. Venanzi, Inclusion of a photosensitizer in liposomes formed by DMPC/gemini surfactant: Correlation between physicochemical and biological features of the complexes, *J. Med. Chem.*, 2005, **48**, 4882–4891.

48 L. Caillier, E. Taffin de Givenchy, R. Levy, Y. Vandenberghe, S. Geribaldi and F. Guittard, Polymerizable semi-fluorinated gemini surfactants designed for antimicrobial materials, *J. Colloid Interface Sci.*, 2009, **332**, 201–207.

49 W. Xiao, K. H. Ernst, K. Palotas, Y. Zhang, E. Bruyer, L. Peng, T. Greber, W. A. Hofer, L. T. Scott and R. Fasel, Microscopic origin of chiral shape induction in achiral crystals, *Nat. Chem.*, 2016, **8**, 326–330.

50 C. Bello, C. Bombelli, S. Borocci, P. Di Profio and G. Mancini, Role of the spacer stereochemistry on the aggregation properties of cationic gemini surfactants, *Langmuir*, 2006, **22**, 9333–9338.

51 L. Zhou, J. Yue, Y. Fan and Y. Wang, Self-assembly and chiral recognition of chiral cationic gemini surfactants, *Langmuir*, 2018, **34**, 12924–12933.

52 G. Caracciolo, D. Pozzi, G. Mancini and R. Caminiti, Role of the spacer stereochemistry on the structure of solid-supported gemini surfactants aggregates, *Langmuir*, 2007, **23**, 10040–10043.

53 D. A. Jaeger, E. Kubicz-Loring, R. C. Price and H. Nakagawa, Vesicular properties of stereoisomeric surfactants, *Langmuir*, 1996, **12**, 5803–5808.

54 B. Vijai Shankar and A. Patnaik, Chiral discrimination of a gemini-type surfactant with rigid spacer at the air-water interface, *J. Phys. Chem. B*, 2007, **111**, 11419–11427.

55 P. Zhang, J. Ma, X. Kang, H. Liu, C. Chen, Z. Zhang, J. Zhang and B. Han, Switching chirality in the assemblies of bio-based amphiphiles solely by varying their alkyl chain length, *Chem. Commun.*, 2017, **53**, 2162–2165.

56 T. G. Barclay, K. Constantopoulos and J. Matisons, Nanotubes self-assembled from amphiphilic molecules via helical intermediates, *Chem. Rev.*, 2014, **114**, 10217–10291.

57 G. A. Ferreira and W. Loh, Liquid crystalline nanoparticles formed by oppositely charged surfactant-polyelectrolyte complexes, *Curr. Opin. Colloid Interface Sci.*, 2017, **32**, 11–22.

58 F. E. Schwartz, A.M.; Perry, J.W.; Bartell, Surface active agents, *J. Phys. Colloid Chem.*, 1949, 1467.

59 E. D. Goddard, Polymer/surfactant interaction-Its relevance to detergent systems, *J. Am. Oil Chem. Soc.*, 1994, **71**, 1–16.

60 L. Piculell, J. Norrman, A. V. Svensson, I. Lynch, J. S. Bernardes and W. Loh, Ionic surfactants with polymeric counterions, *Adv. Colloid Interface Sci.*, 2009, **147–148**, 228–236.

61 L. Piculell, Understanding and exploiting the phase behavior of mixtures of oppositely charged polymers and surfactants in water, *Langmuir*, 2013, **29**, 10313–10329.

62 B. Lindman, F. Antunes, S. Aidarova, M. Miguel and T. Nylander, Polyelectrolyte-surfactant association—from fundamentals to applications, *Colloid J.*, 2014, **76**, 585–594.

63 S. Zhou and B. Chu, Assembled materials: Polyelectrolyte-surfactant complexes, *Adv. Mater.*, 2000, **12**, 545–556.

64 J. Janiak, S. Bayati, L. Galantini, N. V. Pavel and K. Schillén, Nanoparticles with a bicontinuous cubic internal structure formed by cationic and non-ionic surfactants and an anionic polyelectrolyte, *Langmuir*, 2012, **28**, 16536–16546.

65 G. Nizri, S. Magdassi, J. Schmidt, Y. Cohen and Y. Talmon, Microstructural characterization of micro- and nanoparticles formed by polymer-surfactant interactions, *Langmuir*, 2004, **20**, 4380–4385.

66 G. Nizri, A. Makarsky, S. Magdassi and Y. Talmon, Nanostructures formed by self-assembly of negatively charged polymer and cationic surfactants, *Langmuir*, 2009, **25**, 1980–1985.

67 K. Kogej, Study of the effect of polyion charge density on structural properties of complexes between poly(acrylic acid) and alkylpyridinium surfactants, *J. Phys. Chem. B*, 2003, **107**, 8003–8010.

68 M. C. Di Gregorio, M. Gubitosi, L. Travaglini, N. V. Pavel, A. Jover, F. Meijide, J. Vázquez Tato, S. Sennato, K. Schillén, F. Tranchini, S. De Santis, G. Masci and L. Galantini, Supramolecular assembly of a thermoresponsive steroidal surfactant with an oppositely charged thermoresponsive block copolymer, *Phys. Chem. Chem. Phys.*, 2017, **19**, 1504–1515.

69 J. Janiak, L. Piculell, K. Schillén and D. Lundberg, Responsive release of polyanions from soluble aggregates formed with a hydrolyzable cationic surfactant and a nonionic surfactant, *Soft Matter*, 2013, **9**, 4103–4112.

70 L. Chiappisi, I. Hoffmann and M. Gradzielski, Complexes of oppositely charged polyelectrolytes and surfactants - Recent developments in the field of biologically derived polyelectrolytes, *Soft Matter*, 2013, **9**, 3896–3909.

71 Y. Wang, H. Wu, J. Wang, P. Lou, Y. Zhao and G. Bai, Thermodynamics of self-aggregation of mixed cationic gemini/sodium deoxycholate surfactant systems in aqueous solution, *J. Therm. Anal. Calorim.*, 2019, **135**, 2903–2913.

72 M. Akram, I. A. Bhat, Z. Yaseen and Kabir-ud-Din, Physicochemical investigation of novel biodegradable dicationic ester bonded m-E2-m gemini surfactants with bile salts: Insights from surface tension, dynamic light scattering and fluorescence, *Colloids Surfaces A Physicochem. Eng. Asp.*, 2014, **444**, 209–216.

73 Y. Wang, R. M. F. Fernandes and E. F. Marques, From single gemini surfactants in water to catanionic mixtures with the bile salt sodium taurodeoxycholate: Extensive micellar solutions, coacervation and liquid crystal polymorphism as revealed by phase behavior studies, *J. Mol. Liq.*, 2019, **285**, 330–337.

74 Q. Li, X. Yue, P. Shang, Y. Quan, M. Ren, Y. Ma and X. Chen, Environmental stimuli induced phase transition in the aqueous mixture solution of Gemini surfactants and sodium deoxycholate, *Colloids Surfaces A Physicochem. Eng. Asp.*, 2016, **489**, 67–74.

75 L. J. Zhu, D. D. Huang, Q. T. Li, G. C. Xu and X. Chen, Nanofibers and vesicles self-assembled from Gemini surfactant complexes with bile salts, *Wuli Huaxue Xuebao/ Acta Phys. - Chim. Sin.*, 2013, **29**, 2415–2421.

76 Y. Wang, P. Lou, G. Bai, C. Fan and M. Bastos, Cationic gemini and sodium cholate - Following the interaction of oppositely charged surfactants by calorimetry, turbidity and conductivity, *J. Chem. Thermodyn.*, 2014, **73**, 255–261.

77 S. Padasala, V. Patel, D. Ray, K. Singh, V. K. Aswal and P. Bahadur, Bile salt assisted morphological changes of cationic gemini surfactant (12-4-12) micelles, *RSC Adv.*, 2016, **6**, 96584–96594.

78 X. Li and H. Kunieda, Catanionic surfactants: Microemulsion formation and solubilization, *Curr. Opin. Colloid Interface Sci.*, 2003, **8**, 327–336.

79 R. Zhang and P. Somasundaran, Advances in adsorption of surfactants and their mixtures at solid/solution interfaces, *Adv. Colloid Interface Sci.*, 2006, **123–126**, 213–229.

80 A. Singh, J. D. Van Hamme and O. P. Ward, Surfactants in microbiology and biotechnology: Part 2. Application aspects, *Biotechnol. Adv.*, 2007, **25**, 99–121.

81 L. Piculell and B. Lindman, Association and segregation in aqueous polymer/polymer, polymer/surfactant, and surfactant/surfactant mixtures: Similarities and differences, *Adv. Colloid Interface Sci.*, 1992, **41**, 149–178.

82 N. I. Kapakoglou, D. L. Giokas, G. Z. Tsogas and A. G. Vlessidis, Coacervation of surface-functionalized polymerized vesicles derived from ammonium bromide surfactants. Application to the selective speciation of chromium in environmental samples, *Anal. Chem.*, 2008, **80**, 9787–9796.

83 Y. Yeo, E. Bellas, W. Firestone, R. Langer and D. S. Kohane, Complex coacervates for thermally sensitive controlled release of flavor compounds, *J. Agric. Food Chem.*, 2005, **53**, 7518–7525.

84 Y. Xu, M. Mazzawi, K. Chen, L. Sun and P. L. Dubin, Protein purification by polyelectrolyte coacervation: Influence of protein charge anisotropy on selectivity, *Biomacromolecules*, 2011, **12**, 1512–1522.

85 D. J. Burgess and J. E. Carless, Manufacture of gelatin/gelatin coacervate microcapsules, *Int. J. Pharm.*, 1985, **27**, 61–70.

86 W. Dong and R. Bodmeier, Encapsulation of lipophilic drugs within enteric microparticles by a novel coacervation method, *Int. J. Pharm.*, 2006, **326**, 128–138.

87 W. Zhao and Y. Wang, Coacervation with surfactants: From single-chain surfactants to gemini surfactants, *Adv. Colloid Interface Sci.*, 2017, **239**, 199–212.

88 M. Wang and Y. Wang, Development of surfactant coacervation in aqueous solution, *Soft Matter*, 2014, **10**, 7909–7919.

89 M. Wang, Y. Fan, Y. Han, Z. Nie and Y. Wang, Coacervation of cationic gemini surfactant with N-benzoylglutamic acid in aqueous solution, *Langmuir*, 2013, **29**, 14839–14847.

90 H. Fan, B. Li, Y. Yan, J. Huang and W. Kang, Phase behavior and microstructures in a mixture of anionic Gemini and cationic surfactants, *Soft Matter*, 2014, **10**, 4506–4512.

91 M. Jendric, N. Filipović-Vinceković, M. Vinceković, M. Bujan and I. Primožić, Phase behavior of bis(quaternary ammonium bromide)/sodium cholate/H2O system, *J. Dispers. Sci. Technol.*, 2005, **26**, 39–51.

92 O. Glatter, *Scattering methods and their application in colloid and interface science*, Elsevier Inc., Amsterdam, 2018.

93 J. Goodwin, *Colloids and Interfaces with Surfactants and Polymers*, John Wiley & Sons Ltd, Chichester, 2009.

94 P. N. Pusey, in *Neutrons, X-rays and light: scattering methods applied to soft condensed matter*, eds. P. Lindler and T. Zemb, Elsevier Science B.V., Amsterdam, 2002, pp. 3–22.

95 L. Ogendal, *Light scattering demystified, Theory and practice*, 2019.

96 W. Schärtl, *Light scattering from polymer solutions and nanoparticle dispersions*, Springer, Berlin, 2007.

97 J. Jansson, K. Schillén, M. Nilsson, O. Söderman, G. Fritz, A. Bergmann and O. Glatter, Small-angle X-ray scattering, light scattering, and NMR study of PEO-PPO-PEO triblock copolymer/cationic surfactant complexes in aqueous solution, *J. Phys. Chem. B*, 2005, **109**, 7073–7083.

98 P. C. Hiemenz and R. Rajagopalan, *Principles of colloid and surface chemistry, Revised and expanded*, CRC press, New York, 1997.

99 A. Guinier and G. Fournet, *Small-angle scattering of X-rays*, John Wiley & Sons, Inc., New York, 1955.

100 O. Spalla, in *Neutrons, X-rays and light: Scattering methods applied to soft condensed matter*, eds. P. Lindler and T. Zemb, Elsevier Science B.V., Amsterdam, 2002, pp. 49–71.

101 O. Glatter, A new method for the evaluation of small-angle scattering data, *J. Appl. Crystallogr.*, 1977, **10**, 415–421.

102 SasView for small angle scattering analysis, http://www.sasview.org/.

103 I. Breßler, J. Kohlbrecher and A. F. Thünemann, SASfit: A tool for small-angle scattering data analysis using a library of analytical expressions, *J. Appl. Crystallogr.*, 2015, **48**, 1587–1598.

104 D. A. Skoog, F. J. Holler and S. R. Crouch, *Principles of instrumental analysis*, Cengage learning, 2017.

105 C. Zhou, D. Langevin and S. Guillot, Internal organisation in polyelectrolytes/oppositely charged surfactants colloidal complexes anticipating precipitated nanostructures, *Eur. Phys. J. E*, 2011, **34**, 1–7.

106 A. J. F. Siegert, Radiation Laboratory report no. 465, *Massachusetts Inst. Technol. Cambridge, MA*.

107 W. Brown and T. Nicolai, in *Dynamic light scattering—The method and some applications*, ed. W. Brown, Oxford University Press Inc., New York, 1993, pp. 272–318.

108 B. J. Frisken, Revisiting the method of cumulants for the analysis of dynamic light-scattering data, *Appl. Opt.*, 2001, **40**, 4087.

109 P. Štêpánek, in *Dynamic light scattering—The method and some applications*, ed. W. Brown, Oxford University Press Inc., New York, 1993, pp. 177–241.

110 S. W. Provencher, A constrained regularization method for inverting data represented by linear algebraic or integral equations, *Comput. Phys. Commun.*, 1982, **27**, 213–227.

111 J. Jakeš, Regularized positive exponential sum (REPES) program-A way of inverting laplace transform data obtained by dynamic light scattering, *Collect. Czechoslov. Chem. Commun.*, 1995, **60**, 1781–1797.

112 H. Cui, T. K. Hodgdon, E. W. Kaler, L. Abezgauz, D. Danino, M. Lubovsky, Y. Talmon and D. J. Pochan, Elucidating the assembled structure of amphiphiles in solution via cryogenic transmission electron microscopy, *Soft Matter*, 2007, **3**, 945–955.

113 D. Danino, Cryo-TEM of soft molecular assemblies, *Curr. Opin. Colloid Interface Sci.*, 2012, **17**, 316–329.

114 E. Callaway, Molecular-imaging pioneers scoop Nobel, *Nature*, 2017, **550**, 167.

115 H. Friedrich, P. M. Frederik, G. De With and N. A. J. M. Sommerdijk, Imaging of self-assembled structures: Interpretation of TEM and Cryo-TEM images, *Angew. Chem. Int. Ed.*, 2010, **49**, 7850–7858.

116 P. Schultz, Cryo-electron microscopy of vitrified specimens, *Q. Rev. Biophys.*, 1988, **21**, 129–228.

117 J. J. De Yoreo and N. A. J. M. Sommerdijk, Investigating materials formation with liquid-phase and cryogenic TEM, *Nat. Rev. Mater.*, 2016, **1**, 1–18.

118 C. Colliex, Seeing and measuring with electrons: Transmission electron microscopy today and tomorrow - An introduction, *Comptes Rendus Phys.*, 2014, **15**, 101–109.

119 R. F. Thompson, M. Walker, C. A. Siebert, S. P. Muench and N. A. Ranson, An introduction to sample preparation and imaging by cryo-electron microscopy for structural biology, *Methods*, 2016, **100**, 3–15.

120 F. Nudelman, G. De With and N. A. J. M. Sommerdijk, Cryo-electron tomography: 3-dimensional imaging of soft matter, *Soft Matter*, 2011, **7**, 17–24.

121 P. L. Stewart, Cryo-electron microscopy and cryo-electron tomography of nanoparticles, *Wiley Interdiscip. Rev. Nanomedicine Nanobiotechnology*, 2017, **9**, 1–16.

122 J. R. Kremer, D. N. Mastronarde and J. R. McIntosh, Computer visualization of three-dimensional image data using IMOD, *J. Struct. Biol.*, 1996, **116**, 71–76.

123 E. F. Pettersen, T. D. Goddard, C. C. Huang, G. S. Couch, D. M. Greenblatt, E. C. Meng and T. E. Ferrin, UCSF Chimera - A visualization system for exploratory research and analysis, *J. Comput. Chem.*, 2004, **25**, 1605–1612.

124 G. Cox, *Optical imaging techniques in cell biology*, CRC Press, New York, 2012.

125 C. H. Spink, in *Methods in cell biology*, Elsevier Inc., 2008, vol. 84, pp. 115–141.

126 G. Olofsson and G. Wang, in *Polymer-surfactant systems*, ed. J. C. T. Kwak, CRC Press, New York, 1998, pp. 317–356.

127 W. Loh, C. Brinatti and K. C. Tam, Use of isothermal titration calorimetry to study surfactant aggregation in colloidal systems, *Biochim. Biophys. Acta - Gen. Subj.*, 2016, **1860**, 999–1016.

128 M. W. Freyer and E. A. Lewis, in *Methods in cell biology*, Elsevier Inc., 2008, vol. 84, pp. 79–113.

129 P. Bharmoria and A. Kumar, Thermodynamic investigations of protein's behaviour with ionic liquids in aqueous medium studied by isothermal titration calorimetry, *Biochim. Biophys. Acta - Gen. Subj.*, 2016, **1860**, 1017–1025.

130 K. Makino and H. Ohshima, Electrophoretic mobility of a colloidal particle with constant surface charge density, *Langmuir*, 2010, **26**, 18016–18019.

131 A. V. Delgado, F. González-Caballero, R. J. Hunter, L. K. Koopal and J. Lyklema, Measurement and interpretation of electrokinetic phenomena: (IUPAC technical report), *Pure Appl. Chem.*, 2005, **77**, 1753–1805.

132 M. Instruments, Zetasizer Nano series technical note, *MRK654-01*.

133 S. Kelly and N. Price, The use of circular dichroism in the investigation of protein structure and function, *Curr. Protein Pept. Sci.*, 2000, **1**, 349–384.

134 S. M. Kelly, T. J. Jess and N. C. Price, How to study proteins by circular dichroism, *Biochim. Biophys. Acta - Proteins Proteomics*, 2005, **1751**, 119–139.

135 S. R. Martin and M. J. Schilstra, in *Methods in cell biology*, Elsevier Inc., 2008, vol. 84, pp. 263–293.

136 G. Blauer and G. Wagniere, Conformation of bilirubin and biliverdin in their complexes with serum albumin, *J. Am. Chem. Soc.*, 1975, **97**, 1949–1954.

137 P. Novotná and M. Urbanová, Bilirubin, model membranes and serum albumin interaction: The influence of fatty acids, *Biochim. Biophys. Acta - Biomembr.*, 2015, **1848**, 1331–1340.

138 I. Goncharova, S. Orlov and M. Urbanová, The location of the high- and low-affinity bilirubin-binding sites on serum albumin: Ligand-competition analysis investigated by circular dichroism, *Biophys. Chem.*, 2013, **180–181**, 55–65.

139 G. Conte, R. Di Blasi, E. Giglio, A. Parretta and N. V. Pavel, Nuclear magnetic resonance and X-ray studies on micellar aggregates of sodium deoxycholate, *J. Phys. Chem.*, 1984, **88**, 5720–5724.

140 A. Rich and D. M. Blow, Formation of a helical steroid complex, *Nature*, 1958, **182**, 423–426.

141 A. A. D'Archivio, L. Galantini, E. Giglio and A. Jover, X-ray and quasi-elastic light-scattering studies of sodium deoxycholate, *Langmuir*, 1998, **14**, 4776–4781.

142 H. Amenitsch, H. Edlund, A. Khan, E. F. Marques and C. La Mesa, Bile salts form lyotropic liquid crystals, *Colloids Surfaces A Physicochem. Eng. Asp.*, 2003, **213**, 79–92.

143 N. V. Hud and K. H. Downing, Cryoelectron microscopy of phage DNA condensates in vitreous ice: The fine structure of DNA toroids, *Proc. Natl. Acad. Sci.*, 2001, **98**, 14925–14930.

144 M. Lueckheide, J. R. Vieregg, A. J. Bologna, L. Leon and M. V. Tirrell, Structure-property relationships of oligonucleotide polyelectrolyte complex micelles, *Nano Lett.*, 2018, **18**, 7111–7117.

145 Y. Lansac, J. Degrouard, M. Renouard, A. C. Toma, F. Livolant and E. Raspaud, A route to self-assemble suspended DNA nano-complexes, *Sci. Rep.*, 2016, **6**, 21995.

146 D. McLoughlin, M. Delsanti, C. Tribet and D. Langevin, DNA bundle formation induced by cationic surfactants, *Europhys. Lett.*, 2005, **69**, 461–467.

147 K. Osada, Structural polymorphism of single pDNA condensates elicited by cationic block polyelectrolytes, *Polymers (Basel).*, 2020, **12**, 1603.

148 A. M. Carnerup, M.-L. Ainalem, V. Alfredsson and T. Nylander, Condensation of DNA using poly(amido amine) dendrimers: effect of salt concentration on aggregate morphology, *Soft Matter*, 2011, **7**, 760–768.

149 N. V. Hud and I. D. Vilfan, Toroidal DNA condensates: unraveling the fine structure and the role of nucleation in determining size, *Annu. Rev. Biophys. Biomol. Struct.*, 2005, **34**, 295–318.

150 V. A. Bloomfield, DNA condensation, *Curr. Opin. Struct. Biol.*, 1996, **6**, 334–341.

151 W. M. Gelbart, R. F. Bruinsma, P. A. Pincus and V. A. Parsegian, DNA inspired electrostatics, *Phys. Today*, 2000, **53**, 38–44.

152 A. F. Jorge, S. C. C. Nunes, T. F. G. G. Cova and A. A. C. C. Pais, Cooperative action in DNA condensation, *Curr. Opin. Colloid Interface Sci.*, 2016, **26**, 66–74.

153 V. A. Bloomfield, DNA condensation by multivalent cations, *Biopolymers*, 1997, **44**, 269–282.

154 R. Ninomiya, K. Matsuoka and Y. Moroi, Micelle formation of sodium chenodeoxycholate and solubilization into the micelles: Comparison with other unconjugated bile salts, *Biochim. Biophys. Acta - Mol. Cell Biol. Lipids*, 2003, **1634**, 116–125.

155 I. J. Arroyo-Maya and D. J. McClements, Application of ITC in foods: A powerful tool for understanding the gastrointestinal fate of lipophilic compounds, *Biochim. Biophys. Acta - Gen. Subj.*, 2016, **1860**, 1026–1035.

156 M. Uchman, M. Gradzielski, B. Angelov, Z. Tošner, J. Oh, T. Chang, M. Štěpánek and K. Procházka, Thermodynamic and kinetic aspects of coassembly of PEO-PMAA block copolymer and DPCl surfactants into ordered nanoparticles in aqueous solutions studied by ITC, NMR, and time-resolved SAXS techniques, *Macromolecules*, 2013, **46**, 2172–2181.

157 M. D'Alagni, M. Delfini, L. Galantini and E. Giglio, A study of the interaction of bilirubin with sodium deoxycholate in aqueous solutions, *J. Phys. Chem.*, 1992, **96**, 10520–10528.

158 G. Lazzara, G. Olofsson, V. Alfredsson, K. Zhu, B. Nyström and K. Schillén, Temperature-responsive inclusion complex of cationic PNIPAAM diblock copolymer and γ-cyclodextrin, *Soft Matter*, 2012, **8**, 5043–5054.

159 S. Bayati, K. Zhu, L. T. T. Trinh, A. L. Kjøniksen and B. Nyström, Effects of temperature and salt addition on the association behavior of charged amphiphilic diblock copolymers in aqueous solution, *J. Phys. Chem. B*, 2012, **116**, 11386–11395.

160 A. Wangsakan, P. Chinachoti and D. J. McClements, Isothermal titration calorimetry study of the influence of temperature, pH and salt on maltodextrin-anionic surfactant interactions, *Food Hydrocoll.*, 2006, **20**, 461–467.

161 M. Thongngam and D. J. McClements, Characterization of interactions between chitosan and an anionic surfactant, *J. Agric. Food Chem.*, 2004, **52**, 987–991.

162 D. J. McClements, Isothermal titration calorimetry study of pectin - Ionic surfactant interactions, *J. Agric. Food Chem.*, 2000, **48**, 5604–5611.

163 W. Loh, L. A. C. Teixeira and L. T. Lee, Isothermal calorimetric investigation of the interaction of poly(N-isopropylacrylamide) and ionic surfactants, *J. Phys. Chem. B*, 2004, **108**, 3196–3201.

164 G. Olofsson and G. Wang, Interactions between surfactants and uncharged polymers in aqueous solution studied by microcalorimetry, *Pure Appl. Chem.*, 1994, **66**, 527–532.

165 G. Wang and G. Olofsson, Ethyl(hydroxyethyl)cellulose and ionic surfactants in dilute solution. Calorimetric and viscosity study of the interaction with SDS and some cationic surfactants, *J. Phys. Chem.*, 1995, **99**, 5588–5596.

166 A. Niemiec and W. Loh, Interaction of ethylene oxide-propylene oxide copolymers with ionic surfactants studied by calorimetry: Random versus block copolymers, *J. Phys. Chem. B*, 2008, **112**, 727–733.

167 S. Dai and K. C. Tam, Isothermal titration calorimetric studies on the interaction between sodium dodecyl sulfate and polyethylene glycols of different molecular weights and chain architectures, *Colloids Surfaces A Physicochem. Eng. Asp.*, 2006, **289**, 200–206.

168 R. G. Orth and R. C. Dunbar, Luminescent probes for detergent solutions. A simple procedure for determination of the mean aggregation number of micelles, *J. Am. Chem. Soc.*, 1978, 5951–5952.

169 M. Almgren and J. E. Löfroth, Determination of micelle aggregation numbers and micelle fluidities from time-resolved fluorescence quenching studies, *J. Colloid Interface Sci.*, 1981, **81**, 486–499.

170 J. Stam, M. Almgren and C. Lindblad, Sodium dodecylsulfate-poly(ethyleneoxide) interactions studied by time-resolved fluorescence quenching, *Prog. Colloid Polym. Sci.*, 1991, **84**, 13–20.

171 M. Swanson-Vethamuthu, P. L. Dubin, M. Almgren and Y. Li, Cryo-TEM of polyelectrolyte-micelle complexes, *J. Colloid Interface Sci.*, 1997, **186**, 414–419.

172 P. Hansson and M. Almgren, Interaction of CnTAB with sodium (carboxymethyl)cellulose: Effect of polyion linear charge density on binding isotherms and surfactant aggregation number, *J. Phys. Chem.*, 1996, **100**, 9038–9046.

173 J. Courtois and J. F. Berret, Probing oppositely charged surfactant and copolymer interactions by isothermal titration microcalorimetry, *Langmuir*, 2010, **26**, 11750–11758.

174 J. F. Berret, G. Cristobal, P. Hervé, J. Oberdisse and I. Grillo, Structure of colloidal complexes obtained from neutral/polyelectrolyte copolymers and oppositely charged surfactants, *Eur. Phys. J. E*, 2002, **9**, 301–311.

175 J. F. Berret, B. Vigolo, R. Eng, P. Hervé, I. Grillo and L. Yang, Electrostatic self-assembly of oppositely charged copolymers and surfactants: A light, neutron, and X-ray scattering study, *Macromolecules*, 2004, **37**, 4922–4930.

176 J. F. Berret, Evidence of overcharging in the complexation between oppositely charged polymers and surfactants, *J. Chem. Phys.*, 2005, **123**, 164703.

177 P. Novotná, F. Králík and M. Urbanová, Chiral recognition of bilirubin and biliverdin in liposomes and micelles, *Biophys. Chem.*, 2015, **205**, 41–50.

178 J. H. Perrin and M. Wilsey, The induced optical activity of bilirubin in the presence of sodium deoxycholate, *J. Chem. Soc. D Chem. Commun.*, 1971, 769–770.